DCT 241

Cross-Frame Forces in Skewed Steel I-Girder Bridges: Field Measurements and Finite Element Analysis

By

Jennifer McConnell

Research Assistants:
Matija Radovic
Kelly Ambrose

Center for Innovative Bridge Engineering

April, 2014

Delaware Center for Transportation
University of Delaware
355 DuPont Hall
Newark, Delaware 19716
(302) 831-1446

Project Report for

Cross-Frame Forces in Skewed Steel I-Girder Bridges: Field Measurements and Finite Element Analysis

Prepared for

Delaware Department of Transportation

by

Jennifer McConnell

with

Matija Radovic
Kelly Ambrose

Center for Innovative Bridge Engineering

College of Engineering
University of Delaware
Newark, DE 19716

April 2014

This work was sponsored by the Delaware Center for Transportation and was prepared in cooperation with the Delaware Department of Transportation. The contents of this report reflect the view of the authors who are responsible for the facts and accuracy of the data presented herein. The contents do not necessarily reflect the official views of the Delaware Center for Transportation or the Delaware Department of Transportation at the time of publication. This report does not constitute a standard, specification, or regulation.

The Delaware Center for Transportation is a university-wide multi-disciplinary research unit reporting to the Chair of the Department of Civil and Environmental Engineering, and is co-sponsored by the University of Delaware and the Delaware Department of Transportation.

DCT Staff

Ardeshir Faghri
Director

Jerome Lewis
Associate Director

Ellen Pletz
Business Administrator I

Earl "Rusty" Lee
T^2 Program Coordinator

Matheu Carter
T^2 Engineer

Sandra Wolfe
Event Coordinator

DCT Policy Council

Robert McCleary, Co-Chair
Chief Engineer, Delaware Department of Transportation

Babatunde Ogunnaike, Co-Chair
Dean, College of Engineering

Delaware General Assembly Member
Chair, Senate Highways & Transportation Committee

Delaware General Assembly Member
Chair, House of Representatives Transportation/Land Use & Infrastructure Committee

Ajay Prasad
Professor, Department of Mechanical Engineering

Harry Shenton
Chair, Civil and Environmental Engineering

Drew Boyce
Director of Planning, Delaware Department of Transportation

Ralph Reeb
Planning Division, Delaware Department of Transportation

Executive Director, Delaware Transit Corporation

Representative of the Director of the Delaware Development Office

James Johnson
President, JTJ Engineers, LLC

Holly Rybinski
Rybinski Engineering

Delaware Center for Transportation
University of Delaware
Newark, DE 19716
(302) 831-1446

Cross-Frame Forces in Skewed Steel I-Girder Bridges:

Field Measurements and Finite Element Analysis

FINAL REPORT

Submitted to:

Delaware Department of Transportation

PI:

Jennifer McConnell

Research Assistants:

Matija Radovic and Kelly Ambrose

Submitted:

April 8, 2014

ACKNOWLEDGMENTS

This research was made possible by the Delaware Department of Transportation (DelDOT). In addition to financial support, logistical support was provided through providing equipment and personnel to assist with the field testing reported on herein. These contributions to this research are gratefully acknowledged.

TABLE OF CONTENTS

EXECUTIVE SUMMARY

Steel I-girder bridges are one of the most common bridge configurations in use today and cross-frames are an important secondary member in this type of bridge. The facts that cross-frame members provide lateral-load resistance, facilitate distribution of traffic loads among girders, and reduce the buckling length of the compression flanges of the steel girders are currently implicitly or explicitly considered in design and rating processes. However, the design and behavior of cross-frames under routine loadings is a relatively poorly understood topic, particularly for skewed and curved bridges where the role of cross-frames becomes more significant. In addition to the commonly-considered functions of cross-frames listed above, they also provide redundant load paths and play a role in a bridge's inelastic response. Thus, this research was motivated by the desire to better understand cross-frames' stress-states and roles in load distribution at both elastic and inelastic load levels.

This is of interest because, while it is known that bridges have the capacity to easily sustain loads greater than their design loads, a codified method for quantifying this reserve capacity that accounts for the three-dimensional structural behavior does not exist. The fact that girder bridges are typically designed and rated based on a line-girder approach that neglects the redundant load paths that girders provide results in significant conservatism. A method that accounts for this redundancy through analyzing bridge girder systems versus bridge girders would not only enable the design of more efficient structures, but could also be a highly valuable tool for bridge management. Given the well-documented state of structurally deficient bridges nationwide, the application of system-level analysis would allow for better identification and prioritization of the most critical structures and allow for a more

efficient use of the limited financial resources available for infrastructure investments. The work described herein is a step towards this goal.

Chapters 1, 2, and 3 provide background on and methodology employed in this research. Specifically, Chapter 1 discusses the motivations, objectives, scope, and organization of the research. Chapter 2 provides a review of literature relevant to the subject research and describes the two bridges used in the field testing. Chapter 3 reviews the finite element analysis (FEA) methodologies used in this work.

Chapter 4 discusses the field testing completed in service of the first objective of this project: to quantify the forces in cross-frames via field testing of in-service, skewed, steel I-girder bridges. Two bridges of varying skews, SR 1 over US 13 (abbreviated herein as US-13) and SR 299 over SR 1 (abbreviated herein as SR-299), both located in New Castle County, Delaware were field tested for this purpose. US-13 is heavily skewed with a skew angle of 65 degrees and SR-299 is moderately skewed with a skew angle of 32 degrees. Because skew has been shown to have a significant impact on a bridge's reserve capacity, these two levels of skew were chosen for study. Other than varying skew angles, a pair of bridges having nearly equal values of other key variables affecting structural response was sought. As a result, the two bridges have similar span configurations, span lengths, girder spacings, and material properties. The structures differ in cross-frame configuration (K-frame versus X-frame) and layout (inline versus staggered) in order to further explore potential effects of differing cross-frame designs.

During these tests, both cross-frames and girder cross-sections were instrumented to determine both cross-frame forces and the distribution of force in the system. Overall between the two bridges, the field tests captured data for 121 points

on 11 cross-frames and 6 girder locations. A finite element model for each bridge was built and analyzed prior to testing in order to develop instrumentation plans for the field work. In order for these tests to serve their intended purpose of providing data for validating the finite element model, the applied loads during the period when data was collected must be known. It order to accomplish this, the bridge was closed to ambient traffic while a weighed test vehicle crossed the bridge in multiple passes.

The results of the field testing, which are discussed in Chapter 5, indicate interesting differences between the responses of these two bridges. The two most significant differences were that, in the bridge with staggered K-frames and less skew (SR-299), the cross-frame forces were significantly reduced and the magnitude of lateral bending was significantly higher. Specifically, the peak cross-frame stress due to the weighed vehicle in US-13 is nearly three times the corresponding value in SR-299 (4.2 ksi versus 1.5 ksi) while the girder stresses in the two structures are similar to one another (1.5 ksi and 1.7 ksi). Based on the known relationship between skew and torsional force, the higher skew of US-13 is a likely reason for the increased cross-frame stresses in this bridge. The peak lateral bending stress in SR-299 is 3.7 times larger than the peak lateral bending stress observed in US-13 (550 psi vs. 149 psi). The lateral bending stress in SR-299 also contributes more significantly to the total stress relative to the results for US-13, with SR-299 having a lateral to vertical bending stress ratio of 69% compared to the maximum value for this quantity in the US-13 results being 38%. The peak lateral bending stress of 550 psi appears to be related to the fact that the location where this occurs is equidistant between two staggered cross-frames.

A similarity in the two sets of field data is data indicating that the cross-frame members experience a significant amount of bending, which is indicated by both variation in stress along the length of the member as well as variation in stress through the member cross-sections. For example, the highest difference between the two gauges on a given cross-section of a US-13 cross-frame member is 4.5 ksi. This effect was observed as being most prominent in diagonal members experiencing tension.

The next primary objective was to calibrate corresponding finite element models of the field tested bridges which accurately capture the three-dimensional behavior of the bridges. These results are also discussed in Chapter 5 and show that the FEA is of acceptable accuracy in some cases but that the FEA accuracy is very sensitive to the manner in which cross-frames are modeled. For example, the FEA of US-13 showed that the tensile bottom flange stresses were well predicted by the model in all cases with a maximum percent difference of 13%. Weaker correlation between the field and FEA web results was revealed to be due to field results showing that when the peak stress occurred in one gauge of a pair of gauges on opposite sides of the same web cross-section, the other gauge of the pair would be experiencing an opposite force effect (i.e., tension on one side of the web and compression on the other, Figure 5.11. It is hypothesized that this is due to a combination of lateral bending and warping torsion of these non-compact webs. This effect is not reproduced when the cross-frames are modeled using the commonly-accepted beam elements. However, this effect is reproduced when the cross-frames were modeled with shell elements. In fact, the percent difference between the field and FEA web stress results decreased by as much as 100%. Regarding the correlation between the cross-frame field and FEA data, the general trend of the variation in stress from gauge to gauge that was observed

in the field results was reproduced with reasonable accuracy, but the percent differences in magnitude varied between 1 and 900%, or as much as 2 ksi, with the field results typically giving higher values. As a result of these efforts it was concluded that the global response of US-13 was accurately simulated, but accurately simulating localized effects requires a FEM even more refined that the detailed FEM used in this work. Similar behavior was obtained for SR-299, but a larger discrepancy between field and FEA values typically occurred despite FEA peak girder stresses matching theoretical expectations well. The comparison of field, FEA, and theoretical expectations led to the hypothesis that this may be due to the field behavior deviating from theoretical expectations to unintended fixity of the bearings.

The third primary objective was to perform a FEA parametric study for the purposes of observing the effect of cross-frame layout (staggered versus inline) and configuration (x-frame versus k-frame) on girder and cross-frame stresses as well as bridge ultimate capacity. This work is discussed in Chapter 6. Given the improved correlation between the field and FEA responses of US-13, this model was selected as the basis for a parametric study where K-frames versus X-frames and staggered versus inline cross-frame layouts were evaluated. The fact that the comparison between the FEA and field peak bottom flange stresses was within 5% gives confidence that girder results generated in these parametric models will be of reasonable accuracy. The greater variation in cross-frame stresses suggests that relative differences in cross-frame stress throughout these models will provide a reasonable estimate of cross-frame behavior, but that the FEA results will likely under-estimate the magnitudes of stress that would be likely to occur in a physical representation of the structures being

modeled and these facts should be kept in mind when assessing cross-frame output from these models.

Despite the fact that the results from the US-13 field results suggest that these models will produce lower bounds of cross-frame demands, the cross-frames were found to be a critically-stressed component at both service and ultimate load levels. At service load levels, while all cross-frame tensile stresses were well below the corresponding tensile capacities, compressive stresses exceed the member capacities in three of the four models. Furthermore, a significant variation in the compression results was observed with the peak compressive stresses varying by 50% in the different models, with K-frames in a staggered configuration producing the greatest stress and inline X-frames producing the lowest stress. In assessing the governing compressive stress results relative to the buckling capacities of the cross-frame members, it was seen that the design stresses are exceed by as much as 29% under the service level loading and that this occurs in the bottom chord of the X-frame, which has a significantly reduced capacity compared to the other members, in the staggered model. The locations of maximum cross-frame stresses in all models are in cross-frames adjacent to supports.

In the nonlinear analyses, all models resisted a live load of at least 57 times the loading used in the field test, which is the load magnitude equivalent of 44 HS-20 vehicles, in addition to self-weight. At this level of loading and for the modeling assumptions used in this work (which most notably consisted of linear elastic transverse load distribution mechanisms due to the assumed concrete and cross-frame properties), a significant level of load redistribution was observed, with four of the five girders having a fully yielded bottom flange at mid-span of the loaded span as

well as one or more girders yielded in the bottom flanges at the abutment of the loaded span and over the pier support.

These observations along with the quantification of the spread of plasticity in each model led to the conclusion that cross-frame layout was more influential to inelastic girder response than cross-frame configuration. Viewing the inelastic regions in all models it was shown that in the staggered models, the yielded area is larger as the load has more points along the girder length where load can be transferred transversely due to the discontinuities in cross-frame placement. However, there are more locations where the bottom flange cross-section has yielded on only one side of the girder cross-section, indicating greater lateral bending stresses in these models. In terms of magnitudes of bottom flange stresses, it was found that stagger increases the compressive stress by as much as 12%. However, these effects do not indicate any significant consequence on the structural performance of the girders in terms of peak magnitude of stress under service level loads or a significant difference in the load distribution characteristics of the girders due to differences in either cross-frame configuration or layout.

With regards to the cross-frame results from the inelastic analyses, it was again concluded that the results were more sensitive to cross-frame layout than configuration, with more yielding observed in the inline cross-frames. These stress results were then considered relative to the governing compression capacities of the cross-frame members. When viewed from this perspective, the compressive demand to capacity ratios of the cross-frame members are more sensitive to cross-frame configuration than layout. Furthermore, this showed that the compressive capacities of the cross-frame members was exceeded in all four models. The largest difference was

detected in the diagonal member of the K-frame Inline model where the capacity is only 7% of the demand. The X-frame Staggered model was observed as experiencing both the lowest magnitude of peak compressive strain and the lowest demand to capacity ratios.

Considering that the final girder stress state of all models was relatively similar in demonstrating favorable load redistribution, this load redistribution will be most likely to be achieved in situations where the cross-frame stress is minimized. Thus, it is concluded that the X-frame staggered configuration is the one most likely to lead to the greatest reserve capacity in the system. Modifications to the member sizes used in these cross-frames likely provide the best opportunity for further increasing this reserve capacity.

This report concludes with Chapter 7. Here the scope of work and conclusions are summarized and recommendations for future work are offered.

Chapter 1

INTRODUCTION

1.1 Motivation

Steel I-girder bridges are one of the most common bridge configurations in use today and cross-frames are an important secondary member in this type of bridge. The facts that cross-frame members provide lateral-load resistance, facilitate distribution of traffic loads among girders, and reduce the buckling length of the compression flanges of the steel girders are currently implicitly or explicitly considered in design and rating processes. However, they also provide redundant load paths and contribute significantly to a bridge's inelastic response and this research was motivated by the desire to better understand cross-frames' roles in these responses.

This is of interest because, while it is known that bridges have the capacity to easily sustain loads greater than their design loads, a codified method for quantifying this reserve capacity that accounts for the three-dimensional structural behavior does not exist. The fact that girder bridges are typically designed and rated based on a line-girder approach that neglects the redundant load paths that girders provide results in significant conservatism. A method that accounts for this redundancy through analyzing bridge girder systems versus bridge girders would not only enable the design of more efficient structures, but could also be a highly valuable tool for bridge management. Given the well-documented state of structurally deficient bridges nationwide, the application of system-level analysis would allow for better

identification and prioritization of the most critical structures and allow for a more efficient use of the limited financial resources available for infrastructure investments. The work described herein is a step towards this goal.

Additionally, the design and behavior of cross-frames under routine loadings is a relatively poorly understood topic, particularly for skewed and curved bridges where the role of cross-frames becomes more significant. Furthermore, it is also known that skew influences girder system capacity. Thus, the influence of skew was selected as a primary variable in the present research.

1.2 **Objectives and Scope**

The first objective of this project was to quantify the forces in cross-frames via field testing of two in-service, skewed, steel I-girder bridges. Specifically, one bridge is heavily skewed with a skew angle of 65 degrees and the other is moderately skewed with a skew angle of 32 degrees. Because skew has been shown to have a significant impact on a bridge's reserve capacity, these two levels of skew were chosen for study. During these tests, both cross-frames and girder cross-sections were instrumented to determine both cross-frame forces and the distribution of force in the system. A finite element model for each bridge was built and analyzed prior to testing in order to develop instrumentation plans for the field work. In order for these tests to serve their intended purpose of providing data for validating the finite element model, the applied loads during the period when data was collected must be known. It order to accomplish this, the bridge was closed to ambient traffic while a weighed test vehicle crossed the bridge in multiple passes.

The next primary objective was to calibrate corresponding finite element models of these bridges that accurately capture the three-dimensional behavior of the bridges. This was carried out using the commercial FEA software Abaqus through modeling the girders and concrete components with shell elements and the cross-frame with beam elements. Various refinements to the cross-frame modeling was also explored in order to determine the influence of this refinement on model accuracy relative to the field test results. As a result of this work, significant variations in cross-frame forces are observed and analyzed. The third primary objective was to perform a FEA parametric study for the purposes of observing the effect of cross-frame layout (staggered versus inline) and configuration (x-frame versus k-frame) on girder and cross-frame stresses as well as bridge ultimate capacity.

1.3 **Report Organization**

Following the introduction to the research provided in the present chapter, Chapter 2 background information, including a literature review of related research and a detailed description of the two bridges chosen for field testing. Chapter 3 describes the finite element methodology used for: developing the instrumentation plans for the field work described in Chapter 4; creating detailed finite element models simulating the field test in order to further understand the observed response through the greater level of detail afforded by FEA, which is described in Chapter 5; and for performing the parametric study on the influence of cross-frame configuration (staggered versus inline and x-frame versus k-frame), which is described in Chapter 6. Chapter 7 summarizes conclusions from the research.

Chapter 2

BACKGROUND

2.1 Literature Review

The American Association of State Highway and Transportation Officials (AASHTO 2010) LRFD Bridge Design Specifications define a cross-frame as a transverse truss framework connecting adjacent longitudinal flexural components. There are two main types of cross-frames: X-type or K-type. According to Bishara and Elmir (1990), intermediate cross-frames are primarily used in multibeam steel bridges as a means for lateral-load resistance, live-load distribution, and reduction of the buckling length of the compression flanges of the steel girders. Bridge skew, cross-frame type, and cross-frame spacing, among other variables, are important considerations when investigating cross-frame forces as detailed in this section.

Researches have used finite element analysis to investigate the interaction between cross-frames and girders. Bishara and Elmir (1990) studied cross-frame forces in skewed steel bridges, looking specifically at X-type cross-frames in simply supported welded steel plate girder bridges with composite reinforced concrete decks with variable skew angles. This research determined that the effect of skew on the forces induced in cross-frame members may be neglected for skew angles less than twenty degrees. It was also found that the higher the skew angle, the higher the maximum forces that are induced in the cross-frame members. The investigation also concluded that increasing the cross-sections of the cross-frame members increases the internal forces in the cross-frames. It showed that the maximum compressive forces occurred in members attached to the ends of exterior girders situated at the obtuse angles of the bridge and maximum tensile forces occurred in the chord members at

mid-span. Bishara and Elmir (1990) used three-dimensional finite element analysis that using the computer program ADINA. They used triangular plate elements to discretize the concrete deck and beam elements to discretize the cross-frame members. Stringers were divided into top and bottom halves. Each half is discretized as beam elements joined to the other half by steel link elements. The top halves of the stringers were connected to the slab plate elements by rigid link elements.

Wang and Helwig (2008) studied the influence of cross-frame orientation on cross-frame requirements in bridges with skewed supports, the cross-frames of which they explain are more susceptible to large live load than those in bridges with normal supports. They performed computational studies on the torsional bracing behavior of steel girders with skewed supports using the three-dimensional finite element program ANSYS. They focused on two-, three-, and four-girder systems with lines of bracing oriented either parallel to the skew angle or perpendicular to the longitudinal axis of the girders. In most cases, transverse stiffeners were created using shell elements, while cross-frames were modeled using truss elements. The skew angles considered ranged from 0 to 45 degrees. Elastic material properties were used in the analyses and three different types of loading were considered: uniform moment loading, a uniformly distributed load applied along the girder length, and a single point load applied at mid-span. They found that for cases when the bracing is oriented perpendicular to the girder lines, the effects of the skew angle had little effect on the stiffness and strength requirements of the bracing. When the bracing was oriented parallel to the skew angle, the skew angle had a more significant impact on the stiffness and strength requirements of the bracing (Wang and Helwig 2008).

Additional work by Wang et al (2011) showed that cross-frame forces can be less in bridges with staggered cross-frames.

Full scale bridge models have also been tested in a structural laboratory to determine the influence of cross-frames on load resisting capacity of steel girder bridges. Azizinamini et al. (1995) carried out full scale tests on a bridge built in the laboratory. The bridge was a 70 ft long simple span with a total width of 26 ft consisting of 3 welded plate girders 54 in. deep, built compositely with a 7 ½ in-thick reinforced concrete deck. By doing 12 different tests using this model, the researchers were able to vary the type of cross-frame (K or X), cross-frame spacing, and loading using the same girders. It was found that when both lanes of the bridge were loaded, when the truck load was applied straddling the bridge centerline, and when only one lane was loaded, the maximum strain in the girders was not significantly affected by the cross-frame type. Ultimately it was concluded that cross-frames had little influence on steel bridges with skews smaller than 20 degrees after construction. The influence of cross-frames on bridges with skews greater than 20 degrees was not investigated. Also, they concluded that simpler and cheaper forms of cross-frames such as the X-type provide the same effective behavior as the more expensive K-type of cross-frame in bridges less than 20 degrees skew.

Research has also been done using the finite element method to analyze girder-diaphragm interaction. Tedesco et al. (1995) modeled an actual simply supported steel highway bridge with no skew located in Birmingham, Alabama. The deck slab was modeled with four-node shell elements to accurately represent membrane stresses, while the diaphragms were modeled with two-node beam elements. The objective was to determine whether or not diaphragms can be removed from an existing bridge. The

finite element analysis was compared with actual field testing of the bridge in order to validate the model. It was discovered that the removal of diaphragms had a modest effect on bridge response, increasing flexural stress and vertical deflection for the most highly stressed girders by 8% and 9%, respectively.

Separately relating to the goals of the present work, there has also been research dealing with the influence of skew on ultimate capacity, which informed the selection of bridges in this work. While investigating the ultimate capacity of skewed simple-span bridges, Bechtel (2001) evaluated six bridge models using the finite element analysis software ABAQUS with skews ranging from zero to seventy five degrees. The cross braces were placed at a maximum spacing of 25 feet and the length of the girder was held constant in order to keep the width to length ratio constant at approximately 1:5 which kept factors that affect longitudinal stiffness constant. Bechtel (2001) discovered that the magnitude of load causing yielding in each girder increases as the skew angle increases, but there is no significant contribution until the skew is greater than sixty degrees, at which point the bridge begins to behave differently and load redistribution is different. From this research, it was ultimately discovered that large skews have a significant beneficial effect on the reserve capacity of a bridge.

Other researchers, such as Fell and Kanvinde (2010), who conducted several large scale tests on bracing members undergoing seismic loading, have explored how cross-frame bracing aides seismic design along with other considerations. Others have looked at more specific cross-frame detailing. Quadrato et al. (2010) looked specifically at cross-frame connection details and discovered that many states use a bent plate for this connection since code provisions require end cross-frames to be

aligned parallel to the skew angle. The research explains that although cross-frames can often represent an expensive component per unit weight on a bridge due to fabrication complexities and construction fit-up issues, they are essential to the stability of steel girder bridges during construction. Finite element analysis was then used to investigate how the cross-frame connection affected the bracing behavior of the bridge and how it could be possibly altered to reduce cost.

The influence of cross-frame placement and skew angle in steel bridges subject to distortion-induced fatigue has also been investigated. Hartman et al. (2010) conducted forty high-resolution, three-dimensional finite element analyses of a bridge with multiple cross-frame and skew arrangements in order to study the relationships between skew angle, cross-frame placement, and distortion-induced fatigue stresses. In the models, skew angles of 0, 20, and 40 degrees were used with cross-frames spaced at 15 ft and 30 ft. Each model was composed of a deck, girder top flanges and concrete haunch, girder webs, girder bottom flanges, and cross-frames with element types, mesh sizes, and boundary conditions remaining constant among all the models. The loading consisted of one AASHTO fatigue truck placed to induce maximum positive moment on the east span of the two-span continuous bridge. Ultimately, they found that in bridges with cross-frames placed parallel to the skew angle, increased cross-frame spacing slightly increased the maximum principle web-gap stress. They found that in bridges with staggered cross-frames, the web-gap stresses were not found to increase proportionally with skew angle.

Numerical models of continuous, skewed, steel bridges have also been created to study the effect of lateral-torsional buckling during deck placement and the role of cross-frames in deck placement. Liu and Chajes (2008) studied a 63 degree four-span

continuous plate girder bridge made with high performance steel (HPS) with three spans of 199.25 ft and one span of 175 ft. It had K-shaped cross-frames designed parallel to the skewed supports. They created two three-dimensional finite element models using ANSYS with the girders and wet concrete represented as shell elements and the cross-frames as frame elements. When investigating the deck pour sequence, the hardening concrete was assumed to have 10% of its fully cured modulus of elasticity. From their research, they discovered that the deck pour sequence on skewed bridges could be adjusted to avoid complications with lateral-torsional buckling. Fasl et al. (2009) commented on how buckling capacity is improved for lateral torsional buckling of steel plate girder bridges during deck placement by providing bracing in the form of intermediate cross-frames and made recommendations to be implemented in the design of three bridges in Texas.

In conclusion, research has shown that skew angle is an important factor in a bridge's response, but more research to understand the behavior at inelastic load levels is needed. In addition, cross-frame spacing has been shown to have a larger influence than cross-frame type; therefore an attempt was made to keep this variable as constant as possible between the bridges used in the field work so that the influence of skew angle could be more directly assessed.

2.2 **Bridge Descriptions**

The two bridges field tested in this work were chosen by considering the ideas presented in the literature review and the population of bridges available for testing. Many of Delaware's bridges that were good candidates for this study intersected Interstate 95, a main highway on the East Coast. The traffic control to field test these

bridges was considered to be an unnecessary complication; therefore any bridges that crossed or contained I95 were not considered for this study. After these bridges were removed from consideration, the number of steel I-girder bridges remaining for consideration was limited. It was decided to choose a moderately- and a heavily-skewed bridge in order to assess a range of skews. Because the difference between cross-frame shapes was not found to be significant, both K shaped cross-frames and X-shaped cross-frames were considered in this study. Two bridges of relatively the same length and span configuration were also desired. When taking all these restrictions into considerations, SR 1 over US 13 and SR 299 over SR 1 were chosen for study and are described in the following subsections.

2.2.1 **SR 1 over US 13**

SR 1 over US 13 is a 65 degree skew (which is considered heavily-skewed) steel I-girder bridge on Delaware State Route 1. Twin spans carry the north- and southbound lanes. The tested bridge carries the southbound lanes of State Route 1 over U.S. 13 approximately 5 miles south of the Chesapeake and Delaware Canal in Delaware, immediately south of Road 423 and just north of Boyd's Corner, Delaware. Figure 2.1 indicates the location of this bridge. It consists of two continuous spans of equal (165 feet) lengths as seen in photograph in Figure 2.2 and in elevation view in Figure 2.3. Figure 2.4 demonstrates a plan view of the bridge. There are five girders spaced 9'- 6" on center with exterior girders spaced 2'-10" and 3'- 10" away from the outer edge of the bridge parapets on the west and east sides, respectively, as can be seen in Figure 2.5. Therefore, the total width of the bridge is 44'-8", carrying two 12' lanes, a 12' shoulder on the west side, and a 6' shoulder on the east side, while also

having parapets 1’-4” in width on each side of the bridge. A girder elevation view is included in Figure 2.6.

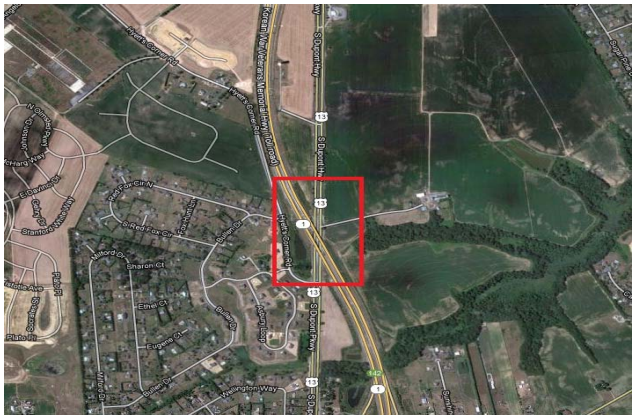

Figure 2.1 Satellite View of SR 1 Over US 13 (Google Maps, 2012)

Figure 2.2 Photograph of SR 1 Over US 13, Elevation View

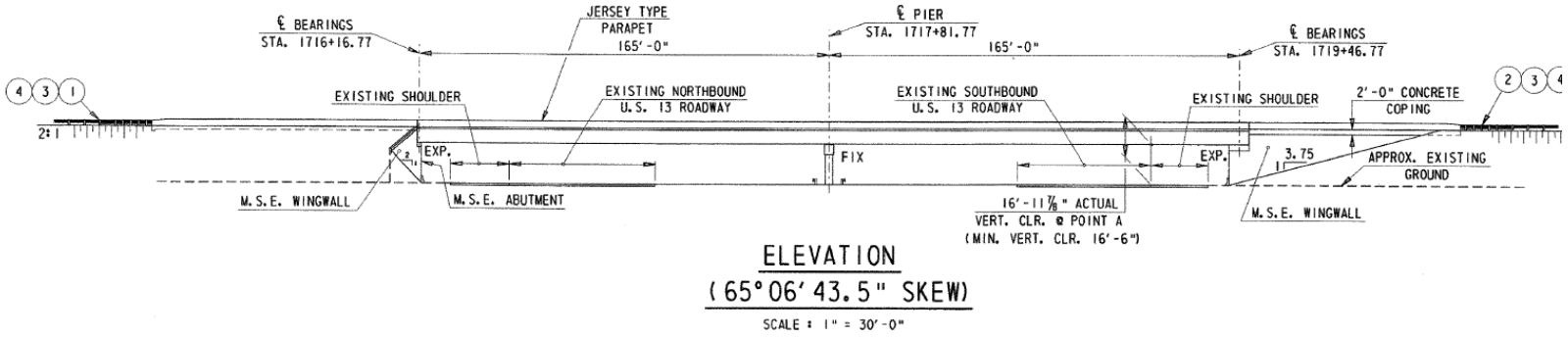

Figure 2.3 SR 1 over US 13 Elevation View

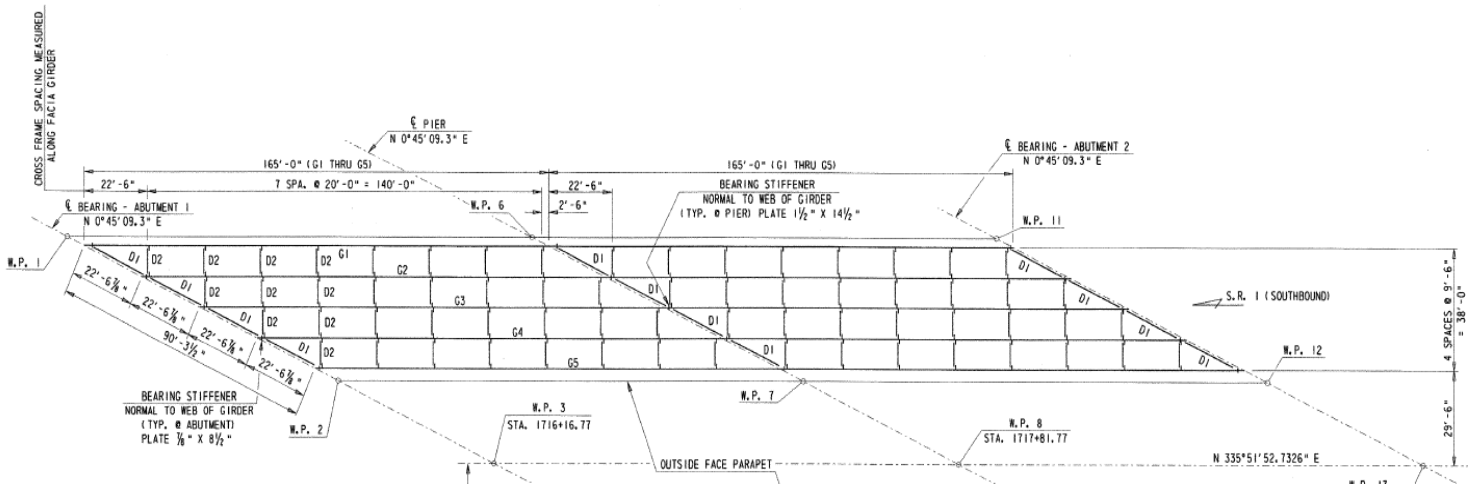

Figure 2.4 SR 1 over US 13 Plan View

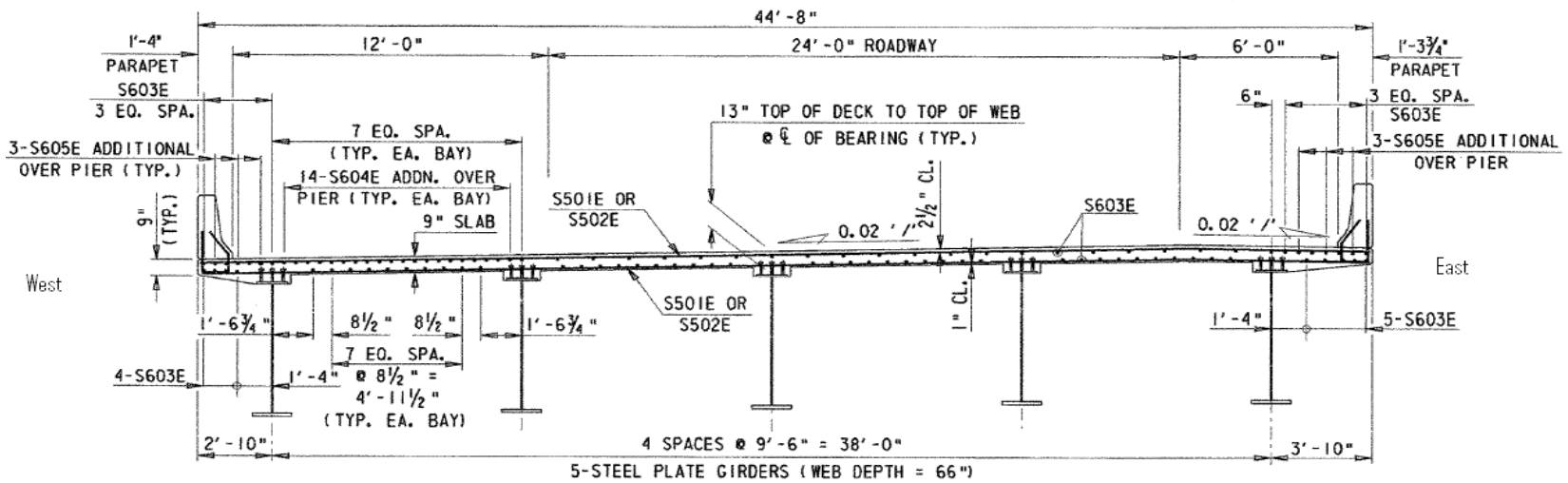

Figure 2.5 SR 1 over US 13 Cross-Section View

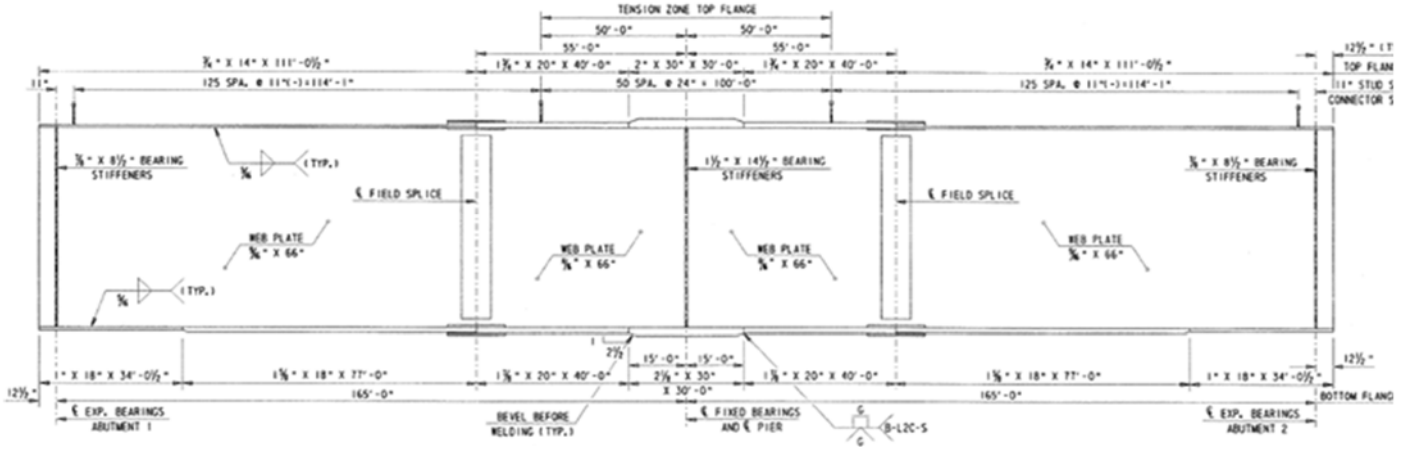

Figure 2.6 SR 1 over US 13 Girder Elevation View

As represented in Figure 2.7, X-type cross-frames are used to laterally brace the girders of the bridge. These are spaced 20 feet on center with the exception of the first cross-frame from the end and the first cross-frame from the pier support which are spaced at 22'- 6" on center. As seen in Figure 2.7, the cross-frames consist of two 3 ½ x 3 ½ x 3/8 inch steel angles that comprise the inclined members of the cross-frame and a 4 x 4 x ½ inch steel angle serves as the bottom chord. The two inclined members are bolted at their intersection by a ½" x 6" x 1'- 1" fill plate. All of the angles are bolted to the girders with Type 1, 7/8" diameter A325 high strength mechanically galvanized friction bolts via a ½" x 10" connection plate fillet welded along the full height of the web. The cross-frames are seen in photograph in Figure 2.8. All structural steel is AASHTO M270 Grade 50 (F_y = 50,000 psi) painted with a urethane paint. The steel girder is composite with the bridge deck.

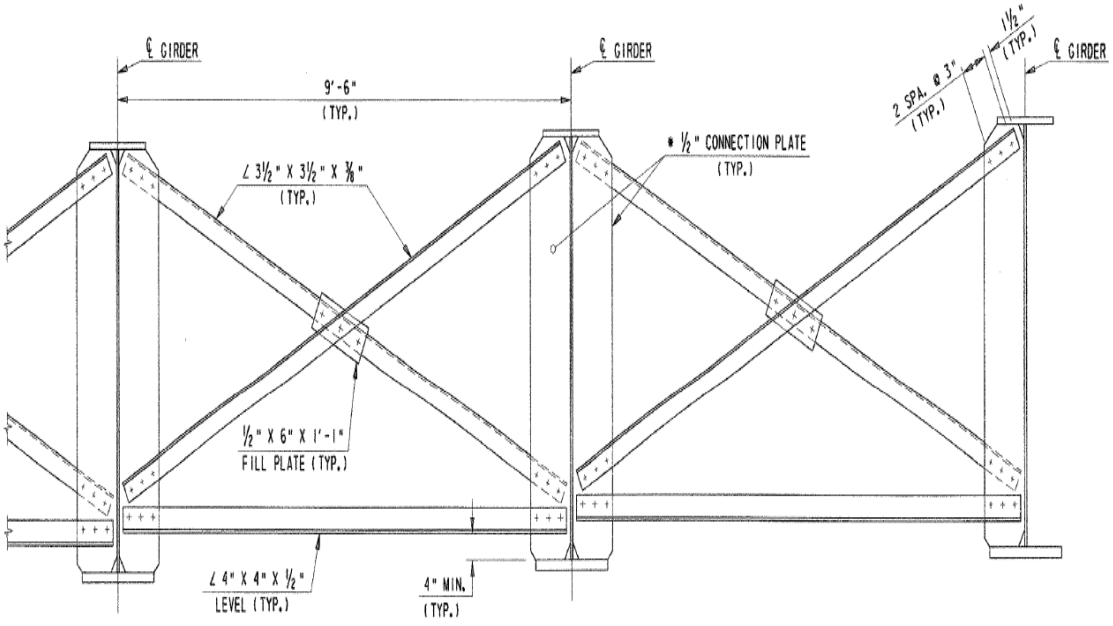

Figure 2.7 SR 1 Over US 13 Intermediate Cross-frame Detail

Figure 2.8 Photograph of SR 1 Over US 13 Cross-frames

2.2.2 SR 299 over SR 1

SR 299 over SR 1 is a 32 degree skew (considered moderately-skewed) steel I-girder bridge on Delaware State Route 299 over Delaware State Route 1. It is located in the Middletown-Odessa area of Delaware, approximately 9 miles south of the Chesapeake and Delaware Canal in Delaware, with a map of the location shown in Figure 2.9. It consists of two spans, of 128 feet and 134 feet, as seen in photograph in Figure 2.10 and in elevation view plans in Figure 2.11. Figure 2.12 demonstrates a plan view of the bridge. There are eleven girders in the cross-section, spaced 9'- 1" with exterior girders spaced 2'-11" away from the outer edge of the bridge parapets, as shown in Figure 2.13. Therefore, the total width of the bridge is 95'-11", carrying four 12' lanes of traffic, two 12' outside shoulders, a 22' median and turning lane which

varies in position along the length of the bridge, and two 1'-4" parapets. A girder elevation view is included in Figure 2.14.

As represented in Figure 2.15, K-type cross-frames are used to laterally brace the girders of the bridge and are spaced 18'- 3" on center on the west span and 19' – 6" on the east span with the exception of the first cross-frame from each support, where the spacing varies (see Fig. 2.12). As seen in Figure 2.15, the typical cross-frames consist of two 3 ½" x 3 ½" x 3/8" steel angles that comprise the inclined members of the cross-frame and one 4" x 4" x ½" steel angle that serves as the bottom chord. The two steel angles of the inclined members are welded with a 5/16" fillet weld on both sides to a 1/2" gusset plate, which is also connected by a 5/16" fillet weld on both sides to the midspan of the bottom chord. All fillet welds are at least 4" in length. All of the angles are connected with 5/16" fillet welds to ½" gusset plates that are bolted to the ½" x 7" connection plate fillet welded to the girders along the full height of the web. The cross-frames are shown in photograph in Figure 2.16. All structural steel is AASHTO M270 Grade 50 (F_y = 50,000 psi) and is painted.

Figure 2.9 Satellite View of SR 299 Over SR 1 (Google Maps, 2012)

Figure 2.10 Photograph of SR 299 Over SR 1, Elevation View

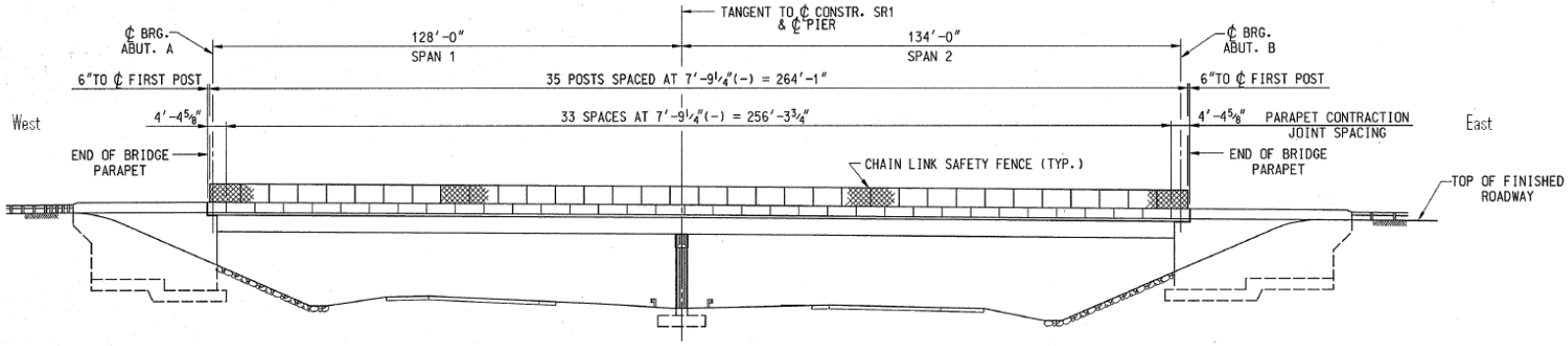

Figure 2.11 SR 299 Over SR 1 Elevation View

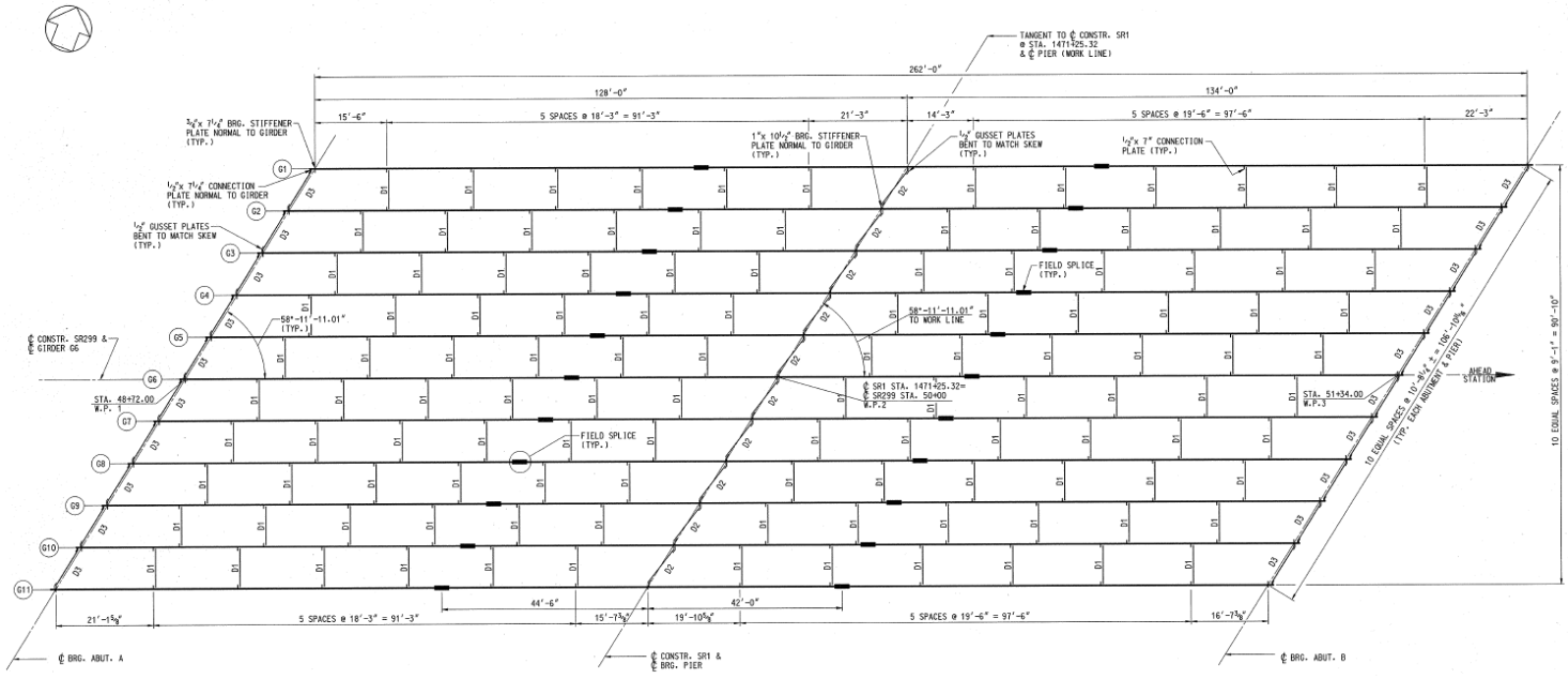

Figure 2.12 SR 299 Over SR 1 Plan View

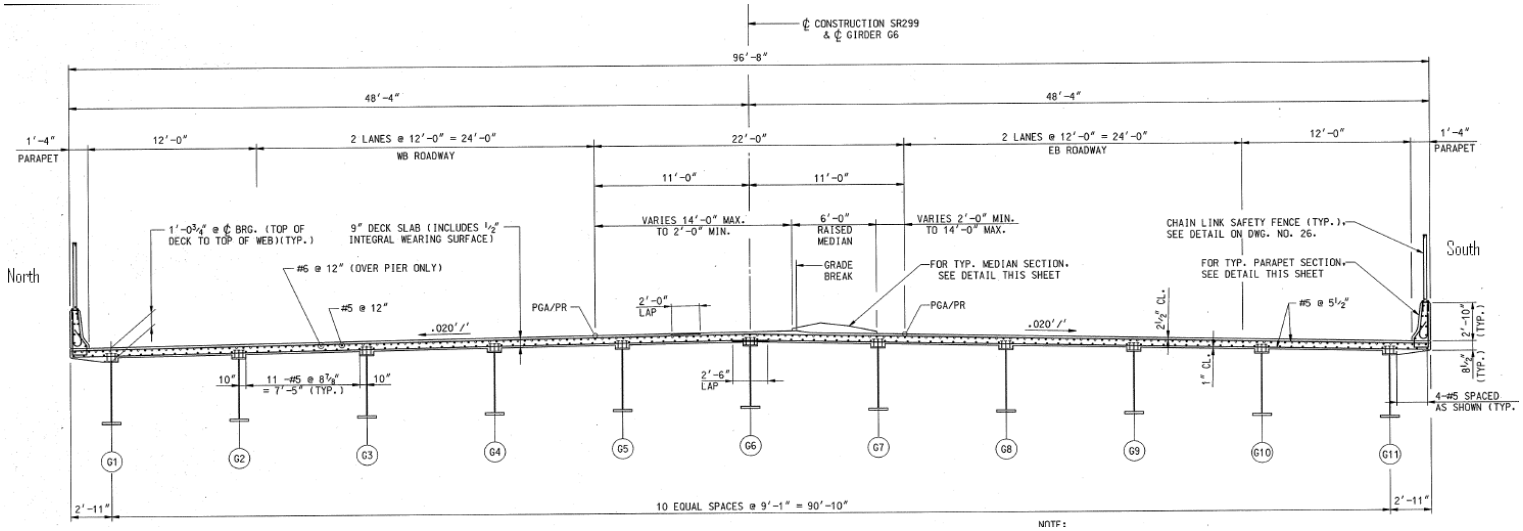

Figure 2.13 SR 299 Over SR 1 Bridge Cross-section

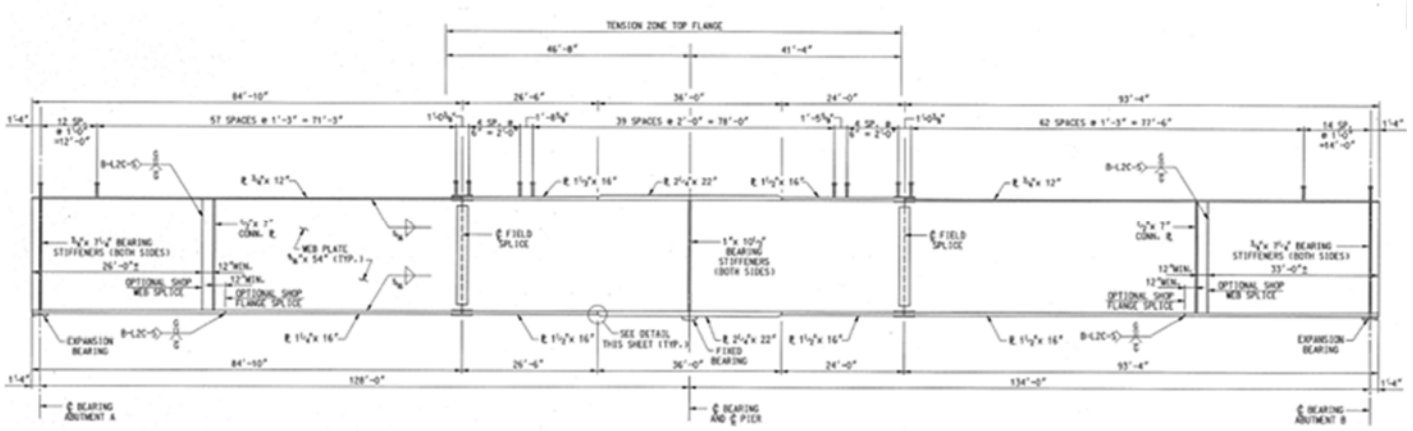

Figure 2.14 SR 299 Over SR 1 Girder Elevation

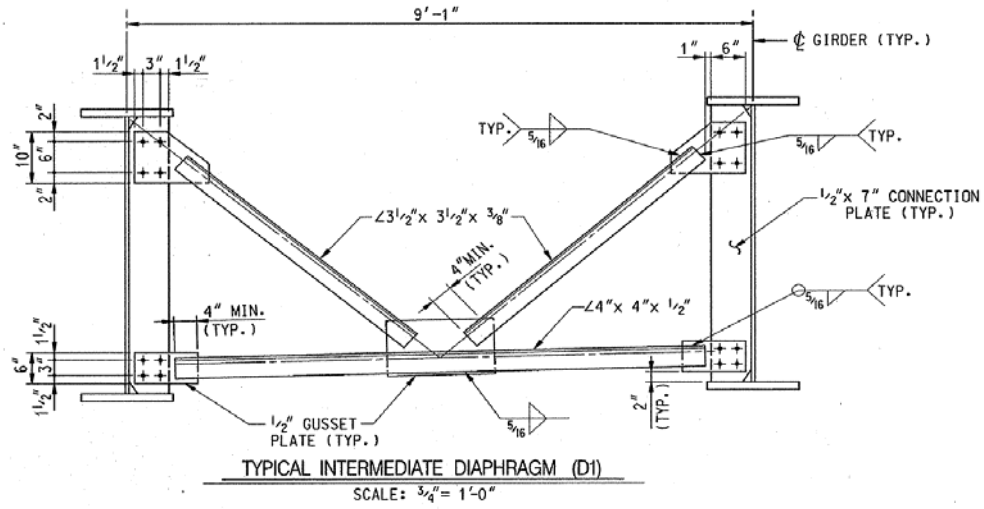

Figure 2.15 SR 299 Over SR 1 Intermediate Cross-frame Details

Figure 2.16 Photograph of SR 299 Over SR 1 Cross-frames

Chapter 3

FINITE ELEMENT MODELING

3.1 Introduction

Finite element analysis (FEA) is a numerical technique for finding approximate solutions of partial differential equations, often done as a computer simulation in engineering analysis. For this project, computer-aided modeling was employed to create and analyze finite element models for each of the bridges studied. This section describes the development of the finite element models for the two skewed bridges described in Section 2.2. For this work, AutoCAD was used to create the basic geometry, commercial software was used for pre-processing, and ABAQUS 6.9-2 was used for analysis and post-processing.

3.2 Geometry

The geometry of each bridge was first created based on structural plans provided by DelDOT. This geometry was initially drawn using AutoCAD software. Here the coordinate system was such that the z-axis aligned with the length of the bridge, the x-axis was aligned with the transverse direction, and the y-axis was aligned with the vertical direction. The main structural components of the bridge used to make the superstructure model included the girders, concrete haunches, reinforced concrete deck, and parapets. These components were connected together with cross-frames and stiffeners serving as connection plates. Figure 3.1, below, demonstrates an example of the base geometry drawn in AutoCAD.

Once the basic geometry was completed in AutoCAD, it was then imported into a pre-processing program to begin the next stage of the model construction. As will be discussed in Section 3.3, this involved assigning material properties and three-dimension geometry to the different components drawn in AutoCAD.

3.3 **Elements**

The girder flanges and webs, stiffeners, deck, haunch, and parapet were modeled using 4-node, fully integrated shell elements, labeled as type S4 in ABAQUS. Shell elements have displacement and rotational degrees of freedom.

Cross-frame members were modeled using beam elements. Specifically, beam type B31 in ABAQUS was used. This is a one-dimensional line element in three-dimensional space having 3 translational and 3 rotational degrees of freedom at each

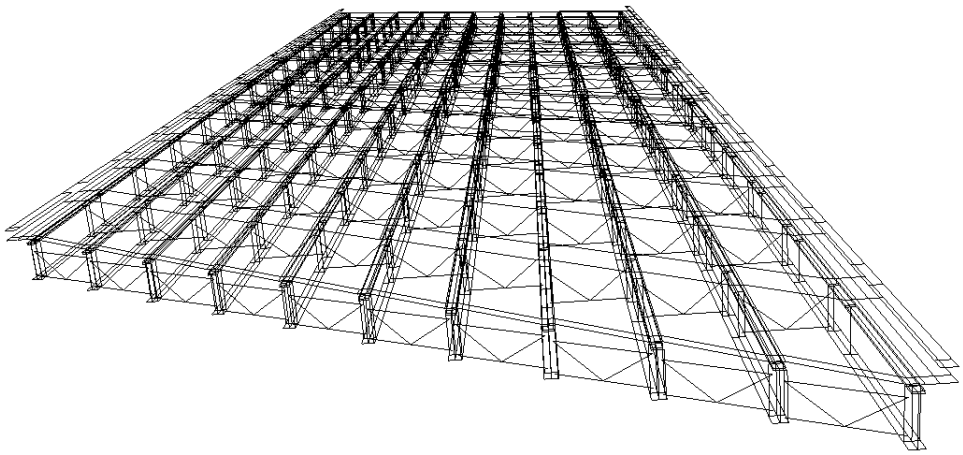

Figure 3.1 Base Geometry for SR 299 in AutoCAD

node. The cross-sectional properties corresponding to each of the beam elements were created by defining specific dimensions on a standard section, such as an angle, provided in the pre-processing software, using the standard nominal dimensions of the members specified in the structural plans provided by DelDOT. The beam elements were further defined by an orientation vector perpendicular to the length of the element to define the orientation of the cross-section, i.e., which direction the legs of the angles were oriented.

The girders, haunches, deck, and parapets were connected using rigid links. Specifically, rigid multiple point constraint (MPC) beams were used to link the elements of the top flanges to the haunches as well as the haunches to the deck and the deck to the parapets. In order for this connection to be made, the mesh was carefully created so that deck nodes were transversely aligned along the centerline of the girder and haunch and the longitudinal coordinates of all nodes to be connected were identical. The MPC elements then equate the displacement and rotation at the two connected nodes. In this way, the rigid links conceptually model the composite action between the slab and girders.

Linear-elastic and non-linear plastic material properties were used depending on the purpose of various FE models. Linear elastic material properties were used for the FEA validations of the field test described in Chapter 5 because these loads are not expected to, nor were they observed to, cause the steel or concrete elements to exceed their proportional limits. Thus, in these models, elastic properties were input for both the concrete and the steel. The concrete in models was defined with a modulus of elasticity of 4,286,830 psi (5 ksi compressive strength) and a Poisson's ratio of 0.2.

Steel was defined with a modulus of elasticity of 29,000 ksi and a Poisson's ratio of 0.32.

For the parametric studies described in Chapter 6.(Section 6.4.) where the models are loaded until failure, plastic material properties were specified for the girders and stiffeners, which also serve as connection plates. (The cross-frame members continued to be modeled using the elastic steel properties discussed in the previous paragraph because this is a limitation of this element type.) Abaqus requires plastic material input to be expressed in terms of true stress and logarithmic plastic strain. True stress (σ_T) is defined as the ratio of the external load to the instantaneous cross-sectional area of the loaded element and can be related to engineering stresses by Eq. 3-1,

$$\sigma_T = \sigma_E(1 + \epsilon_E) \qquad \textit{Equation 3-1}$$

where σ_E is engineering stress and ϵ_E is engineering strain. Engineering strain (ϵ_E) is related to logarithmic plastic strain (ϵ_{ln}) by Eq. 3-2,

$$\epsilon_{ln} = \ln(1 + \epsilon_E) - \frac{\sigma_T}{E_s} \qquad \textit{Equation 3-2}$$

where E_s is modulus of elasticity of steel. Table 3.1 shows the data points used to define a multi-linear constitutive law in Abaqus in terms of these quantities. For small deformation the difference between engineering and true stress is negligible. However, as strains exceed the elastic limit, the change in cross-sectional area increases, resulting in true stresses that can be significantly higher that engineering stresses.

Table 3.1 Steel Plastic Material Properties for Girders, Connection Plates and Stiffeners

True Stress (psi)	Logarithmic Plastic Strain
55,104	0
56,939	0.009
70,132	0.0248
112,650	0.4016

3.4 Mesh Generation

A critical part of the finite element model is the size of the elements used to discretize the different components of the bridge. This can have a large effect on the accuracy of the model as well as the time and amount of memory it takes to process the analysis. Larger element sizes reduce the number of degrees of freedom in the system, and thus the computation time. On the other hand, a sufficiently fine mesh, up to the point where convergence is achieved, is required in order to provide accuracy. Therefore, the mesh size was carefully considered while developing the finite element models for each of the bridges. The sizes of the elements were selected in order to evenly divide the girders and were consistent with element sizes that have been validated in previous research.

In order to utilize the rigid links to connect the girder, haunch, and deck, it was critical that the nodes along the centerline of each of these elements lined up vertically along the entire length of the structure. When initially planning the mesh, it became clear that this was going to be a difficult task. Non-uniform spacing in some locations of the bridge of the transverse stiffeners on the webs of the girders and changes in girder geometry along the length of the bridge caused a need for the element size

along the length of the girder's flanges to vary so that the node in the flanges and web align with the nodes in the transverse stiffeners. This process required several iterations in order to find a mesh size that would not only allow for these elements to be connected, but produce a mesh that was not too fine that it required a large amount of computer memory to process.

In general, at US-13 two elements were used along the width of the flanges except at the sections with the largest flange width for each bridge, where four elements were used along the width of the flanges to keep element sizes consistent and aspect ratios close to 1. The flanges at SR-299 have different widths; therefore smaller elements are used at SR-299 than US-13 to accommodate the difference in the widths and to keep aspect rations close to 1. As a result in SR-299, four, six and eight elements were used to model flange widths. At both models (US-13 and SR-299) two elements are used to model widths of the connection plates and stiffeners. The aspect ratio for connection plate and stiffeners at US 13 is calculated to be 1, while the aspect ratio for the same elements at SR-299 is calculated to be 1.27. The web of US-13 is modeled with 8 elements with aspect ratio of 1.5, while the web of SR-299 is modeled with 20 elements with aspect ratio of 1.3.

Eight elements were used along each of the inclined members of the X-shape cross-frames in the SR 1 over US 13 model, while 4 elements were used along each of the inclined members of the K-shape cross-frames in the SR 299 over SR 1 model. In the US-13 model, 8 elements were used along the bottom chord of the cross-frame, while in the SR-299 model, 4 elements were used in bottom chord. A reduced number of elements per cross-frame member was used for SR-299 due to the significantly larger size of this bridge and thus model. Changing the number of cross-frame bottom

chord elements for SR-299 did not significantly change the maximum stresses. Specifically, increasing the number of beam elements in the bottom chord of the cross-frame from 4 to 16 resulted in a stress increase from 829 psi to 838 psi (1% difference) at Gauge Location 12-4-H and 12-4-G. At Gauge Locations 12-5-F and 12-5-E the stress change was also 1% (from 924 psi to 934 psi). At the same time, the average bottom flange stress at Location G1 changed from 1491 psi to 1495 psi (0.26% difference). Thus, the larger cross-frame elements were deemed an appropriate compromise between accuracy and computational savings. The transverse stiffeners were meshed to align with the mesh of the web and the cross-frames were connected to the transverse stiffeners by merging the node from the beam element with the node on the mesh of the transverse stiffener closest to where the cross-frame is bolted (see Figure 3.2).

The mesh sizes of the haunch and deck were governed by the mesh size of the top flange, while mesh size of parapet was governed by mesh size of deck. As previously discussed, proper alignment between these elements is necessary in order to efficiently model composite action. In most cases the aspect ratio for the deck, haunch and parapet elements in the US -13 was 1.6, while the aspect ratio for the deck, haunch and parapet elements in the SR -299 was 1.3.

As previously mentioned a great care was taken in meshing the elements in order to have nodes from the elements from top flange, haunch and deck to be aligned. Once the top flange elements are created they are copied, and offset to the distance to match haunch and deck geometry from construction plans. Then, these copied elements are selected and their properties are changed to match properties of haunch and deck respectively. At the end of this step, only deck elements above the bridge

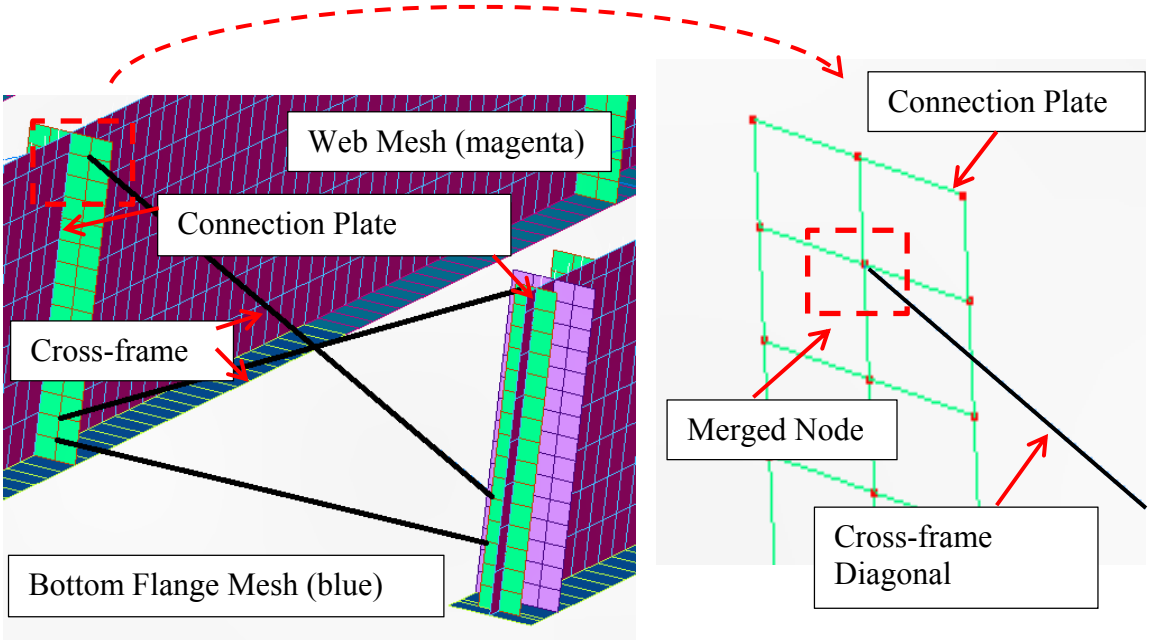

Figure 3.2 Cross-frame to Connection Plate Connection (FEM of the Bridge US-13)

girders were created. To fill the gap between bridge's girders the deck edge elements (along the length of the top flange) are then copied and pasted until they reached neighboring deck elements. At the point where neighboring deck elements were met, the small offset (0.3-0.5 in) between elements nodes were overcome by using "merge coinciding nodes" tool in pre-processing software. This pre-processing tool merges nodes on the elements that were in proximity of 0.5 in of each other, minimally distorting element shape.

In order to model the skewed ends of the bridge and maintain a uniform mesh of quadrilateral elements, first a reference line was drawn over each end of the bridge models (as shown at right side in Figure 3.3). Then, the deck elements are visually

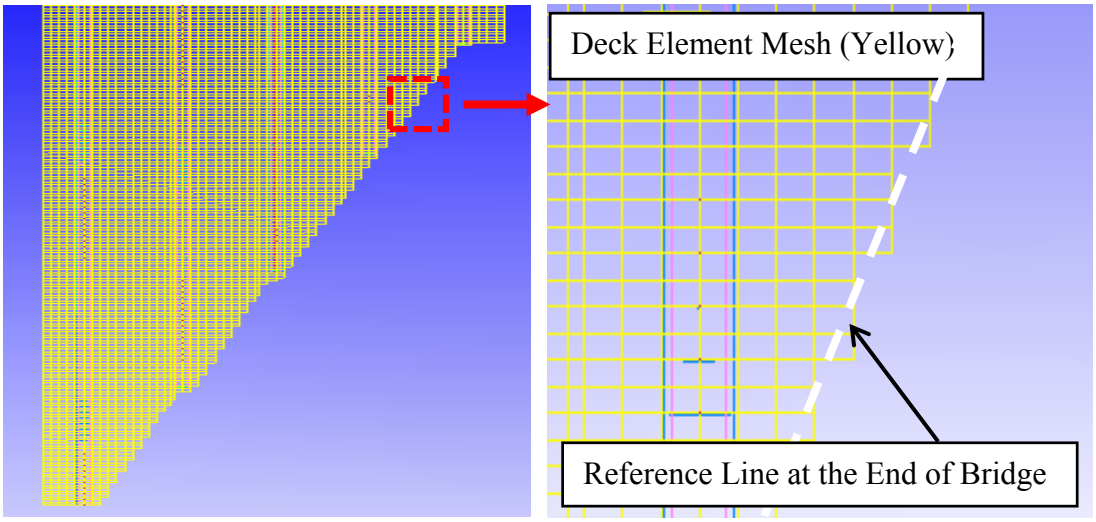

Figure 3.3 Deck Elements at the End of Bridge (FEM of US-13)

inspected and if more than 50% of the deck element area was outside the boundary established by this skewed line, the element was manually deleted; if the less than 50% of the deck element area was outside the reference line, the element was not deleted. The left side of Figure 3.3. shows the resulting deck mesh (wireframe view) relative to the end of the bridge for the US-13, while the right side of Figure 3.3 shows enhanced view of the reference line used to select deck elements that were deleted in order to form skew line.

3.5 **Boundary Conditions**

After the mesh was generated and material properties were added, appropriate boundary conditions had to be specified for each of the models. These were specified along the line of nodes along the width of the bottom flange of each girder at each of the bridge supports.

Both bridges (US -13 and SR-299) have the same type of supports; expansion bearings at abutments and fixed bearings at pier. Expansion bearings are modeled with translation in the transverse and vertical directions constrained, while fixed bearings are modeled with translation in the transverse, longitudinal, and vertical directions constrained.

In the preliminary study, used to develop instrumentation plan, translation in the transverse and vertical directions were constrained at the two supports at either end of the bridge where expansion bearings are located , while at pier support where fixed bearings are located translation in the transverse, longitudinal, and vertical directions were constrained. At the center node of the line of nodes along the bottom flange of the middle girder at the pier support, translation was constrained in all three directions and rotation was constrained in the longitudinal and vertical directions to provide sufficient stability in the analysis.

However, at the FEMs used for validation purposed, rotational constrains at center node at middle girder at the pier support, were removed, since the results showed that they did not contributed to stability of analysis. Figure 3.4 shows constraints used at FEMs of US-13 and SR-299. Figure 3.4 on the left shows bottom flange elements at abutment, with expansion bearing being modeled with the middle node (node with constraints labeled “1,2”, which corresponds to lateral and vertical translational constraints). Figure 3.4 on the right shows bottom flange elements at the pier with the fixed bearing also modeled with the middle node (node with constrains labeled 1,2,3; which corresponds to lateral, vertical and longitudinal constrains).

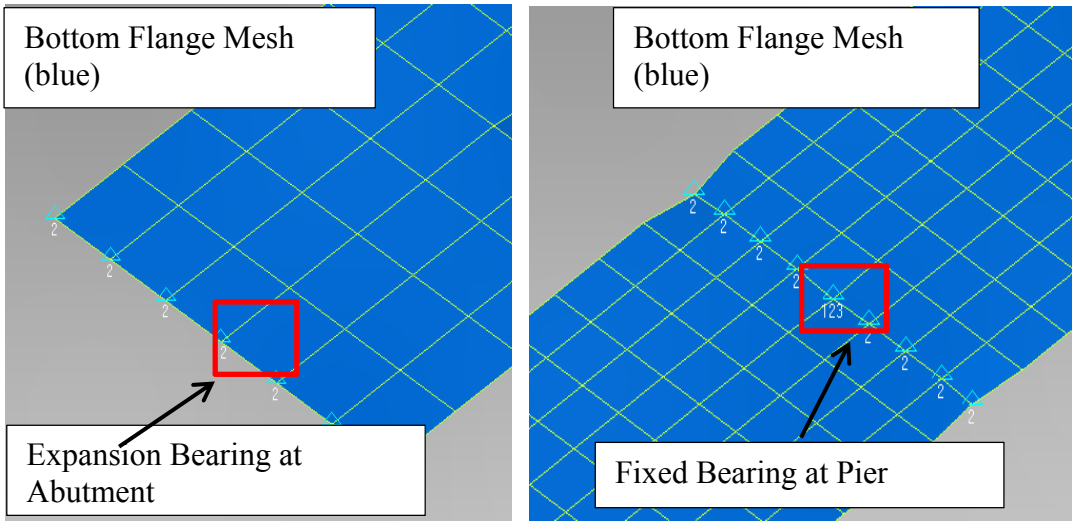

Figure 3.4 Expansion Bearing (Left) and Fixed Bearing (Right) FEM of the Bridge SR-299

3.6 **Loading**

The final step before analyzing the model in Abaqus is to apply the loading. For the preliminary models used to develop the instrumentation plan, the loading was based on a standard truck loading (AASHTO HS-20), shown in Figure 3.5, consisting of a front axle of 8 kips spaced fourteen feet from the two rear axles, each 32 kips, spaced fourteen apart.

For the preliminary analysis used to construct the instrumentation plans for field testing, four different load positions for US-13 were investigated for dead load plus live load: the first three with the truck loading centered over the center support 2 feet from the left parapet, 2 feet from the right parapet, and with the right line of truck wheels centered on the lane boundary and the last with the centroid of the truck loading positioned at 40 % of the span length from the abutment and 2 feet from the left parapet. The latter case is intended to produce the maximum moment in Girder 4,

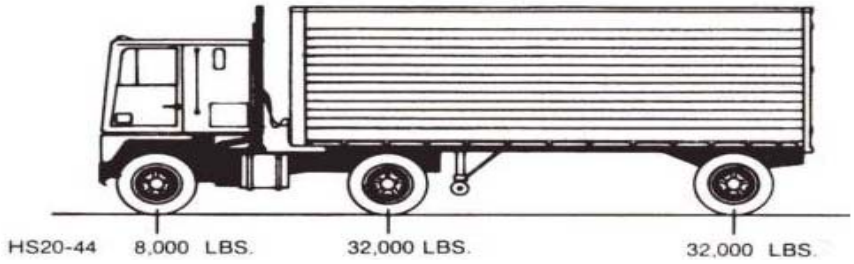

Figure 3.5 HS-20 Truck Loading (AASHTO 2010)

while the former provide additional information about the cross-frame response. The fourth case is based on the theoretical position for maximum positive moment.

For the preliminary analysis of the SR-299 model, three different load positions were investigated under dead load plus live load and live load only. The three positions were the truck loading in the obtuse corner of the bridge between girders 9 and 10 approximately 10’ from the end of the bridge, the centroid of the truck loading positioned at 40 % of the length of the 134’ span between girders 5 and 6, and the truck loading centered over the center support of the bridge. These load cases were investigated to represent three known severe loading types: load in the obtuse corner of the bridge, loading causing maximum positive moment, and loading over the location experiencing maximum negative moment. Because forces have been shown to be higher in the obtuse corner of skewed bridges, the obtuse corner load case was added. Dead load was applied in the negative vertical direction as a gravity load by adding material densities to the models. The results from the live load only case are more relevant to determining instrumentation plans since only these results will be captured by the field instrumentation.

When calibrating the models, the loading truck present during field testing was used in FEA. The field test loading truck was modeled using six point loads (one to represent each wheel), with a pair of point loads spaced six feet apart transversely to comprise each axle (Table 3.2). Front axle was 5 ft apart from the middle axle, while rear axle was 15 ft apart from the rear axle. These point loads were applied to the deck nodes.

For the model validation (Chapter 5) and static analysis portion of parametric study (Chapter 6, Section 6.3), the truck load was simulated with a series of static load cases which varied in position to represent a truck traveling across the length of the bridge. Nodal positions of each of these load cases, which were necessary to apply the loads in the model, were computed using VBA programing routine. To facilitate the use of this routine, the deck element nodes were numbered in ascending order. The routine was supplied with parameters of the loading truck axle nodal lengths and widths. The loading truck axle nodal length is computed by dividing the length between the truck's axles by the length of the deck elements, while nodal width is computed by dividing width between the truck's wheel lines by the width of the deck elements. These numbers are rounded to the closest integer, effectively approximated the distances between the wheel lines and the axles in terms of number of nodes. Then the left rear wheel of the truck are placed at Node 1 (i.e., the truck is placed at the

Table 3.2 Point Loads Used in FEMs Representing Wheel Weight of Loading Truck

Front Axle (lb)		**Middle Axle (lb)**		**Rear Axle (lb)**	
Left Side	Right Side	Left Side	Right Side	Left Side	Right Side
6693	7857	8419	12155	8120	12180

position representing the entire truck first being fully on the bridge) and the nodal position of the other left side wheels is found by adding axle nodal length parameter (number of deck nodes between two wheels) computed in previous step. The position of the right rear wheel was computed by adding nodal axle width to the left rear wheel and determining starting node number for the left rear wheel. Due to bridge skew, node number (ID) of the right real wheel and node number (ID) of left rear wheel are not the same. Once the node number (position of the right rear wheel was determined, then the nodal positions of the remaining right wheels were computed by adding axle nodal length parameter computed previously.

Once nodal positions for all six wheels were calculated, the program assigns the corresponding weights to the nodes to complete this load case. A new load case is then created by moving the left rear wheel to Node 2 and repeating the procedure of locating the other nodes where load will be applied and assigning weights of point loads at these six locations. This process repeats until right rear wheel reaches final deck node. Once the nodal loads are calculated the file is exported and compiled in a format that can be copied into Abaqus input file. Figure 3.6 shows example of programing routine output that is ready to be manually copied into Abaqus input file. First three rows in Figure 3.6 are Abaqus commands (rows that start with "*") while the following six rows are nodal positions and corresponding weights of six loading truck wheels. The loading case is finalized with another Abaqus command (*End Step). The next loading case (CASE 2) has the same Abaqus command structure, while nodal positions are increased by one number.

Initially it was planned to have loading cases analyzed for every node along the length of the deck. However, that turned out to be very impractical due to Abaqus

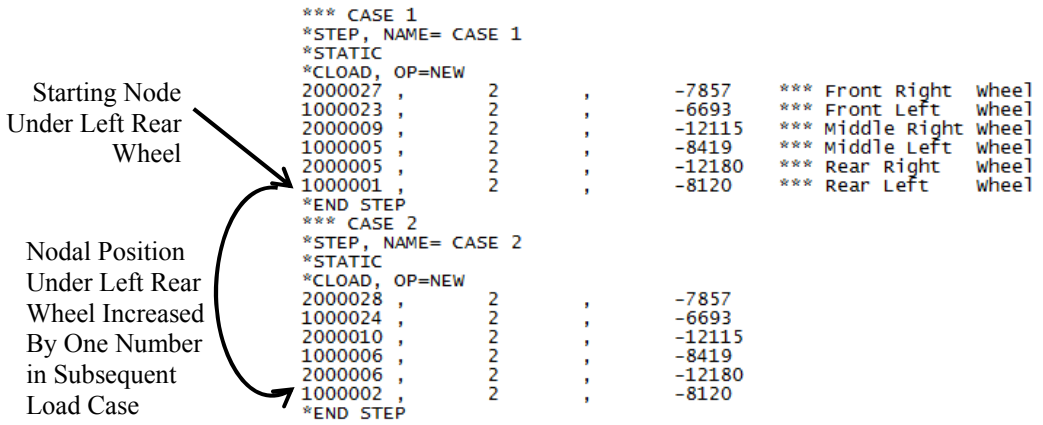

Figure 3.5 Example of Abaqus Input File Exported by VBA Programing Routine

output file size constrains (especially for the SR-299). To solve this problem load cases that were perceived not to be contributing to maximum response of the instrumented gauges were deleted from the input file and excluded from the analysis.

The exclusion criteria were based on the analysis of field test strain plots. From the field strain plots it could be seen when the strain gauges were critically engaged and when they are not. Based on this analysis, total of 136 load cases for US -13 and total of 200 load cases for SR-299 were selected and compiled to best simulate the loading conditions of a moving truck progressing along the length of the bridge. Figure 3.7 graphically shows load (truck) progression over bridge deck (FEM of US-13). The six yellow arrows represent wheel loads applied to deck nodes. The FEM of the bridge is shown in transparent mode, so the load progression with respect to the gauge locations could be properly perceived**.**

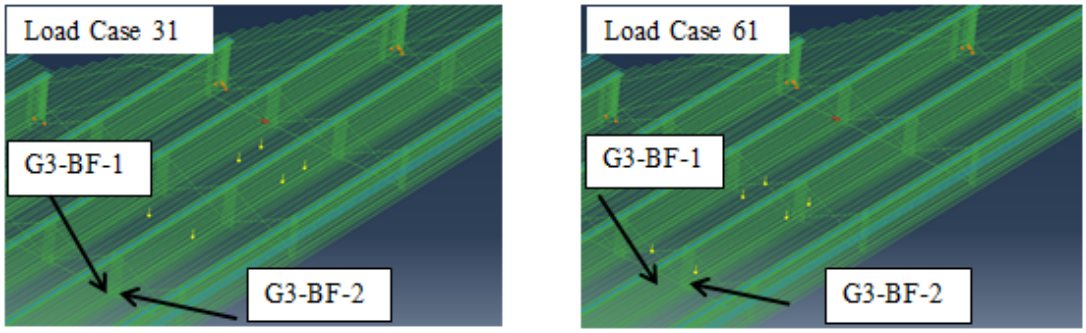

Figure 3.6 Moving Load Applied to FEM of US-13

This loading procedure allowed the varying effects of the moving load to be efficiently assessed as the load position causing the maximum force effect was neither readily known with certainty nor consistent for all gauge locations.

3.7 **Analysis**

After all of the modeling was completed, output from the pre-processing program was used to create an ABAQUS input file. Once the FEA was processed, initial evaluation of these results included visualization of the output to ensure all connections were properly implemented, that stresses were in the correct range of magnitude, and that the relative magnitudes of stress displayed in various elements were logical. The analysis was an implicit analysis which means the dependent variables were defined by coupled sets of equations and solved through an iterative technique. Linear-elastic, static analysis assuming elastic material properties and geometric linearity was used in the FEA reproducing the field work, which is described in Chapter 5.

For the parametric analysis described in Chapter 6, Section 6.4., where the bridge models (FEM of different cross-frame configurations of US-13) are loaded past

their yield point, the analysis was performed using the Riks method of analysis. This method is generally used to predict unstable, geometrically nonlinear collapse of a structure and can include nonlinear materials, nonlinear geometry and boundary conditions. This method uses the load magnitude as an additional unknown and solves simultaneously for loads and displacements. The load case that produced the highest bottom flange stress at US-13, was used as a input of initial load magnitudes in Riks method.

3.8 **Future Work Considerations**

Any improvements made to the existing methodology should take into consideration the available computing power. Both FEMs (US-13 and SR-299) created for these projects were extremely large models (well over 100,000 elements and over 500,000 nodes). To successfully handle pre and post file processing, a significant investment in powerful computing machines is needed. For the large file preprocessing, customer service of the preprocessing software (Femap 11.0.) recommended that RAM memory of at least 10GB. Additionally, 10GB RAM memory should be accompanied with graphic card memory of 1GB. Initially, 1GB RAM memory and graphic card of GB was used in file pre and post processing.

This insufficient computing power caused modeling and results compiling long and laboring process with frequent interruptions due to system overload. Once a new, more powerful computer was acquired, modeling time was reduced from several weeks to several days. Finally, high performance computing processors are needed in order to efficiently analyze models of this scale, particularly the non-linear models described in Chapter 6. The state-of-the-art high performance computing (HPC)

machines consisting of dual-socket processors with 12-cores per socket and 64 GB RAM processor were used for processing purposes. Even with all this computing power, it would take between 45 minutes to 1 hour an 20 minutes to process SR-299 linear-elastic analysis model containing 200 load cases. It would take additional 2 hours to transfer processed file from the HPC location to local machine where further post processing would take place.

Additionally, it would take between two to four hours to process the various non-linear modifications of US-13 discussed in Chapter 6. In addition to processing demands, the requirements for post-processing should also be considered. The files containing the visualization of the post-processing file were in the range of 17GB for the US-13 (Riks method) to 57GB for the SR-299. Manipulating and archiving this data also necessitates ample computing resources.

Chapter 4

FIELD TESTING

Two bridges of varying skews, SR 1 over US 13 and SR 299 over SR 1, both located in New Castle County, Delaware, were selected for field testing. SR 1 over US 13 is a 65 degree skew bridge with X-type cross-frames, while SR 299 over US 13 is a 32 degree skew bridge with K-type cross-frames. Between both bridges, 11 different cross-frames and 6 different girder locations were instrumented using BDI ST-350 strain transducers. Gauges were clamped at selected cross-frame and bottom flange locations and bonded at web locations. The bridges were loaded with multiple passes of a weighed test vehicle provided by the Delaware Department of Transportation (DelDOT).

A truck with a man-lift was also provided by DelDOT to facilitate gauge installation. They also facilitated lane closures in order to ensure safe access to all testing locations and maintenance of traffic. This chapter explains the selection of the BDI strain transducers, the instrumentation layouts for both bridges, and the loading of the bridges used for testing. It also highlights how the data from the tests was processed, presents the data, and includes recommendations for future similar field tests.

4.1 Gauge Type and Data Collection

BDI ST-350 strain transducers and their associated structural testing system were used in field testing. BDI strain transducers are larger and easier to handle and install than traditional foil type gauges. The ease in installation stems from their ability to be clamped in place on cross-frame angles and flanges, eliminating the need from

fastening through welds or adhesives. This ease in installation was the primary criteria leading to the selection of this testing system since both bridges that were tested serve as highway overpasses. Thus, installation time was critical because lane closures were necessary to install much of the instrumentation and minimizing lane closure time was of importance.

Figure 4.1 demonstrates two BDI strain transducers clamped onto each leg of a cross-frame angle section. When clamping was not possible, which was the case at web locations, steel tabs were connected to the gauges using small bolts and bonded to the steel surface using an adhesive. A small surface area of paint was grinded to remove it prior to installation of the gauge to ensure proper adherence when gauges were bonded. Figure 4.2 demonstrates a BDI strain transducer bonded to a girder web.

Figure 4.1 Clamped BDI Strain Transducers

Figure 4.2 Bonded BDI Strain Transducer

The BDI strain transducers have a strain range of ± 4000με and are individually calibrated to ± 2 % per NIST standards (Bridge Diagnostics, 2006). A calibration certificate is provided by the company with each transducer. Each strain transducer is a full Wheatstone bridge with four active 350W foil gauges and a four wire hookup (Bridge Diagnostics, 2006). Bridge Diagnostics, Inc. supplies each transducer with an identification number and a calibration factor that are incorporated into the data acquisition system in order to ensure accuracy of results.

4.2 Instrumentation Layout

The field testing equipment owned by the University of Delaware has the capability to record 36 BDI strain transducers at one time; therefore it was decided to conduct each bridge test in two phases utilizing all or most of the strain transducers in each test in order to maximize the amount of data that could be recorded at each bridge. Two days were allotted for testing at each bridge and the gauges were broken

down into groups to be tested on each day. There was overlap of the testing locations between the two days in order to be able to assess uniformity between tests completed over the course of multiple days.

Between both bridges, 11 different cross-frame locations and 6 different girder locations were instrumented in order to record data at cross-frames and their adjacent girders. Through instrumenting the adjacent girders, the global response of the structure in the vicinity of the cross-frames will be known, which will provide insight into the cross-frame behavior and assist in future FEA calibration efforts. Preliminary finite element models created for each bridge were used to determine locations of interest and produce an instrumentation layout.

While the instrumentation plan for each bridge was unique, there were similarities between the two. Three girder locations were instrumented on each bridge, with a gauge on each side of the vertical axis of the bottom flange and a gauge on each side of the web at mid-height. The same labeling system was used at the girder locations on each bridge. Girder locations are labeled as G followed by a number that corresponds to a sequential numbering of the girder cross-sections that were instrumented (for example G1). BF-1 and BF-2 represent the two bottom flange gauges, while W-1 and W-2 represent the two web gauges. For SR 1 over US 13, BF-1 and BF-2 are always on the west and east sides of the girder, respectively, while for SR 299 over SR 1, BF-1 and BF-2 are always on the north and south sides of the girder, respectively.

Since the cross-frame type differed between the two bridges, the cross-frame labeling system differed slightly between the two bridges. However, in both bridges the cross-frames are labeled with two numbers. The first number corresponds to the

longitudinal position of the cross-frame on the bridge and the second number refers to its transverse position. An example of the cross-frame numbering can be seen in Figure 4.3. Cross-frame gauges were then labeled by the cross-frame number followed by a letter that corresponded to the location on the cross-frame. For example, Cross-frame 12-4-A corresponds to the twelfth longitudinal line of cross-frames at the fourth transverse positioning with Location A instrumented, where the letter designation represents the same location (e.g., west end of bottom chord) on each cross-frame within a given bridge. The following subsections detail the specific locations instrumented for each bridge

4.2.1 **SR 1 over US 13**

The instrumentation layout for SR 1 over US 13 consisted of fifty-nine unique positions for strain gauges. Multiple points on five cross-frames and three girder cross-sections were instrumented. Specifically, the cross-frames instrumented were Cross-frame numbers 4-4, 11-3, 12-3, 12-4, and 14-3 and Girder locations G1, G2, and G3 as identified in Figure 4.3. The instrumentation plan was developed using the finite element analysis of the bridge under several loading conditions as previously discussed in Chapter 3 to determine areas of interest. Peak cross-frame forces and adjacent girder locations were investigated under dead load plus live load of an HS-20 truck (AASHTO 2010) in four different load positions: the first three with the truck loading centered over the center support 2 feet from the left parapet, 2 feet from the right parapet, and with the right line of truck wheels centered on the lane boundary and the last load case with the truck loading positioned at 40 % of the span length from the abutment and 2 feet from the left parapet. The latter case is intended to

produce the maximum moment in Girder 4, while the former provide additional information about the cross-frame response. Each of the cross-frames instrumented were ones that exhibited peak stresses under the four loading scenarios investigated; therefore they and their adjacent girder locations were chosen for testing. All cross-frames that were selected for instrumentation frame into a common girder (Girder 4, labeled as "G4", the fourth girder from the top of in Fig. 4.3) to enable recording the range of responses occurring as the longitudinal position of the cross-frame varies while attempting to minimize the number of girder locations that would need to be instrumented in order to have a basis for comparison to the cross-frame data and keep the overall number of gauges to a minimum. All members of the cross-frames were investigated and instrumentation was placed on members that exhibited highest stresses.

Each of the three girder locations, which were selected because of their position adjacent to instrumented cross-frames, has four strain gauges, one on each side of the web (W-1 and W-2) and two on the bottom of the bottom flange (BF-1 and BF-2) as seen in Figure 4.4 below. These girder locations allow for the stresses at these sites to be correlated to the stresses in the adjacent cross-frame. The position of the gauges within these cross-sections was chosen in order to assess the variation of stresses throughout the girder cross-section and to locate the neutral axis of the girder location. Specifically, by installing two gauges at each height, lateral bending effects can be captured and redundancy in the data is obtained in the event of a malfunctioning gauge.

Because of limitations imposed by the number of data channels that could be connected to the data acquisition system, gauges were not placed on the top flange

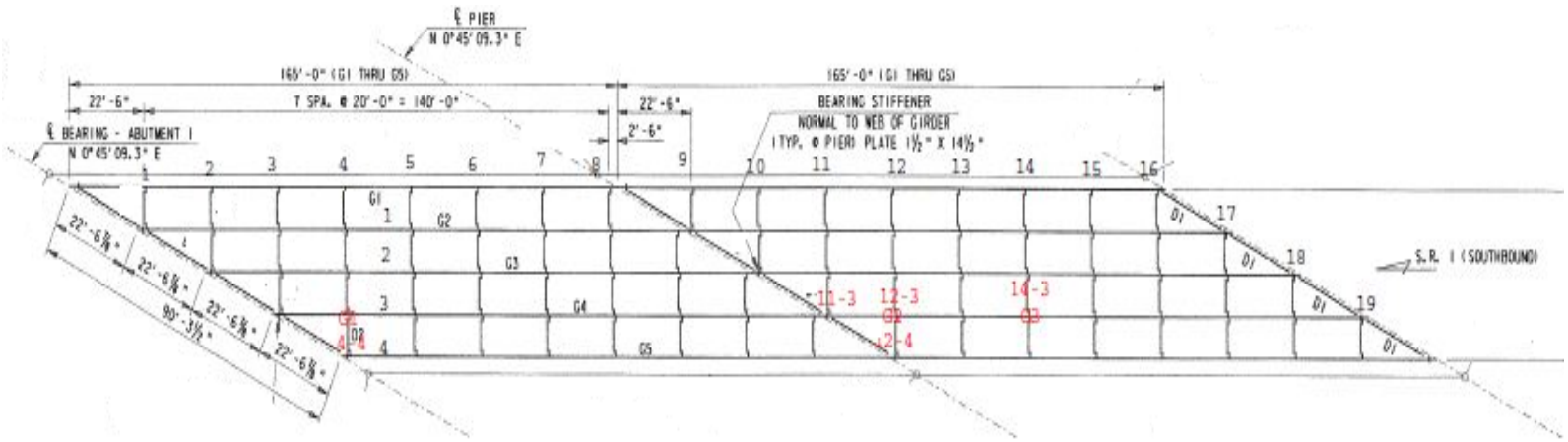

Figure 4.3 SR 1 Over US 13 Instrumentation Layout

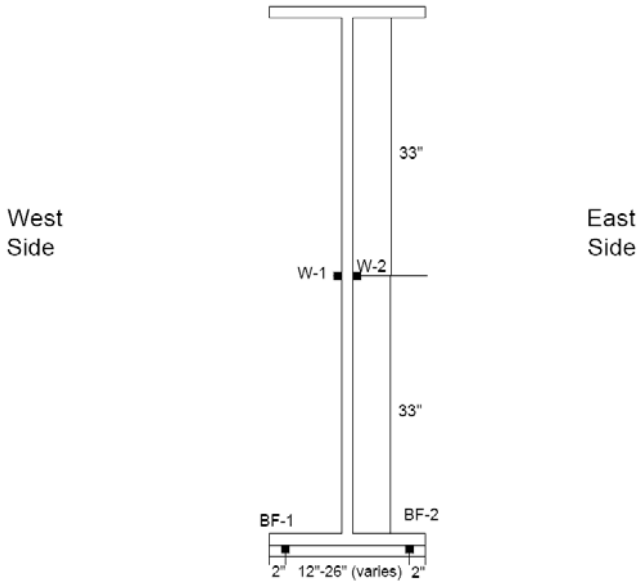

Figure 4.4 Girder Strain Gauges Cross-Section Labeling System, SR 1 Over US-13

because composite action with the deck would cause these strains to be very small and thus difficult to accurately capture.

Girder locations 2 and 3 were fully instrumented (W-1, W-2, BF-1, and BF-2) on the first day of testing. On the second day of testing, Girder locations 1 and 2 were fully instrumented (W-1, W-2, BF-1, and BF-2). Therefore, there was an overlap between the gauges (W-1, W-2, BF-1, and BF-2) at Girder location 2 between the two days of testing. Figure 4.4 shows the labeling system that was used for the girder strain gauges.

Each of the five cross-frames chosen was instrumented with slight differences to reflect where peak stresses occurred in the preliminary finite element analyses. Five cross-frames were chosen, reflecting the areas of highest stress shown

by the results of the finite element model (as described above). Each of the cross-sections that were instrumented was labeled A thru J (as shown in Fig. 4.5) such that the same label applied to the same location on each cross-frame. For example, as shown in Fig. 4.5, the bottom east side of the inclined member, three inches from the connection plate, is always referenced as location H. Note all gauges are placed three inches from connection plates. Each cross-section typically had two gauges, one on each leg of the angle, but in some cases only the concentric leg of the angle is instrumented. This occurs in less critical locations when instrumentation is limited. Table 4.1 specifies which positions were instrumented on each cross-fame by indicating the number of legs instrumented at that location.

The finite element analysis tended to show one of the inclined members of the cross-frame as containing significantly higher stresses than the other inclined member. In each loading scenario, this was the inclined member that framed into the top of Girder 4. Two cross-sections were instrumented on whichever of the two inclined

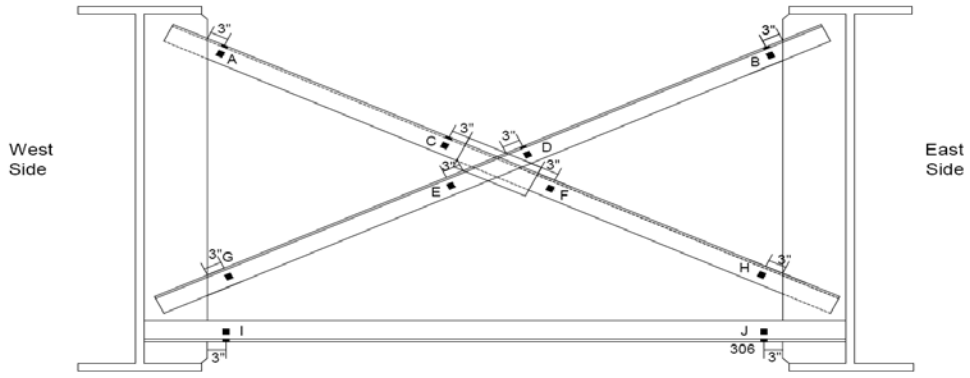

Figure 4.5 Cross-frame Strain Gauges Cross-Section Labeling, SR 1 over US-13

Table 4.1 Number of Gauges per Location, SR 1 over US 13

	Number of Gauges at Location										
Cross-frame	A	B	C	D	E	F	G	H	I	J	Total
4-4	2		2		2		1		2	2	11
11-3		1				1		2	2	2	8
12-3		2		2				2	2	2	10
12-4	2		2				1		2	2	9
14-3		1				2		2	2	2	9

members demonstrated highest stresses, one three inches from the connection plate to the girder (Location A, B, G, or H) and one three inches off the plate that connects the two angles, on the side closest to the gauge already placed (Location C, D, E, or F) to evaluate bending throughout the member. The gauges were placed on the end of the angle that demonstrated the highest stresses. At each of these cross-sections, two gauges were placed, one on each leg of the angle.

Two cross-sections were instrumented on the bottom chord of the cross-frame, three inches off the connection plate on each side (Locations I and J). This chord experienced lower, but still significant, stresses than the inclined member already instrumented; therefore two gauges were placed at each cross-section.

For four of the cross-frames (12-3, 12-4, 11-3, and 14-3), only one cross-section was instrumented on the second inclined member. Here the finite element analysis reported relatively low stresses so a gauge was placed on the same side (i.e. east or west) of the angle that gauges on the higher stress angle were oriented. For example, in Cross-frame 12-4, Locations B and D correspond to the anticipated locations of highest stress, so Location H is also instrumented since it is also on the east side of the cross-frame. Due to limitations with equipment and relatively low predicted stresses, only one gauge was placed at these cross-sections. For the fifth

cross-frame (4-4), both of the inclined members experienced significant stresses in the finite element analysis; therefore two cross-sections were also selected for the remaining angle with these gauges also oriented on the west side of the members, as was done for the other inclined angle of the cross-frame.

The field tests for SR1 over US13 were conducted on Friday, December 2nd, 2011 and Monday, December 5th, 2011. On Day 1 of the field tests (Dec. 2nd), Cross-frames 12-3, 12-4, and 14-3, along with Girder locations 2 and 3 were instrumented and tested. At the end of the day, all of the equipment was removed. On Day 2 of the field tests (Dec. 5th), Cross-frames 4-4 and 11-3, as well as Girder locations 1 and 2 were instrumented and tested. Because of time limitations and difficulty of set-up due to testing at two locations in the bridge requiring a time-consuming process to connect the two segments of instrumentation over traffic lanes, fewer locations were tested on Day 2 than originally planned. This was not a significant detriment to the testing plans as the cross-sections that were not tested as planned were a repetition of cross-sections on Cross-frame 12-4 that were tested the previous day. On both days, the data acquisition system was set up in the median of the underpass roadway, approximately beneath Girder Four. Overall, 47 unique locations were instrumented on five different cross-frames and 12 unique locations were instrumented on three different girder cross-sections over the two days of testing.

4.2.2 **SR 299 over US 13**

The instrumentation layout for SR 299 over SR 1 consisted of sixty-two strain gauges. Multiple points on six cross-frames and three girder cross-sections were instrumented. Specifically, the cross-frames instrumented were Cross-frames 8-4, 12-

4, 12-5, 14-8, 14-9, and 14-10 and Girder locations G1, G2, and G3 as identified in Figure 4.6. G1 is position halfway between the stagger between Cross-frames 12-4 and 12-5, while G2 is at Cross-frame 12-4. The instrumentation plan was developed using FEA under various loading conditions as described in Chapter 3 to determine areas of peak stresses. Each of the instrumented cross-frames exhibited peak stresses under the loading scenarios considered, therefore they and their adjacent girder locations were chosen for testing. The general positions of the cross-frames selected for testing include three cross-frames in line with one another in the obtuse corner of the bridge, a cross-frame at the pier, and cross-frames at the maximum positive moment location for Girder 5.

As with SR 1 over US 13, discussed in the previous section, each of the three girder locations, which were selected because of their position adjacent to instrumented cross-frames (in the obtuse corner of the bridge and at the maximum positive moment location for Girder 5), has four strain gauges, one on each side of the web (W-1 and W-2) and two on the bottom of the bottom flange (BF-1 and BF-2) as seen in Figure 4.7. This was selected in order to assess the variation of stresses throughout the girder cross-section and to locate the neutral axis of the girder location. Because of limitations imposed by the amount of data channels that could be connected to the data acquisition system, gauges were not placed on the top flange because composite action with the deck would cause these strains to be very small and thus difficult to accurately capture. The same labeling system used for SR 1 over US 13 for girder locations was used as demonstrated by Figure 4.7 above. Girder location 3 was fully instrumented (W-1, W-2, BF-1, and BF-2) on the first day of testing, while

only the bottom flange locations (BF-1 and BF-2) were instrumented at Girder locations 1 and 2 on that day.

On the second day of testing, Girder locations 1 and 2 were fully instrumented (W-1, W-2, BF-1, and BF-2). Therefore, there was an overlap between the bottom flange gauges (BF-1 and BF-2) at Girder locations 1 and 2 between the two days of testing. Each of the six cross-frames chosen was instrumented with slight differences to reflect where peak stresses occurred in the preliminary finite element analysis and to capture the transfer of the force from the girders through the cross-frames. Six cross-frames were chosen, reflecting the areas of highest stress shown by the results of the finite element model. Each of the cross-sections that were instrumented was labeled A thru H (see Fig. 4.8 for locations of these cross-sections) so that the same label applied for the same location on each cross-frame. For example, as shown in Figure 4.8 the top south side of the inclined member, three inches from the connection plate, is always referenced as Location B. Note all gauges are placed 3" from the connection plates. Each location had two gauges, one on each leg of the angle. Table 4.2 below specifies which positions were instrumented on each cross-frame by indicating the number of legs instrumented at that location, which is two for all cases for this bridge.

The gauge locations on the different members of the cross-frames were also based on the locations of highest stress as seen in the finite element analysis, which tended to show one of the inclined members of the cross-frame as containing significantly higher stresses. Two cross-sections were instrumented for the inclined member that demonstrated highest stresses, Locations A and C or Locations B and D

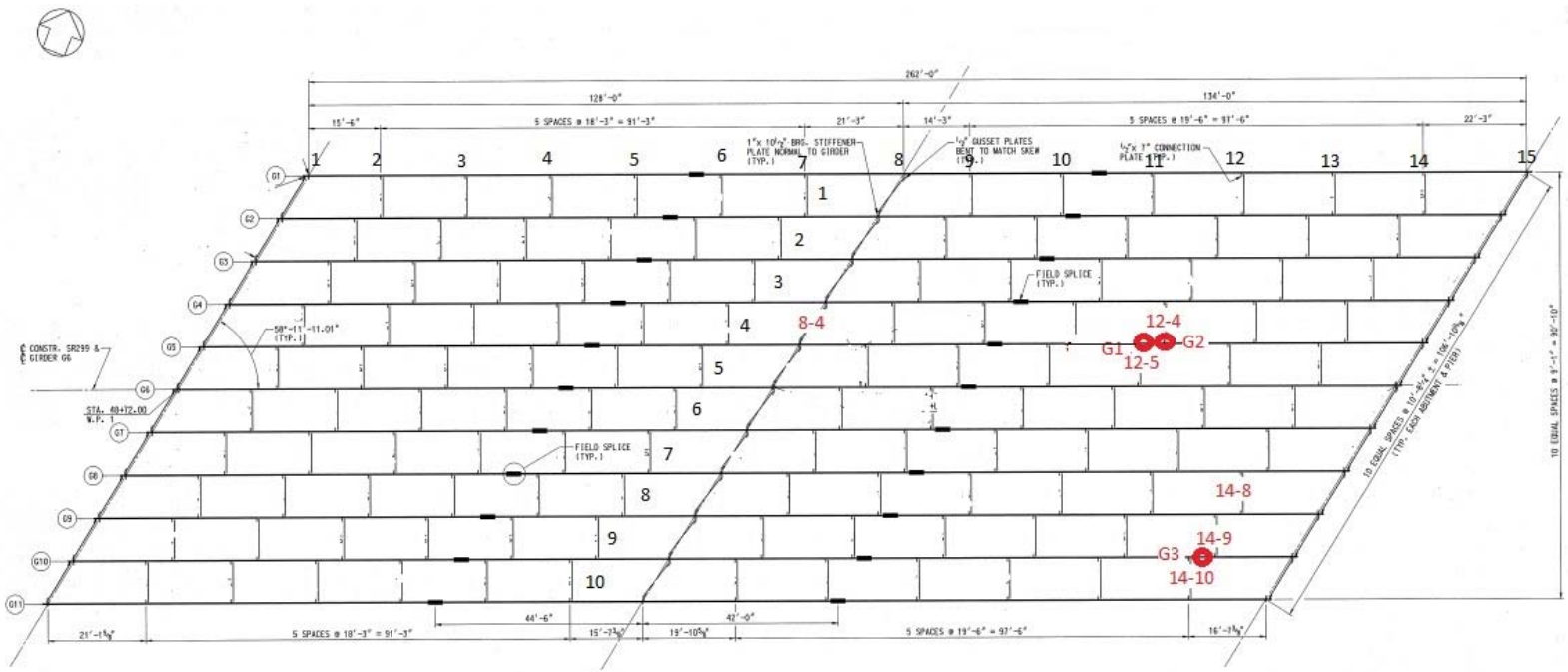

Figure 4.6 SR 299 Over SR 1 Instrumentation Layout

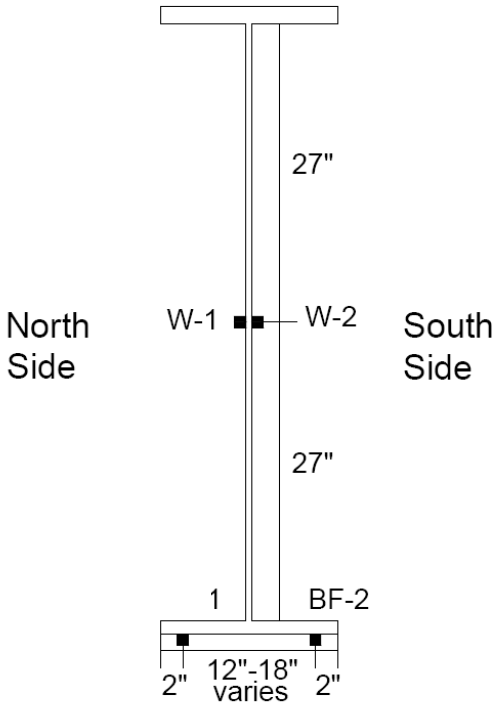

Figure 4.7 Girder Strain Gauges Cross-Section Labeling System, SR 299 Over SR 1

depending on whether the north or south side member demonstrated highest stresses. For Cross-frames 12-4, 12-5, 14-9, and 14-10, the side with the highest stresses that was chosen for instrumentation also coincided with the side where the adjacent instrumented girder was located. Girder locations were not instrumented at Cross-frames 8-4 and 14-8 due to limitations with the amount of gauges available. At each cross-frame, two cross-sections were instrumented on the bottom chord: E and F if the north side inclined member was instrumented or Locations at G and H if the south side inclined member was instrumented. For Cross-frame 14-9, Location E (not on the same side as the inclined member that was instrumented) on the bottom chord, was

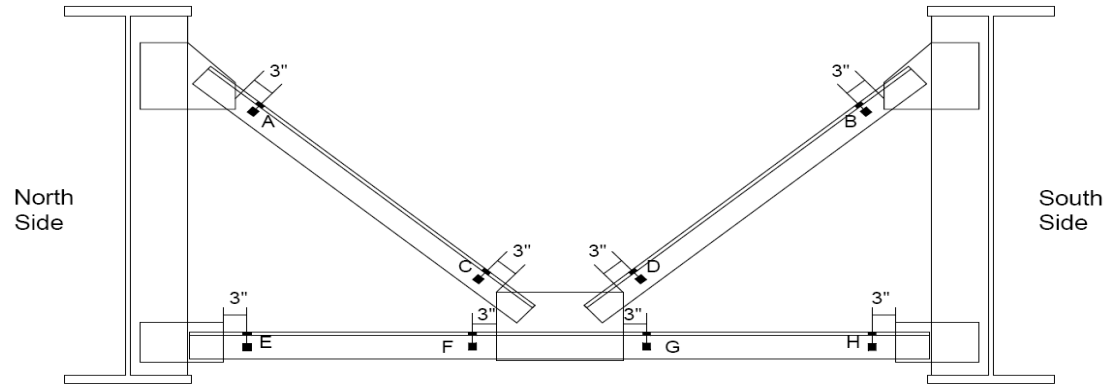

Figure 4.8 Cross-frame Strain Gauges Cross-Section Labeling, SR 299 over SR 1

Table 4.2 Number of Gauges per Location, SR 299 over SR 1

	Number of Gauges at Location								
Cross-frame	A	B	C	D	E	F	G	H	Total
8-4		2		2			2	2	8
12-4		2		2			2	2	8
12-5	2		2		2	2			8
14-8		2		2			2	2	8
14-9		2		2	2		2	2	10
14-10	2		2		2	2			8

also instrumented to compare the forces in the cross-frames at this location on both sides of Girder 9. Specifically, since there were three adjacent cross-frames (14-8, 14-9, and 14-10, see Fig. 4.6) instrumented and Cross-frame 14-9 was the middle cross-frame of the grouping, this location was selected in order to collect data throughout the bottom chord in an effort to relate the data to Cross-frames 14-8 and 14-10, the cross-frames on either side of Cross-frame 14-9. Thus, each cross-frame was instrumented with 8 or 10 strain gauges.

The field tests for SR 299 over SR 1 were conducted on Wednesday, November 30th, 2011 and Thursday, December 1st, 2011. On Day 1 of the field tests (Nov. 30th), Cross-frames 14-8, 14-9, and 14-10, along with Girder location 3 and the bottom flange locations on Girder locations 1 and 2 were instrumented and tested. At the end of the day, all of the equipment was removed. On Day 2 of the field tests (Dec. 1st), Cross-frames 8-4, 12-4, and 12-5 as well as Girder locations 1 and 2 were instrumented and tested. Thus, the data at bottom flange gauge locations on Girder locations 1 and 2 were recorded on both days of testing to capture any differences in the data between the two days. On both days, the data acquisition system was set up underneath the bridge on the outside shoulder of the underpass, northbound SR 1. Overall, 50 gauges were instrumented on six different cross-frames and 12 gauges were instrumented on three different girder cross-sections over the two days of testing.

4.3 **Loading Vehicle**

On each testing day, DelDOT provided a loaded tri-axle dump truck (Fig. 4.9) to use as the test vehicle. The vehicle was outfitted with a large plow on the right side which, at least in part, caused the weights on the right side of the vehicle to be higher. The same dump truck was provided each day and remained loaded throughout the week during which the testing was conducted.

On the first two days of testing each wheel was weighed using Intercomp Model PT 300 Wheel Load Weigher scales. Individual wheel weights were recorded by using two scales to weigh one axle at a time. Two other scales were placed under the wheels of the nearest adjacent axle during measurement in an effort to keep the truck level and account for the variation in weight distribution that may occur due to

the truck's suspension system. The results of this process for each day of testing is referred to as Measurement 1 and Measurement 2, (see Table 4.3). On the second day, DelDOT also took the truck to their scale house and provided a report of the recorded weights of each axle. There is a maximum of 3 % difference for the front axle, 3 % difference for the middle axle, and 1 % difference for the rear axle between the total axle weights of the three different measurements for each of the axles.

In order to determine an averaged weight to use in the finite element analysis, the percentage of the total axle weight measured in each individual wheel load was calculated for Measurements 1 and 2 in order to determine the distribution of weight between the two wheels of the axle (the large plow on the right side caused heavier weights on the right side). The weight distribution of the two wheels within each axle between the two measurements was within 1 %. The percentages of the total axle weight for each wheel were averaged for each axle and the averaged percentages were used to distribute the axle weight recorded at the scale house. The individual wheel weights were then averaged to calculate values to use in the finite element analysis. These measured weights as well as the averaged weight that was used in the finite element analysis can be found in Table 4.3.

Table 4.3 Tri-axle Dump Truck Weights

	Front Axle		**Middle Axle**		**Rear Axle**	
	Left Side	Right Side	Left Side	Right Side	Left Side	Right Side
Wheel Measurement 1	6690 lb	7850 lb	8330 lb	12140 lb	8250 lb	12070 lb
Wheel Measurement 2	6490 lb	7840 lb	8440 lb	12430 lb	8060 lb	12280 lb
Scale House	14780 lb		20260 lb		20240 lb	
FEA	6693 lb	7857 lb	8419 lb	12155 lb	8120 lb	12180 lb

Figure 4.9 DelDOT Triaxle Dump Truck

4.4 Truck Passes

The load tests for each of the bridges were conducted by driving the triaxle dump truck provided by DelDOT and mentioned in Section 4.3 in a series of passes across the bridge. Before each truck pass, traffic on the bridge was stopped and the strain gauges were balanced with no live load on the bridge. The truck then drove across various predetermined transverse positions at approximately 10 to 15 mph while other traffic was stopped. The transverse positions were selected by determining positions of the truck that would either maximize stress in different instrumented sections of the bridge or induce differential displacements at opposite ends of instrumentation while following markings on the roadway that would be easy for the driver to follow. The specific transverse positions for each bridge are discussed in the following subsections.

4.4.1 **SR 1 over US 13**

Three different truck passes were conducted for the load test of SR 1 over US 13. The same three passes were used on both days of testing and are depicted in Figure 4.10. Pass 1 had the dump truck travel down the center of the left lane. This position was intended to maximize the stress in the instrumented girder, G4, and induce differential displacements in the instrumented cross-frames. Pass 2 had the dump truck travel straddling the center line of the two lanes. This pass is intended to produce a high level of stress in each of the girders (G3 and G4) to which the majority of the cross-frames are connected.

Pass 3 had the dump truck travel with the left side wheels aligned with the center line of the two lanes, intending to maximize the stress in the girder at the other end of the majority of the instrumented cross-frames, G3, and produce differential displacements between the two ends of the cross-frame. Thus, the passes were generally shifted to the side of the bridge closest to where the instrumentation was installed. Data was recorded for each of these three passes on both days of testing. Figure 4.11 shows each of the passes in photograph, where it can be seen that the actual position of the truck is closer to the lane boundary than intended for Pass 1, but the actual position of Pass 2 and Pass 3 is in accordance with the testing plan. However, the difference between the point loadings depicted in the figures and the actual centroid of the wheel width is a slight difference that was noted for its potential effect on future FEA calibration efforts.

4.4.2 **SR 299 Over SR 1**

Two different truck passes were conducted for the load test of SR 299 over SR 1. The location of the two passes was intended to be the same for both days of testing, but differed slightly between the two days due to a miscommunication with the driver of the dump truck. On the first day of testing, Pass 1 had the dump truck travel westbound across the bridge with the outside of its left set of wheels on the edge of the left lane boundary as marked on the roadway (excluding the turning lane) and shown in Fig. 4.12. On the second day of testing, for Pass 1 the dump truck traveled westbound across the bridge approximately 1 foot to the right of the left lane boundary and the Day 1 position as shown in Fig. 4.12. Fig. 4.13 shows that Pass 2 for the first day of testing consisted of the dump truck traveling eastbound across the bridge about 1 foot to the inside of the right side yellow line. Fig. 4.13 also shows that Pass 2 for the second day of testing the dump truck traveled eastbound with the outside of its left set of wheels on the edge of the right lane boundary.

4.5 **Data**

After four days of field testing, during which data was collected for 11 different cross-frames and 6 different girder cross-sections, a large amount of data had been collected and needed to be processed. All of the gauges were balanced using the data acquisition system after traffic was stopped on the bridge and prior to the truck passes, but once transferred from the data acquisition system the data still had to be "zeroed", or processed so that the starting value of the data when no live load was on the bridge was zero. This was done by averaging the first 20 data points collected at each gauge and subtracting that average from every data point of that gauge. Data on

the first day of field testing (Nov. 30th, SR 299 over SR 1) was collected at a sample rate of 5 Hz, meaning 5 data points were collected each second. On the remaining days of testing, the sample rate was increased to 20 Hz, or 20 data points per second.

The increase in sample rate was decided after a quick analysis of the data from Day 1 suggested a higher sample rate would yield more data points and perhaps smoother trends in the data. All of the data was processed in MATLAB by using the "smooth" function to take a 5-point moving average of the data. This eliminated a large amount of noise in the data. In order to graphically represent this data, a short MATLAB script was written that smoothed the original data as mentioned previously and down sampled the data (only graphed every 20th data point) in order to create uniform plots with the same formatting for each gauge. An example of the time versus strain plot created for Girder locations 1 and 2 for SR 299 over SR 1 on Day 1 of testing is shown in Figure 4.14. The x-axis represents time in seconds and the y-axis represents micro-strain (which is the strain multiplied by 10^6). The series labels in the legend include the identification number of the gauge followed by the designation of its location (for example, B1477, G1-BF-1). The complete set of time versus strain plots for every location tested can be found in Ambrose (2012).

Using the data that was balanced and smoothed by taking a moving average, the maximum strain values (εMAX) for each gauge for each pass were tabulated. These maximum strain values were converted to stresses (σMAX) by multiplying by the standard value for modulus of elasticity of steel (29,000 ksi). At cross-sections where there were two gauges, the maximum stress values were averaged (σMAX-

AVG). The maximum values for the girder locations (when gauge was tested on two days the maximum of the two days was considered) of SR 1 over US 13 are presented in Table 4.4, while the maximum values for the cross-frames of SR 1 over US 13 are presented in Tables 4.5, 4.6, 4.7, and 4.8.

The maximum values for the girder locations of SR 299 over SR 1 are presented in Table 4.9, while the maximum values for the cross-frames of SR 299 over SR 1 are presented in Tables 4.10 and 4.11. It is noted that the values are not at concurrent times, including bottom flange and web data, so this data should be used purely for understanding maximum force effects and not be used for evaluating load distribution. When a gauge did not balance, it is denoted by the letters "NB", but the data is not treated differently. Other possible errors in gauges functioning are noted as footnotes to the tables as needed.

Trends in the bottom flange test data, which is the best measure available of global response, are generally as expected. For SR 1 over US 13, the bottom flange gauges at Girder Location 3 exhibit the highest tensile stresses, as expected, and the bottom flange gauges at Girder Location 2, the location where the highest negative moments is expected, exhibit the highest compressive stresses. Also for SR 1 over US 13, in general the bottom flange stresses for Pass 1 are greater than for Pass 2 which are greater than Pass 3, which is expected as the truck load moves farther from the instrumented girder. For SR 299 over SR 1, the bottom flange stresses for Girder Locations 1 and 2 are similar as is expected since the two locations are in close proximity to one another. Furthermore the peak stresses at these locations are

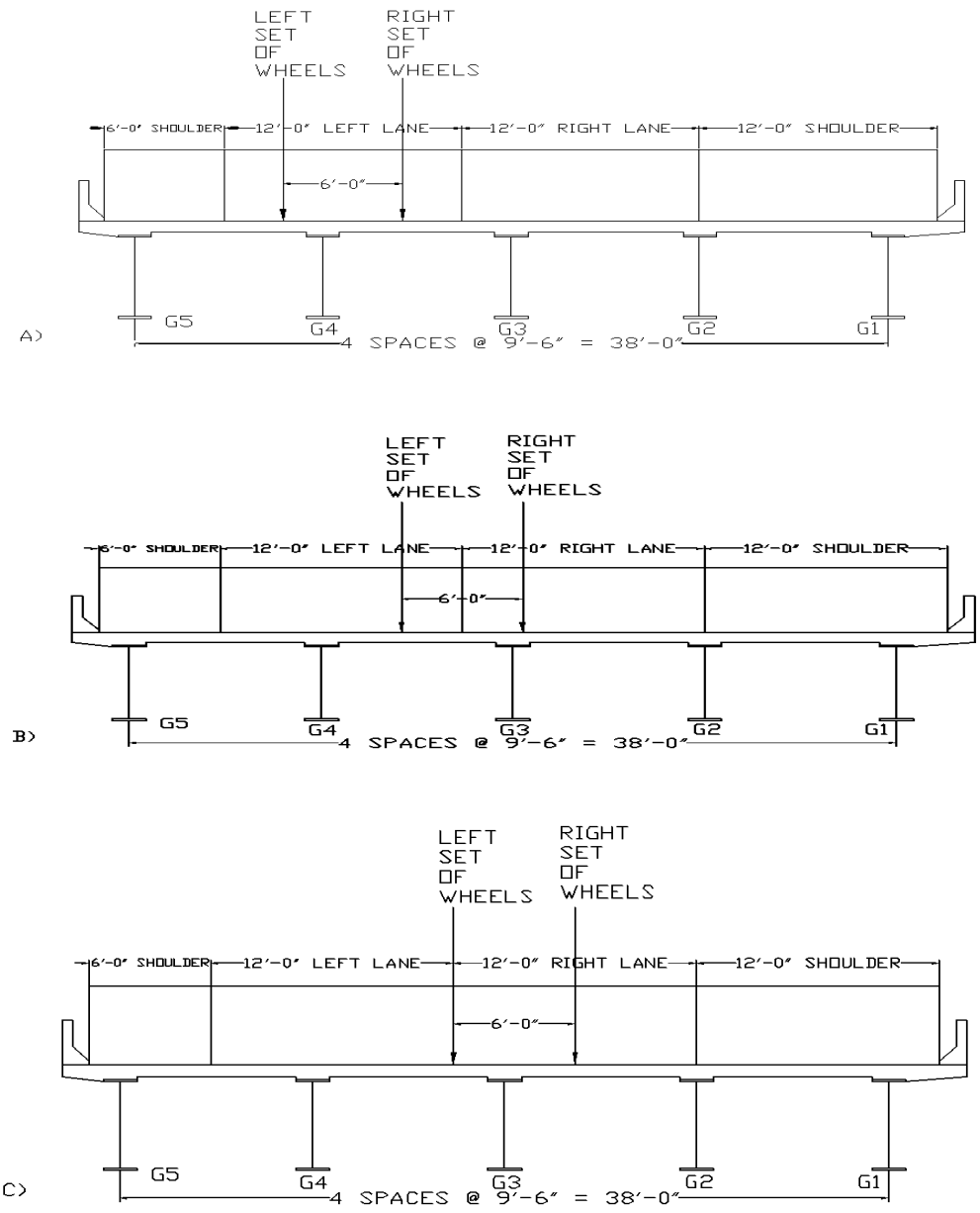

Figure 4.10 Truck Passes for SR 1 Over US 13: A) Pass 1: Center of Left Lane, B) Pass 2: Straddle Center Line, C) Pass 3: Left Wheels on Center Line

A)

B)

Figure 4.11 Photographs of Truck Passes for SR 1 Over US 13: A) Pass 1, B) Pass 2, C) Pass 3

C) 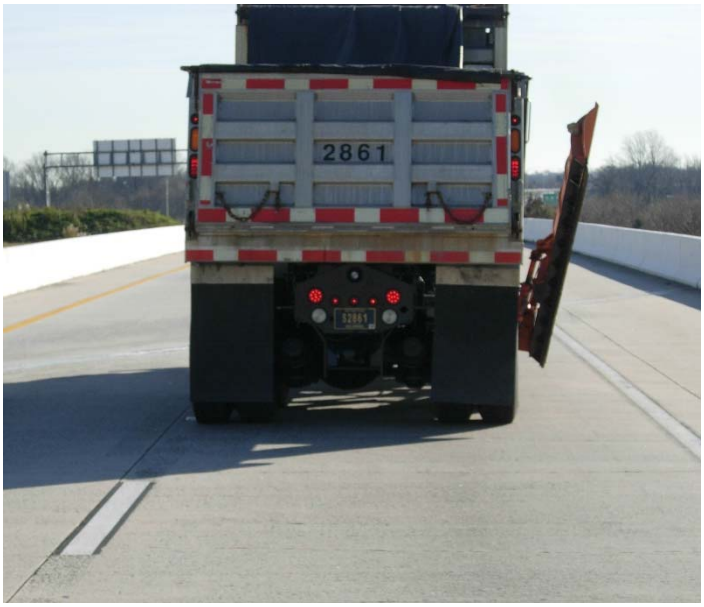

Figure 4.11 Continued

greater than the peak stresses at G3, which is closer to the abutment and thus should experience less moment. It is also logical that the stresses in G1 and G2 are maximized by Pass 1, since this loading is closest to these gauge locations, while the peak stresses in G3 occur under Pass 2, which travels closest to this gauge location.

As mentioned in the literature review in Chapter 2, Bishara and Elmir (1990) found that the higher the skew angle, the higher the maximum forces that are induced in the cross-frame members. The maximum cross-frame force recorded for SR 1 over US 13, the 65 degree skew bridge, is 3.6 ksi which is significantly higher than the maximum cross-frame force recorded for SR 299 over SR 1 of 1.5 ksi.

Thus, the field results for both girders and cross-frames yielded logical results. In Chapter 5, these values will be more thoroughly assessed relative to computational predictions and the enhanced refinement afforded by FEA will be used to more thoroughly analyze the bridge behaviors suggested by this data.

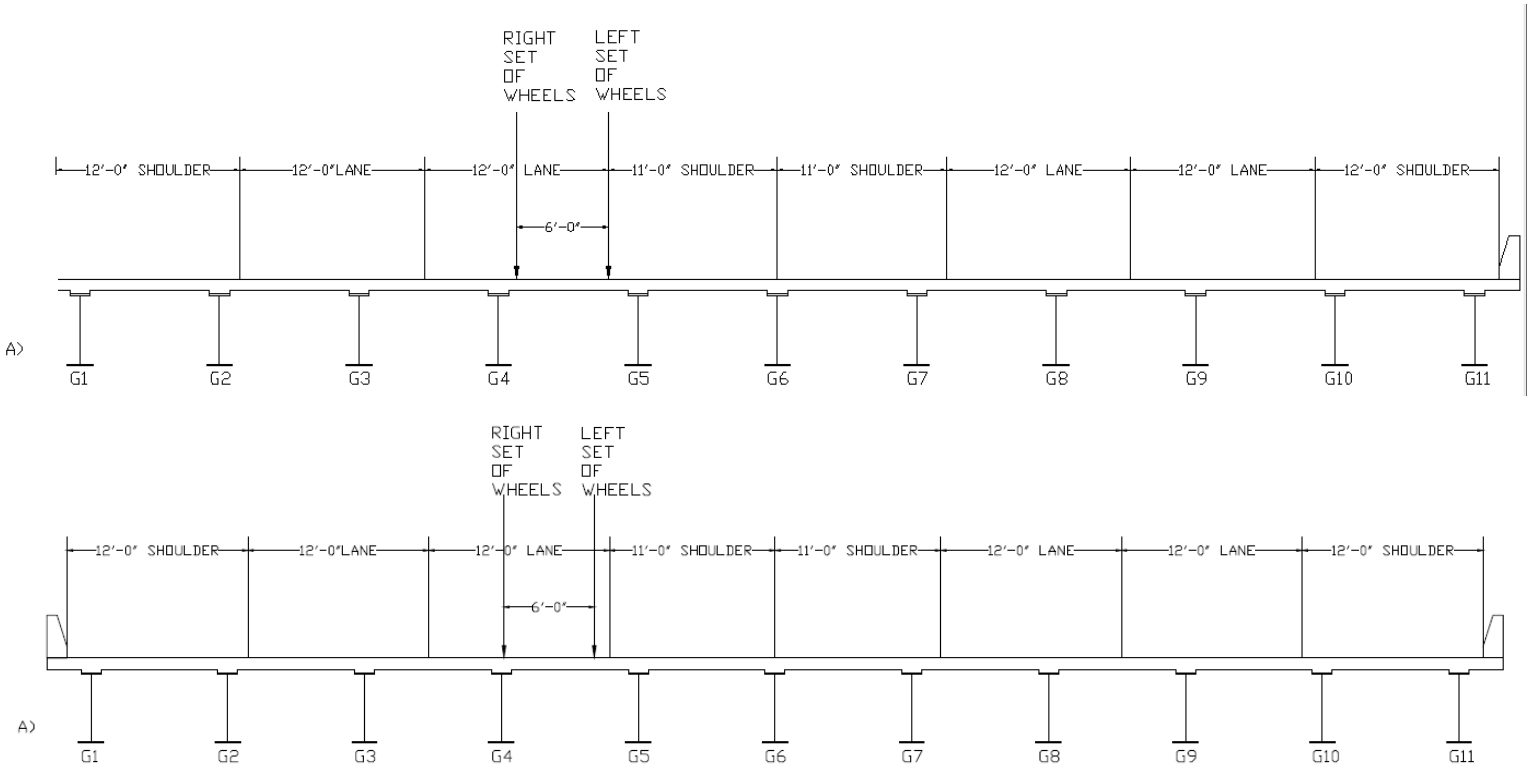

Figure 4.12 West bound Truck Passes (Pass 1) for SR 299 Over SR 1: A) Day 1 B) Day 2

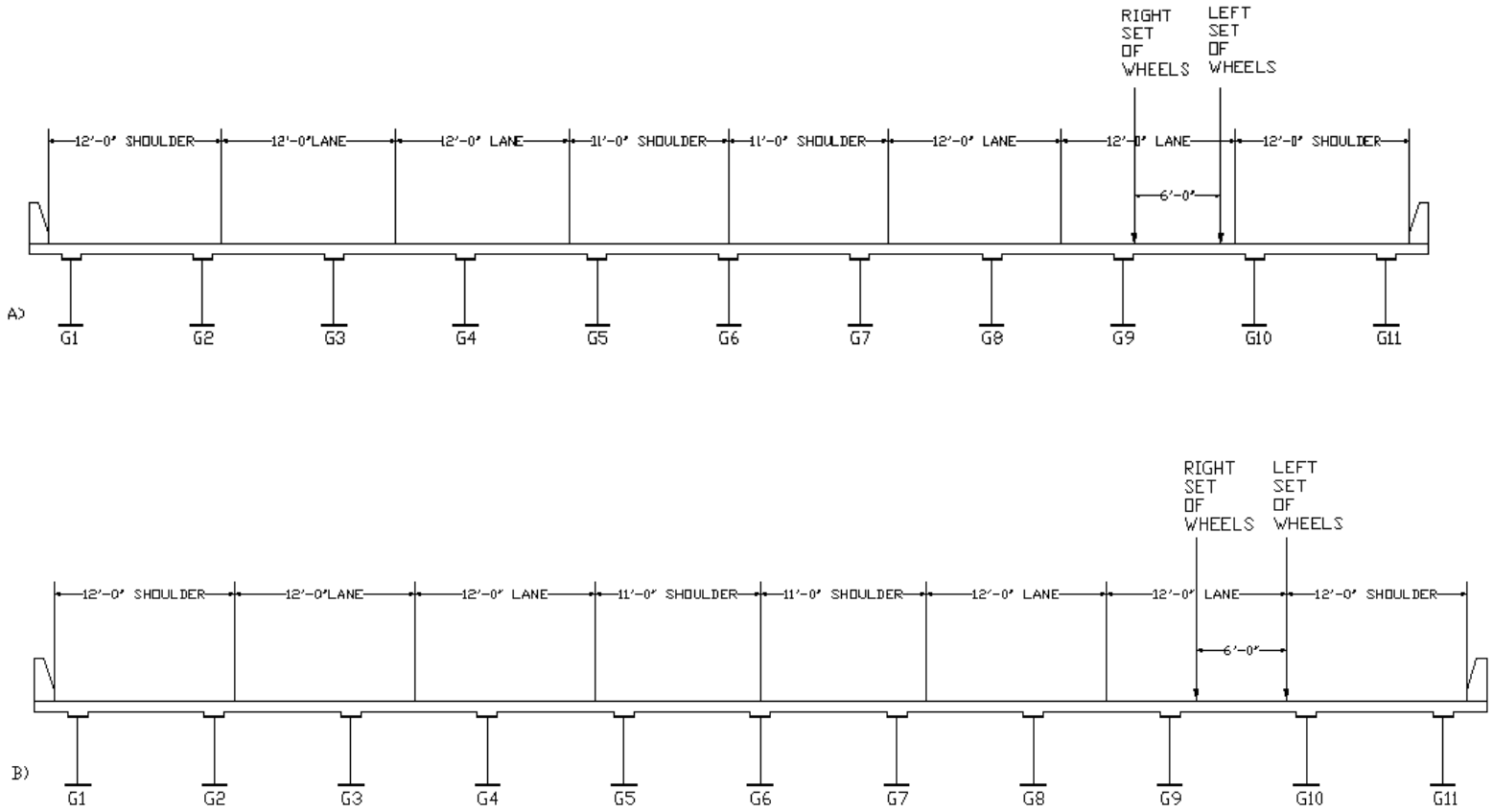

Figure 4.13 Eastbound Truck Passes (Pass 2) for SR 299 Over SR 1: A) Day 1, B) Day 2

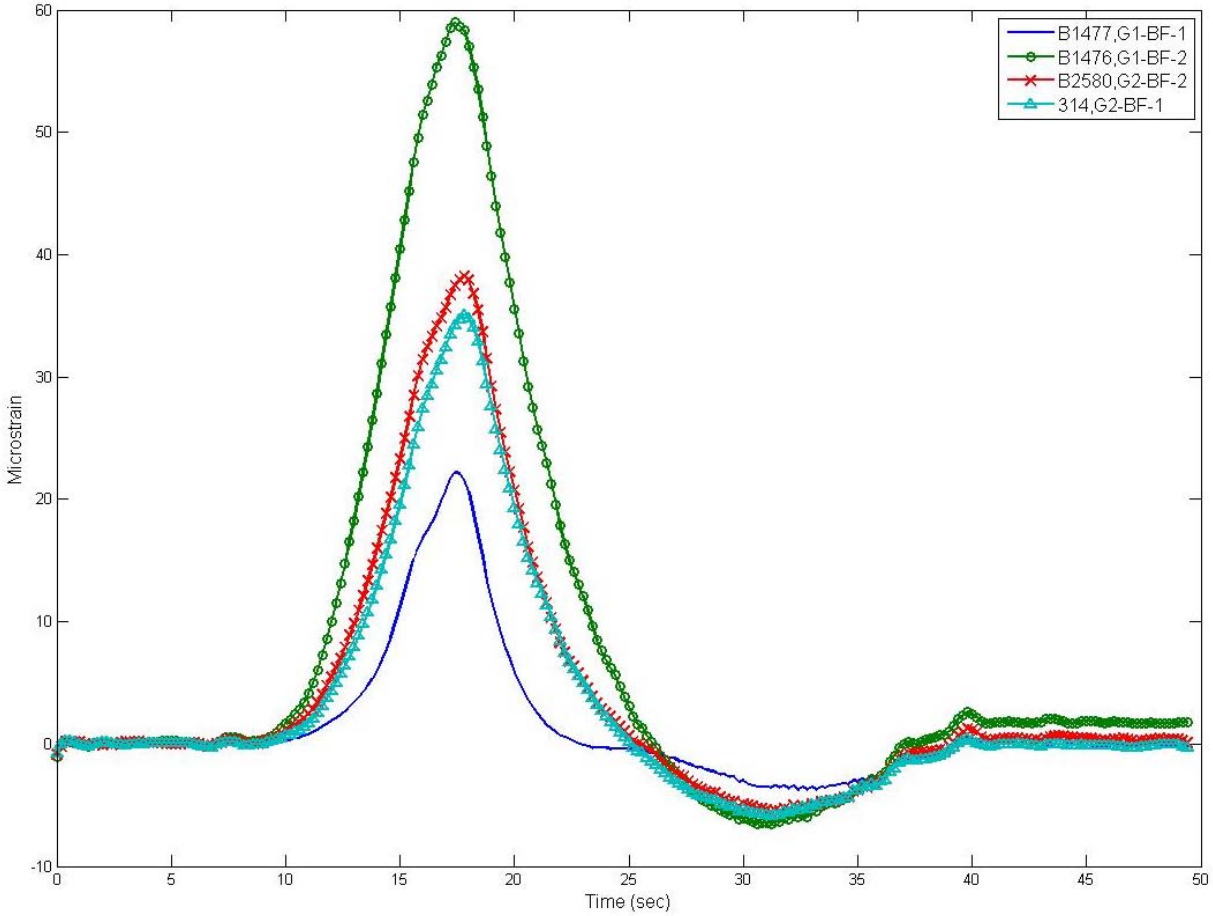

Figure 4.14 Time vs. Strain, SR 299 over SR 1, Day 1

Table 4.4 SR 1 Over US 13 Max Values, Girder Locations

			Pass 1			Pass 2			Pass 3		
Gauge Location	Gauge Number	Day	ε_{MAX}	σ_{MAX} (psi)	$\sigma_{MAX\text{-}AVG}$ (psi)	ε_{MAX}	σ_{MAX} (psi)	$\sigma_{MAX\text{-}AVG}$ (psi)	ε_{MAX}	σ_{MAX} (psi)	$\sigma_{MAX\text{-}AVG}$ (psi)
G1-W-1	337	2	-18.40	-533	314	11.79	342	500	11.25	326	403
G1-W-2	299	2	40.05	1161		22.67	658		16.56	480	
G1-BF-1	2171	2	37.02	1073	1267	34.35	996	999	31.27	907	835
G1-BF-2	317	2	50.37	1461		34.52	1001		26.30	763	
G2-W-1	2171	1	12.48	362	322	10.8	313	313	-4.76	-138	-138
G2-W-2	B1477	2	-7.69	-223	-223	-3.87	-112	-112	-4.60	-133	-133
G2-BF-1	293	1	-22.33	-567	7	-15.48	-449	-385	-11.37	-330	-296
G2-BF-2	348	1	17.29	581		-11.07	-321		-9.02	-262	
G3-W-1	355	1	15.82	459	27	9.51	276	217	6.08	176	161
G3-W-2	339	1	-13.96	-405		5.44	158		5.01	145	
G3-BF-1	292	1	50.29	1458	1307	42.88	1244	1095	34.68	1006	906
G3-BF-2	3317	1	39.83	1155		35.59	945		27.8	806	

*Note: G2-W-2 only recorded on Day 2

Table 4.5 SR 1 Over US 13 Max Values, Cross-frames 12-3, 12-4, & 14-3 Passes 1 & 2

		Pass 1			Pass 2		
Gauge Location	Gauge Number	ε_{MAX}	σ_{MAX} (psi)	$\sigma_{MAX-AVG}$ (psi)	ε_{MAX}	σ_{MAX} (psi)	$\sigma_{MAX-AVG}$ (psi)
12-3-B	2581	36.62	1062	621	71.8	2082	1199
12-3-B	2172	6.20	180		10.88	316	
12-3-D	1475	15.81	458	504	42.26	1226	1018
12-3-D	1478	18.92	549		27.9	809	
12-3-H	2579	22.69	658	658	-23.39	-678	-678
12-3-I	3318	47.98	1392	747	41.08	1191	718
12-3-I	3315	3.48	101		8.46	245	
12-3-J	294	45.36	1315	688	38.64	1121	348
12-3-J	318	2.1	61		-14.69	-426	
12-4-A	314	-85.08	-2467	-1489	-90.59	-2627	-1570
12-4-A	2580	-17.58	-510		-17.69	-513	
12-4-C	1476	-100.55	-2916	-1597	-91.4	-2651	-1646
12-4-C	1477	-9.69	-281		-22.11	-641	
12-4-G	3319	98.28	2850	2850	66.51	1929	1929
12-4-I	2173	7.82	227	319	-26.85	-779	-212
12-4-I	356	14.13	410		12.25	355	
12-4-J	2578	8.44	245	-357	-21.44	-622	-752
12-4-J	306	-33.05	-958		-30.40	-882	
14-3-B	3314	44.79	1299	1356	108.99	3161	3161
14-3-F	337	31.65	918	973	-27.96	-811	108
14-3-F	299	35.4	1027		35.43	1027	
14-3-H	344	49.04	1422	1123	6.63	192	484
14-3-H	317	28.38	823		26.73	775	
14-3-I	295	84.57	2453	1302	99.87	2896	1629
14-3-I	338	5.20	151		12.48	362	
14-3-J	346	85.88	2491	1426	103.86	3012	1453
14-3-J	3316	12.42	360		-3.64	-106	

Table 4.6 SR 1 Over US 13 Max Values, Cross-frames 12-3, 12-4, & 14- 3, Pass 3

		Pass 3		
Gauge Location	Gauge Number	ε_{MAX}	σ_{MAX} (psi)	$\sigma_{MAX\text{-}AVG}$ (psi)
12-3-B	2581	79.22	2297	1335
12-3-B	2172	12.86	373	
12-3-D	1475	52.34	1518	1143
12-3-D	1478	26.48	768	
12-3-H	2579	-45.02	-1305	-1246
12-3-I	3318	26.93	781	549
12-3-I	3315	10.92	317	
12-3-J	294	25.03	726	65
12-3-J	318	-20.58	-597	
12-4-A	314	-89.36	-2591	-1562
12-4-A	2580	-18.34	-532	
12-4-C	1476	-80.24	-2327	-1538
12-4-C	1477	-25.8	-748	
12-4-G	3319	39.21	1137	1137
12-4-I	2173	-38.54	-1118	-413
12-4-I	356	10.08	292	
12-4-J	2578	-33.5	-972	-880
12-4-J	306	-27.13	-787	
14-3-B	3314	123.73	3588	3588
14-3-F	337	-56.46	-1637	-398
14-3-F	299	29.04	842	
14-3-H	344	-27.26	-790	-107
14-3-H	317	19.87	576	
14-3-I	295	90.84	2634	1527
14-3-I	338	14.47	420	
14-3-J	346	95.21	2761	1229
14-3-J	3316	-10.46	-303	

Table 4.7 SR 1 Over US 13 Max Values, Cross-frames 4-4 & 11-3, Passes 1 & 2

		Pass 1			Pass 2		
Gauge Location	Gauge Number	ε_{MAX}	σ_{MAX} (psi)	$\sigma_{MAX\text{-}AVG}$ (psi)	ε_{MAX}	σ_{MAX} (psi)	$\sigma_{MAX\text{-}AVG}$ (psi)
4-4-A	3318	-102.72	-2979	-1656	-86.38	-2505	-1397
4-4-A	3315	-11.44	-332		-9.93	-288	
4-4-C	1475	-108.02	-3133	-1662	-80.21	-2326	-1340
4-4-C	294	-6.56	-190		-12.16	-353	
4-4-E	2579	113.80	3300	2287	76.66	2223	1487
4-4-E	2581	43.95	1275		25.88	751	
4-4-G	2172	145.45	4218	1972	85.83	2489	1184
4-4-G	1478	-9.46	-274		-4.17	-121	
4-4-I	355	40.07	1162	938	8.15	236	339
4-4-I	3317	24.63	714		15.20	441	
4-4-J	339	36.28	1052	43	9.07	263	-284
4-4-J	3316	-33.32	-966		-28.63	-830	
11-3-B	3319	46.74	1409	1409	55.95	1623	1710
11-3-F	292	-53.10	-1540	-1540	-50.86	-1475	-1408
11-3-H	2173	-47.73	-1384	-784	-46.04	-1335	-551
11-3-H	2170	-6.36	-184		8.05	233	
11-3-I	2578	14.44	419	311	13.12	380	286
11-3-I	306	7.01	203		6.62	192	
11-3-J	356	16.48	478	19	15.44	448	14
11-3-J	533	-15.18	-440		-14.48	-420	

Table 4.8 SR 1 Over US 13 Max Values, Cross-frames 4-4 & 11-3, Pass 3

		Pass 3		
Gauge Location	Gauge Number	ε_{MAX}	σ_{MAX} (psi)	$\sigma_{MAX\text{-}AVG}$ (psi)
4-4-A	3318	-71.64	-2077	-1174
4-4-A	3315	-9.36	-271	
4-4-C	1475	-63.08	-1829	-1153
4-4-C	294	-13.22	-383	
4-4-E	2579	59.08	1713	1126
4-4-E	2581	18.55	538	
4-4-G	2172	60.25	1747	894
4-4-G	1478	1.42	41	
4-4-I	355	-12.23	-355	-18
4-4-I	3317	11.00	319	
4-4-J	339	-9.07	-263	-509
4-4-J	3316	-26.03	-755	
11-3-B	3319	67.14	1947	1947
11-3-F	292	-85.49	-2479	-2479
11-3-H	2173	-80.75	-2342	-1368
11-3-H	2170	-13.57	-394	
11-3-I	2578	16.18	469	395
11-3-I	306	11.04	320	
11-3-J	356	16.18	469	-87
11-3-J	533	-22.18	-643	

Table 4.9 SR 299 Over SR 1 Max Values, Girder Locations

			Pass 1			Pass 2		
Gauge Location	Gauge Number	Day	ε_{MAX}	σ_{MAX} (psi)	$\sigma_{MAX-AVG}$ (psi)	ε_{MAX}	σ_{MAX} (psi)	$\sigma_{MAX-AVG}$ (psi)
G1-W-1	294	2	28.53	828	505	4.34	126	79
G1-W-2	317	2	6.25	181		1.14	33	
G1-BF-1	3318	2	37.68	1093	1133	7.09	205	180
G1-BF-2	3314	2	40.41	1172		5.33	155	
G1-BF-1	1477	1	23.34	677	1213	8.92	259	185
G1-BF-2	1476	1	60.29	1748		3.80	110	
G2-BF-1	314	1	35.31	1024	1073	4.18	121	164
G2-BF-2	2580	1	38.66	1121		7.11	206	
G2-W-1	348	2	34.84	1010	297	5.79	168	52
G2-W-2	299	2	-14.38	-417		-2.18	-63	
G2-BF-1	3319	2	60.27	1748	1233	-5.80	-168	59
G2-BF-2	337	2	24.76	718		9.89	287	
G3-W-1	292	1	-4.76	-138	-153	12.72	369	453
G3-W-2	344	1	-5.81	-168		18.54	538	
G3-BF-1	3317	1	2.75	80	-73	25.68	745	810
G3-BF-2	3316	1	-7.78	-225		30.20	876	

Table 4.10 SR 299 Over SR 1 Max Values, Cross-frames 14-8, 14-9, & 14-10

		Pass 1			Pass 2		
Gauge Location	Gauge Number	ε_{MAX}	σ_{MAX} (psi)	$\sigma_{MAX\text{-}AVG}$ (psi)	ε_{MAX}	σ_{MAX} (psi)	$\sigma_{MAX\text{-}AVG}$ (psi)
14-8-B	2170	-8.38	-243	-134	-31.51	-914	-475
14-8-B	2578	-0.86	-25		-1.19	-35	
14-8-D	2171	-7.44	-216	-148	-24.26	-703	-368
14-8-D	2173	-2.72	-79		-7.61	-32	
14-8-G	318	-13.40	-388	-222	42.31	1227	701
14-8-G	339	-1.89	-55		6.05	175	
14-8-H	293	-14.14	-410	-175	49.61	1439	572
14-8-H	355	2.08	60		-10.19	-296	
14-9-B	3318	-7.49	-217	-102	24.05	697	320
14-9-B	3314	0.49	14		-1.95	-57	
14-9-D	3319	-6.72	-195	-134	21.94	636	470
14-9-D	3315	-2.52	-73		10.48	304	
14-9-E	346	-16.63	-482	-246	63.41	1839	NA
14-9-E (NB)	535	-0.32	-9		NA	NA	
14-9-G	2581	-7.29	-212	-133	32.63	946	587
14-9-G	2579	-1.86	-54		7.81	227	
14-9-H	1478	-5.97	-173	-79	29.18	846	357
14-9-H	2172	0.55	16		-4.55	-132	
14-10-A	348	5.58	162	92	-32.07	-930	-507
14-10-A	337	0.75	22		-2.86	-83	
14-10-C	317	5.01	145	100	-26.68	-774	-576
14-10-C	298	1.86	54		-13.03	-378	
14-10-E	306	-9.82	-285	-111	41.32	1198	463
14-10-E	533	2.20	64		-9.41	-273	
14-10-F	294	-8.20	-238	-142	36.60	1061	598
14-10-F	299	-1.71	-50		4.65	135	

Table 4.11 SR 299 Over SR 1 Max Values, Cross-frames 12-4, 12-5, & 8-4

		Pass 1			Pass 2		
Gauge Location	Gauge Number	ε_{MAX}	σ_{MAX} (psi)	$\sigma_{MAX\text{-}AVG}$ (psi)	ε_{MAX}	σ_{MAX} (psi)	$\sigma_{MAX\text{-}AVG}$ (psi)
12-4-B	2170	53.78	1560	801	1.76	51	797
12-4-B	2578	1.46	42		-0.98	-28	
12-4-D	2171	49.98	1450	994	1.33	39	981
12-4-D	2173	18.56	538		-1.01	-29	
12-4-G	314	45.50	1320	783	-9.67	-280	793
12-4-G	2580	8.46	246		-2.28	-66	
12-4-H	1476	47.73	1384	654	-10.78	-313	649
12-4-H	1477	-2.66	-77		1.19	35	
12-5-A	295	-47.09	-1366	-656	-3.95	-115	-664
12-5-A	338	1.89	55		0.63	18	
12-5-C	346	-38.75	-1124	-761	-3.74	-109	-743
12-5-C	344	-13.70	-397		-1.14	-33	
12-5-E	292	52.02	1509	560	-13.87	-402	560
12-5-E	3315	-13.43	-389		1.99	58	
12-5-F	3317	42.45	1231	691	-13.62	-395	691
12-5-F	3316	5.21	151		1.04	30	
8-4-B	1478	-10.47	-304	-186	-11.89	-345	-113
8-4-B	2172	-2.32	-67		-0.78	-23	
8-4-D	2579	-7.32	-212	24	-7.81	-227	24
8-4-D	2581	9.00	261		9.00	261	
8-4-G	318	5.30	154	110	7.06	205	110
8-4-G	293	2.29	66		2.86	83	
8-4-H	339	7.26	210	154	9.68	281	154
8-4-H	355	3.40	98		2.04	59	

Chapter 5

FEA VALIDATION AND SIMULATION OF FIELD TESTING

5.1 Introduction

One purpose of this chapter is to document the validation of the FEM created for each bridge from the field tests. In order to do this, the chapter begins by outlining the metrics used when post-processing the FEM data to compare with the field test results. This is discussed in Section 5.2. The greater resolution of the FEM also allows the field results to be further explained. Thus, the validation and the overall bridge behavior elucidated by this data from the girders and cross-frames forces are discussed in Section 5.3. Section 5.4 summarizes the results of the validation procedure.

5.2 FEM Data Extraction

This section is divided into three primary sections. The first sections details the procedure used to acquire bottom flange data from the FEMs. The second section details the procedure in acquiring web data from FEMs and the third sections details the procedure in acquiring cross-frame data from the FEMs.

5.2.1 Bottom Flange Data Extraction

As explained in Chapter 3, each girder's bottom flange is modeled with four-node shell elements. A total of 6 shell elements that correspond to the locations of the bottom flange strain gauges (G1-BF-1, G1-BF-2, G2-BF-1, G2-BF-2, G3-BF-1 and G3-BF-2) were identified and used for data extraction in the FEM. These are called the bottom flange field elements in the discussion that follows. The output from the shell elements is provided at multiple section points through the thickness of the shell, where the bottom flange section point of interest in order to compare to the physical location

instrumented in the field work is the section point corresponding to the bottom surface of the bottom flange. To insure this section point is consistently used, each shell element is assigned an orientation vector where the n-vector shown in Figure 5.1 points in the upward direction. The material orientation determines the numbering of the section points so that when oriented as shown in Figure 5.1, the section point at element's bottom face is labeled as Section Point 1. In-plane stresses are then extracted at the section points of the elements of interest. As previously discussed in Chapter 4, gauges are positioned aligned with the length of the bottom flange, which corresponds to the S22 stresses in the FEA

Lastly, the S22 data at the section points of interest were compared from the multiple load cases described in Chapter 3 (136 load cases for US-13 and 200 load cases for SR-299). The maximum tensile (positive) and maximum compressive (negative) stress from each data set is identified, documented, and then compared to the corresponding field measurements.

5.2.2 **Web Data Extraction**

Similar to the process used for the flange elements, to extract FEA web data, first the three shell elements that match the locations of the web strain gauges (G1-W, G2-W and G3-W) were identified. These are called the web field elements in the discussion that follows. In contrast to the geometry of the flange, a single element represents the vertical and longitudinal position of two web gauges (e.g.,G1-W-1 and G1-W-2), such that half as many web elements are involved in data extraction as flange elements for the same number of gauges. Instead, data from two section points are used to represent the different through-thickness positions of the web field gauges.

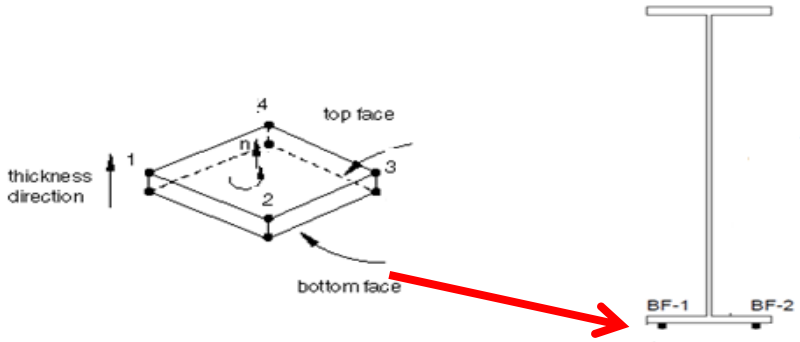

Figure 5.1 Shell Element and Material Orientation in Abaqus v.6.11

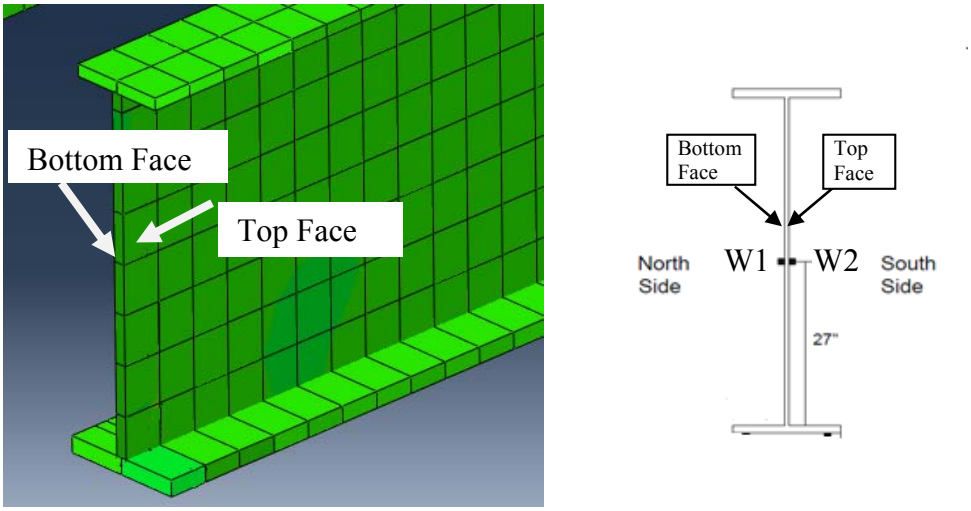

Figure 5.2 Locations of Web Elements in Abaqus and Corresponding Field Web Gauge Locations

This (and the gauge positions described in Chapter 4) dictates that FEA data for Section Point 1 corresponds to field data from W1 gauges while data extracted from Section Point 5 corresponds to field measurement data from W2 gauges.

The local 2-axis of the web elements' orientation is the same as the bottom flange shell orientation, meaning S22 stresses are again the stresses of interest coinciding with the longitudinal stresses obtained in the field testing. Therefore, the FEA S22 stresses are extracted. The same process as described above for the flanges is also used to compare the data from various load cases. Specifically, the maximum tensile and compressive stresses for Section Points 1 and 5 from each of the three web

elements of interest in each model is identified, documented and then compared to the corresponding web field data.

5.2.3 **Neutral Axis Calculation**

The location of the neutral axis is an additional metric related to girder stresses that was used to evaluate the accuracy of the FEA. To determine the neutral axis in the FEA, the load case producing maximum tensile stresses in the more heavily-stressed bottom flange field elements was identified from the data set. Then stresses were extracted at the same load case for the corresponding bottom flange elements (i.e., the opposite gauge of each BF1-BF2 pair) and the web field elements, such that the stresses are known at each of the instrumented points in the cross-section at a common level of load. To determine the corresponding field data, a similar process was used where the load case (as expressed by time stamp associated with each reading) producing maximum tensile strains in the gauges at each cross-section was identified (which was always one of the two bottom flange strain gauges). Then strains at the corresponding time stamp for the other gauges in the same cross-section were then compiled.

To remove lateral bending effects and reduce experimental error in the field test and FEA results, the two bottom flange stresses were averaged and the two web element stresses were averaged. Knowing the bottom flange and web stresses and the corresponding spatial positions, the location of the neutral axis is extrapolated using Equation 5-1.

$$NA = \frac{BF_{stress} - W_{stress}}{BF_{stress} \cdot Y_{web}} \qquad \textit{Equation 5-1}$$

where:

BF_{stress} is averaged bottom flange stress,

W_{stress} is averaged web stress, and

Y_{web} is distance from the location where the web stress is measured to the bottom of the bottom flange. These neutral axis calculations are compared to one another as well as theoretical neutral axis positions later in this chapter.

5.2.4 **Cross-frame Data Extraction**

Figure 5.3 shows a typical view of the instrumentation of a cross-frame cross-section (in this case for US-13), as previously described in Chapter 4. The five beam elements per instrumented cross-frame in the US -13 model (corresponding to the gauge locations shown in the left side of Figure 5.3) and four beam elements per instrumented cross-frame in the SR-299 model corresponding to the field cross-frame gauge locations were identified. These are called the cross-frame field elements in the discussion that follows. Additionally, the right side of Figure 5.3 shows the section points, SP1 and SP2, on the beam element cross-section that were manually defined in order to correspond to the locations of the strain gauges on the cross-frames members. A third section point (SP3) that is shown in Figure 5.3 is the location of the centroid of the beam element. As previously discussed in Chapter 3, the cross-frames are modeled as one-dimensional beam elements. As such, these elements can only bend about their longitudinal axes, and thus only one planar stress component, about the longitudinal axis, exists. This stress corresponds to the direction in which strain was recorded in the field testing and is labeled as S11.

The data resulting from 136 load cases in the US-13 model and 200 load cases in the SR-299 model were extracted at each section point of interest in each beam

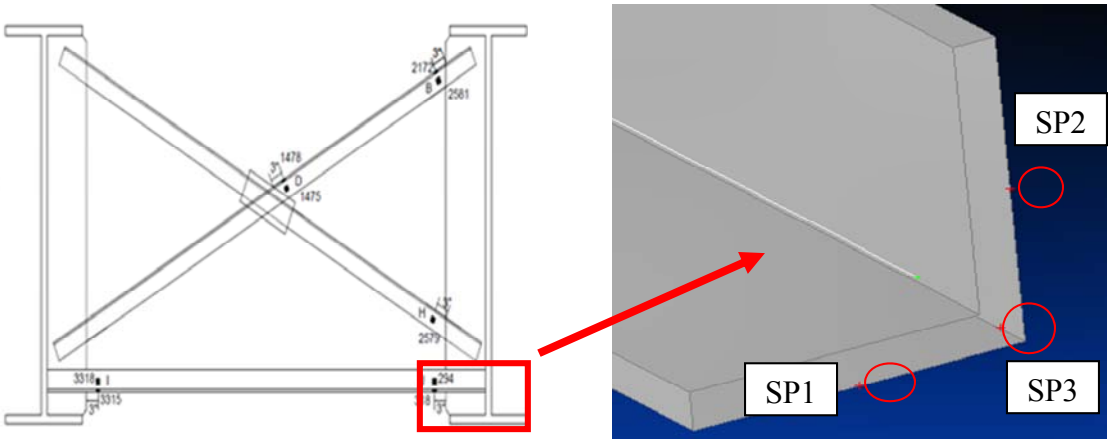

Figure 5.3 Typical Gauge Instrumentation Schematics for Cross-frame Elements and Corresponding SP1 and SP2 Section Points on Beam Elements

element of interest. The maximum tensile and compressive stress for each of these is identified, documented, and then compared to the corresponding field data. Originally, S11 stresses from SP1 and SP2 were extracted for each cross-frame field element and then compared to the stresses from the corresponding gauge locations in the field testing. Figure 5.4 shows an example of this, where the time stamp data from the field test and the load case data from the FEA (which was described in Chapter 3) are merged together by converting the time stamp data in the field test to approximate load cases based on when the data indicates the truck moved on and off the bridge and assuming the truck is traveling at a constant speed. Figure 5.4 shows that these results do not compare well, with minimal stresses being output at the manually-defined section points. In contrast, Figure 5.4 also shows that when plots from SP3 data sets were compared with plots of data set from the strain gauge on the concentric (bolted) leg of the cross-frame member, more realistic data is obtained. Thus, it was concluded that the manually-defined section points did not function as intended and thus the data analysis focused on comparing SP3 data with concentric leg field data.

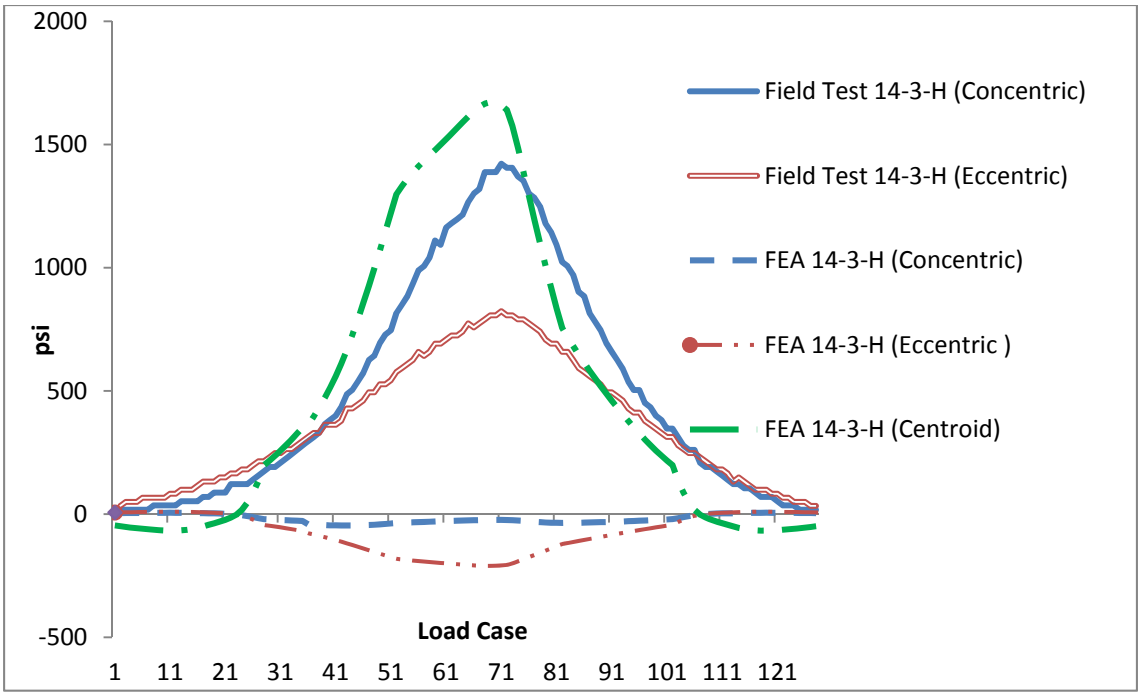

Figure 5.4 Stress Data from Field Measurements and FEA for Cross-frame 14-3-H (US-13)

5.3 Comparison of Field Measurements and FEA Results

This section presents and analyzes the data from the two field tests and the corresponding FEA of these tests. A discussion of the FEA data analysis procedures was previously presented in Section 5.2. All of the field data was processed in MATLAB by using the "smooth" function to take a 5-point moving average of the data This eliminated a large amount of noise in the data. The smoothed strain data was converted to stress by multiplying by the standard value assumed for modulus of elasticity of the steel (29,000 ksi) in order to express the data in quantities having more practical significance to most bridge engineers. The results of this process for each of the two bridges are presented in the following two sub-sections.

5.3.1 **Comparison for US-13**

This section is divided in three primary components. The first (Section 5.3.1.1) presents bottom flange field test measurements and bottom flange FEM data for US-13. This section also discusses lateral bending of the bottom flange. Section 5.3.1.2 presents web data. And lastly, Section 5.3.1.3 presents cross-frame data.

5.3.1.1 **Bottom Flange Results for US-13**

The bottom flange data allows for validation that the primary flexural response of the girders and load distribution characteristics of the bridge are successfully simulated. Table 5.1 shows the data comparison for the maximum tension and compression stresses from the field tests and FEA models for the three bottom girder gauge locations during the three vehicle passes. The values reported in Table 5.1 are maximum concurrent stress values, meaning that the maximum tensile and compressive stresses for any gauge in each gauge pair are identified and recorded and then the concurrent stress value occurring at the same time in the opposite gauge of the gauge pair is recorded. The same procedure is repeated for the FEA results, where concurrent stresses occurring at common loading positions are recorded for each gauge pair. The percent errors reported here are calculated by subtracting the FEA result from the field result and dividing this difference by the field result. Figures 5.5 and 5.6 present alternate graphical formats of this tension and compression stress data, respectively.

The peak bottom flanges stresses are tensile stresses. The top half of Table 5.1 and Figure 5.5 shows that these stresses for the field testing and FEA are generally in good agreement with one another. Specifically, the average percent differences between the bottom flange stresses for all gauge locations at each pass (the data line labeled “Average”, “Tension” in Table 5.1) varies between 2 and 13% for the tension results,

which is deemed a satisfactory result. The results for the two passes closest to the instrumented girder (Pass 1 and Pass 2) yield especially good results on average, with the average difference for these two passes being 8% or less. As the model results becomes more influenced by the transverse load distribution properties of the structure as the transverse distance between the load position and the gauge position increases, this is a logical result that these two passes provided the most favorable comparison. In terms of gauge location, it is observed that the best correlation is obtained at Locations G1 and G3. These are the two locations experiencing the greatest positive bending stress, while in contrast G2 is relatively close to the pier support.

A weaker correlation was expected and achieved when comparing the compressive stress results due to the fact that the concrete is in tension in this situation and the concrete deck was modeled as a linear elastic material with infinite tensile strength for modeling efficiency. These results are included to document the error induced by this simplification; but given the research emphasis on cross-frame stresses, which are observed as being maximized when the bottom flange is in tension, the high percent differences reported here do not affect the overall research objectives. The range of percent differences in this situation varies between 1 and 181%, although this high percent difference is associated with low stresses such that the difference in magnitude (162 psi) is not extreme. It is interesting to note that the passes and gauge locations producing the best and worst correlations in the compression data are exactly reversed from those corresponding to the tension data. Specifically, when evaluating the percent differences between each pass, the best correlation is obtained under Pass 3. The G2 location, which experiences the highest compressive stresses due to its location in proximity to the pier, has significantly better correlation that the remaining locations with the average G2 gauge pair results being less than 20% for all three passes.

The largest overall field test tensile stress (1475 psi) was recorded during Pass 1 at location G3-BF-1. The largest field test compressive stress (544 psi) was recorded at

G2-BF-1 during Pass 1. Pass 1 was designed to produce the highest bending stresses in the bottom flange of the instrumented girder at gauge location G3-BF and to produce the largest compressive stress over the pier, so this result confirms the generally expected theoretical behavior exists in this bridge. The largest FEA tensile stress (1263 psi) was obtained at the same gauge location as the field test (G3-BF-1), while largest FEA compressive stress (550 psi) was also obtained at the same gauge location as the field test (G2-BF-1). Both field test and FEA results at these maximum values correlate acceptably, with 1% difference for the compression stress results and 17% difference for the tension stress results. If the average maximum bottom flange tensile stresses are compared, this difference improves to only 7%. The average difference for maximum\ compression stresses is 16%. Based on collectively considering the results presented, it was concluded that the bottom flange FEM results validate that the model reproduces the girder response with sufficient accuracy.

The bottom flange results also provide information on the lateral bending response of this highly skewed bridge. The general response shown in the data for all gauge and passes, when the bottom flange is in tension or compression, and for both FEA and field results, is that the west side of the bottom flange (BF-1 locations) is experiencing higher stresses than the east side (BF-2 locations). Note this is in terms of absolute values of stress, where tensile stresses are assigned a positive sign and compressive stresses are assigned a negative sign. This indicates that the girder is experiencing lateral bending that causes the west side of the girder to experience tensile lateral bending stresses and the east side of the girder to experience compressive lateral bending stresses when positive moment is applied and the direction of the lateral bending stress to reverse when negative moment is applied. Figures 5.7 and 5.8 conceptually demonstrate how the vertical and lateral bending forces sum to produce the observed results, neglecting the influence of torsion. It is important to note that the gauges used in the field measurements are recording resultant longitudinal elongations

and contractions. This means if the girder is subject to additional longitudinal strain due to warping torsion, the gauge reading will reflect the resultant elongation of all three actions (vertical bending, lateral bending and warping). The discussion that follows neglects the potential for warping torsion consistent with typical bridge design practice and to avoid unnecessarily complicating the discussion.

It follows from the concept shown in Figures 5.7 and 5.8 that a system of equations can be written to solve for the two unknown values of peak lateral bending stress and vertical bending stress at each gauge pair using the two known gauge readings. Specifically, letting V_B be vertical bending stress, L_B be peak lateral bending stress, and T_1 and T_2 be the two total gauge readings at BF-1 and BF-2, respectively, then when the bottom flange is in tension:

$$V_B + L_B = T_1 \quad \text{(at BF-1 in tension)} \qquad \textit{Equation 5-2}$$

$$V_B - L_B = T_2 \quad \text{(at BF-2 in tension)} \qquad \textit{Equation 5-3}$$

and when the bottom flange is in compression:

$$-V_B - L_B = T_1 \qquad \textit{Equation 5-4}$$

$$-V_B + L_B = T_2. \qquad \textit{Equation 5-5}$$

Using these equations, the lateral and vertical bending stresses at each gauge pair, for each pass and force effect were calculated. Table 5.2 summarizes these results based on the field testing while Table 5.3 summarizes these results based on the FEA. In the field data, the maximum value of lateral bending stress (224 psi) was detected under tension at location G1 during Pass 1; the percentage of lateral stress relative to vertical stress was highest (38%) under compression during Pass 1, at location G3. Not only does this behavior increase girder stresses, such lateral bending would also theoretically increase forces in the cross-frame members, which are rigidly attached to the girders. This behavior is further explored in the Section 5.3.1.3.

Table 5.1 Maximum Concurrent Girder Stresses (psi), US-13

		Pass 1			Pass 2			Pass 3		
Gauge Location	Action	Field Test (psi)	FEA (psi)	% error	Field Test (psi)	FEA (psi)	% error	Field Test (psi)	FEA (psi)	% error
G1-BF-1	Tension	1460	1199	18%	1001	1228	-23%	908	1125	-24%
G1-BF-2	Tension	1012	1033	-2%	995	980	2%	763	784	-3%
G1-AVG	Tension	1236	1116	10%	998	1104	-11%	835	954	-14%
G2-BF-1	Tension	591	492	17%	421	411	2%	251	333	-32%
G2-BF-2	Tension	503	471	6%	398	389	2%	240	292	-22%
G2-AVG	Tension	547	481	12%	409	400	2%	245	313	-27%
G3-BF-1	Tension	1475	1263	14%	1244	1054	15%	1006	863	14%
G3-BF-2	Tension	1231	1262	-2%	945	1045	-11%	776	857	-10%
G3-AVG	Tension	1353	1262	7%	1095	1050	4%	891	860	3%
Average	Tension			8%			-2%			-13%
G1-BF-1	Compression	-322	-360	-12%	-102	-234	-130%	-121	-163	-35%
G1-BF-2	Compression	-186	-286	-54%	-47	-89	-91%	-110	-8	93%
G1-AVG	Compression	-254	-323	-27%	-74	-161	-117%	-115	-85	26%
G2-BF-1	Compression	-545	-551	-1%	-449	-431	4%	-330	-365	-11%
G2-BF-2	Compression	-285	-437	-53%	-301	-364	-21%	-242	-284	-18%
G2-AVG	Compression	-415	-494	-19%	-375	-397	-6%	-286	-324	-14%
G3-BF-1	Compression	-201	-257	-28%	-215	-228	-6%	-168	-214	-28%
G3-BF-2	Compression	-91	-256	-181%	-180	-227	-26%	-151	-214	-41%
G3-AVG	Compression	-146	-257	-76%	-197	-227	-15%	-160	-214	-34%
Average	Compression			-55%			-45%			-6%

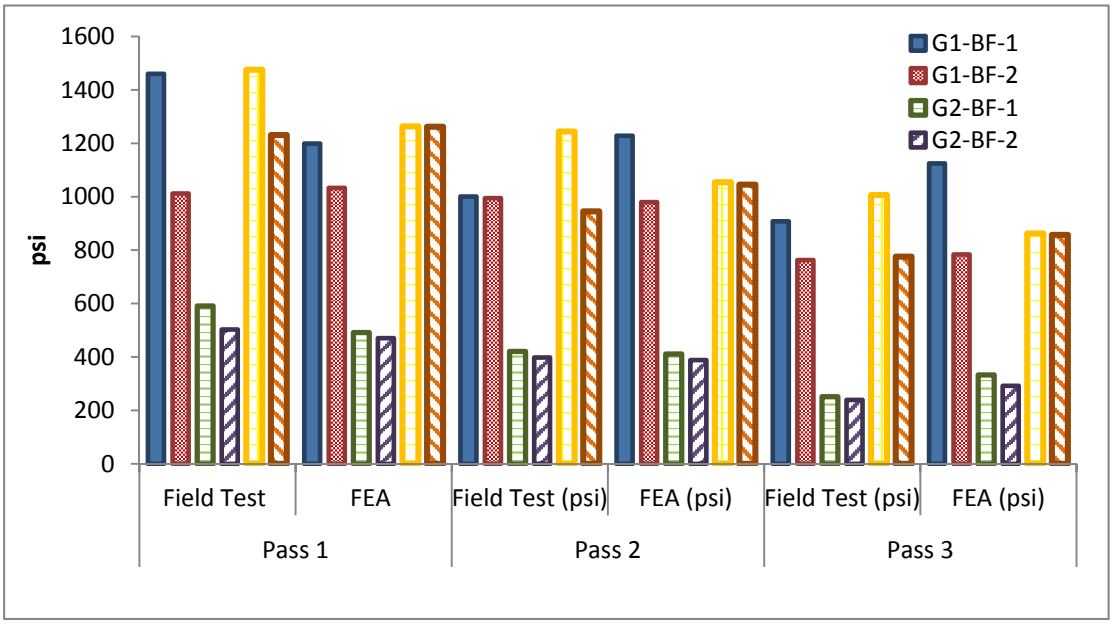

Figure 5.5 Maximum Concurrent Tension Stress Data: Field Measurements vs. FEA, US-13

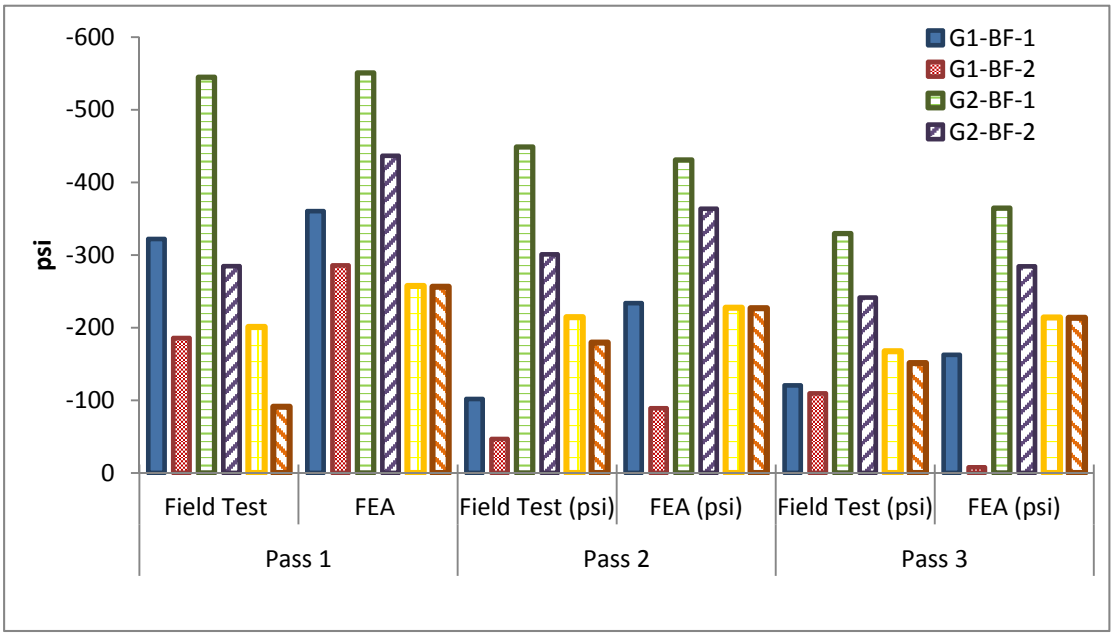

Figure 5.6 Maximum Concurrent Compression Stress Data: Field Measurements vs. FEA, US-13

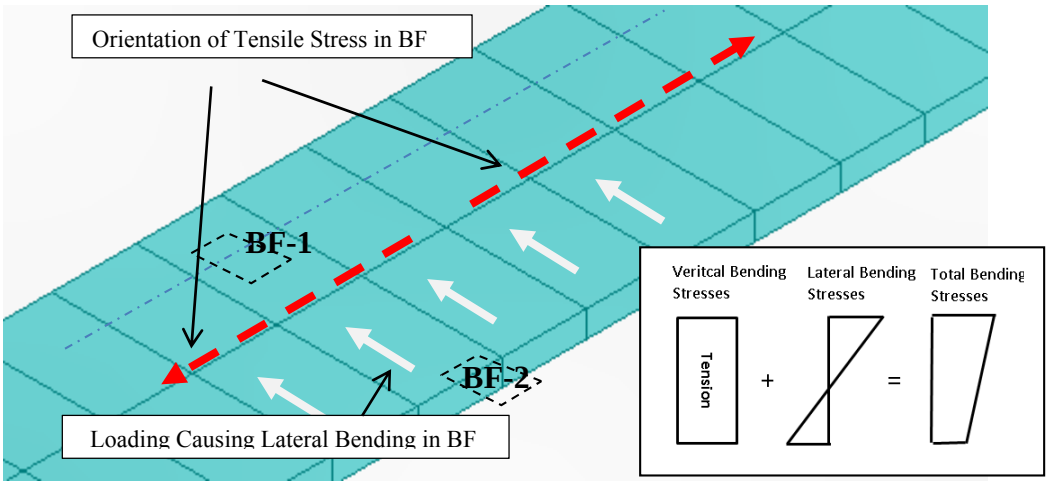

Figure 5.7 Effect of Biaxial Bending of the Bottom Flange When Vertical Bending Causes Tension

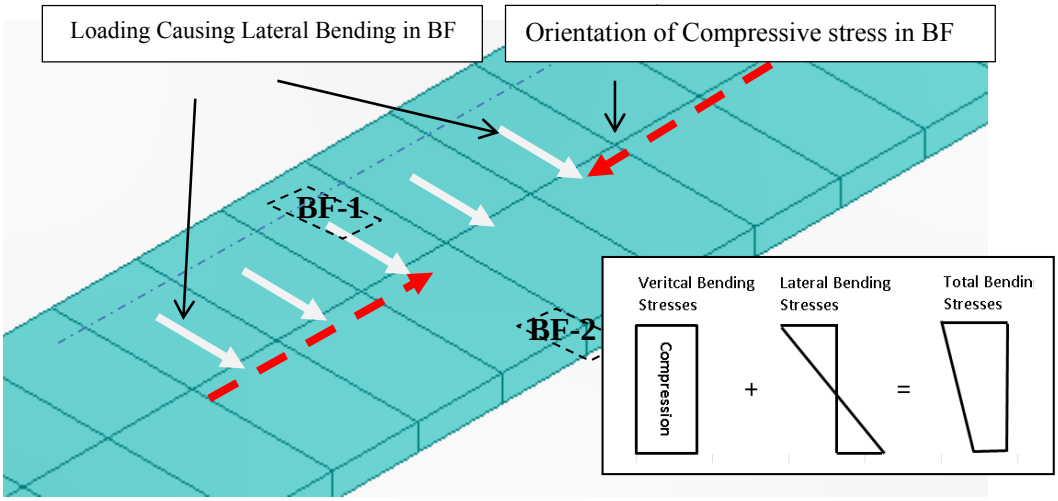

Figure 5.8 Effect of Biaxial Bending of the Bottom Flange When Vertical Bending Causes Compression

In comparing the data for the various cases shown in Table 5.2, one of the most obvious observations is that the lateral bending forces constitute a much more significant amount of the total stress when the bottom flange is in compression. A second observation is that the relative magnitude of lateral bending stress is generally highest during Pass 1 when the load is closest to the instrumented locations and decreases as the load moves farther away during Pass 2 and then Pass 3.

In comparing this data with the FEA results shown in Table 5.3, it is seen that the average for compression (20%) is both similar to the average for compression observed in the field results (21%) and once again significantly higher than the lateral bending effect in tension (5%), which is also similar to the average percentage of lateral bending in tension in the FEA results (8%). However, the values producing these similar averages are quite different. While the field results showed the percentage of lateral bending increasing with pass number, the opposite trend is seen in the FEA results. Perhaps most significantly, in several cases the FEA under-predicts the stress at one gauge of a gauge pair and over-predicts the stress at another. This occurs at Location G3 under all three load passes and in all cases the FEA underestimates the lateral stress gradient. In contrast, the opposite situation occurs in some situations, most significantly at Location G1 under Pass 3 causing compression, where the FEA over-estimates the lateral stress gradient.

5.3.1.2 **Web Results for US-13**

Table 5.4 shows the data comparison between the field and FEA results for the tensile and compressive stresses at the three web gauge locations during the three vehicle passes. The average value at each gauge pair is also reported for convenience in assessing vertical versus lateral bending affects. The values reported in Table 5.4 are maximum concurrent stress values, where the maximum tensile and compressive stresses for any gauge in each gauge pair are identified and recorded and then the concurrent stress value occurring at the same time in the opposite gauge of the gauge pair is recorded. The same procedure is repeated for the FEA results, where concurrent stresses occurring at common loading positions are recorded for each gauge pair. The percent errors reported here are calculated by subtracting the FEA result from the field result and dividing this difference by the field result.

The best overall correlation between the field and FEA results was achieved during Pass 3 at G3-W-2 gauge location during tension, where the error is only 2%. The best correlation for compressive stresses was achieved during Pass 3 at gauge location G2-W-2, where the error is an acceptable value of 12%. However, the percent errors are quite large in much of the remaining data where the data is even of opposite sign in five out of the 36 situations (2 gauges on each of 3 cross-sections under 3 load passes causing 2 force effects: 2 x 3 x 3 x 2 = 36). In all cases this is the result of web lateral bending effect at either G1-W-2 in compression or G2-W-2 in tension. In these situations the field data shows one side of the web in compression and other side in tension, but the FEA does not reproduce this effect.

An example of this is illustrated in Figure 5.9 for Pass 1 at Location G2-W. Here the maximum tensile stress (223 psi) was measured at Gauge G2-W-1; at the same time, the gauge on the other side of the web (Gauge G2-W-2) measured a compressive stress of -42 psi. In contrast, the FEA results for these same gauge locations, shown in Figure 5.10, show tensile stress of 215 psi and 168 psi, respectively. Thus, for this case, the peak tensile stress is well captured, but the field results generally indicate significantly more distortion of the cross-section than the FEA results.

It was discussed in Section 5.3.1.1 that the girders of this highly skewed bridge are subjected to both vertical and lateral bending. These effects as well as perhaps warping torsion of these non-compact webs seem to have an even greater influence on web stresses. Figure 5.11 explores this hypothesis by showing how the web stresses (shown on the left side of the figure) and flange stresses (shown on the right side of the figure) vary as the truck travels across the bridge in the field test. If the girder experiences only vertical bending, then the gauges on each side of a given cross-section for each gauge pair will report equal results. This type of response is observed in the data up to a point in the Figure 5.11 data, labeled the “separation point”, which

Table 5.2 Vertical and Lateral Bending Stresses (psi) For Bottom Flange, US-13, Field Results

		Pass 1				Pass 2				Pass 3					
Force Effect	Gauge Location	Field Test Stresses	Vertical Bending Component	Lateral Bending Component	% Lat./Ver.	Field Test Stresses	Vertical Bending Component	Lateral Bending Component	% Lat./Ver.	Field Test Stresses	Vertical Bending Component	Lateral Bending Component	% Lat./Ver.	Gauge Location Average	Force Effect Average
Tension	G1-BF-1	1460	1236	224	18%	1001	998	3	0.30%	908	835	73	9%	9%	8%
Tension	G1-BF-2	1012				995				763					
Tension	G2-BF-1	591	547	44	8%	421	409	12	3%	251	245	6	2%	4%	
Tension	G2-BF-2	503				398				240					
Tension	G3-BF-1	1475	1353	122	9%	1244	1095	149	14%	1006	891	115	13%	12%	
Tension	G3-BF-2	1231				945				776					
Compression	G1-BF-1	-322	-254	-68	27%	-102	-74	-28	37%	-121	-115	-6	5%	23%	21%
Compression	G1-BF-2	-186				-47				-110					
Compression	G2-BF-1	-545	-415	-130	31%	-449	-375	-74	20%	-330	-286	-44	15%	22%	
Compression	G2-BF-2	-285				-301				-242					
Compression	G3-BF-1	-201	-146	-55	38%	-215	-197	-18	9%	-168	-160	-8	5%	17%	
Compression	G3-BF-2	-91				-180				-151					
Pass Average					22%				14%				8%		

Table 5.3 Vertical and Lateral Bending Stresses (psi) For Bottom Flange, US-13, FEA Results

		Pass 1				Pass 2				Pass 3					
Force Effect	Gauge Location	Field Test Stresses	Vertical Bending Component	Lateral Bending Component	% Lat./Ver.	Field Test Stresses	Vertical Bending Component	Lateral Bending Component	% Lat./Ver.	Field Test Stresses	Vertical Bending Component	Lateral Bending Component	% Lat./Ver.	Gauge Location Average	Force Effect Average
Tension	G1-BF-1	1199	1116	83	7%	1228	1104	124	11%	1125	954	171	18%	12%	5%
Tension	G1-BF-2	1033				980				784					
Tension	G2-BF-1	492	481	10	2%	411	400	11	3%	333	313	20	7%	4%	
Tension	G2-BF-2	471				389				292					
Tension	G3-BF-1	1263	1262	1	0%	1054	1050	5	0%	863	860	3	0%	0%	
Tension	G3-BF-2	1262				1045				857					
Compression	G1-BF-1	-360	-323	-37	12%	-234	-161	-72	45%	-163	-85	-78	91%	49%	20%
Compression	G1-BF-2	-286				-89				-8					
Compression	G2-BF-1	-551	-494	-57	12%	-431	-397	-34	8%	-365	-324	-40	12%	11%	
Compression	G2-BF-2	-437				-364				-284					
Compression	G3-BF-1	-257	-257	-1	0%	-228	-227	0	0%	-214	-214	0	0%	0%	
Compression	G3-BF-2	-256				-227				-214					
Pass Average					5%				11%				21%		

Table 5.4 Maximum Concurrent Web Stresses (psi), US-13

		Pass 1			Pass 2			Pass 3		
Gauge Location	Action	Field data (psi)	FEA data (psi)	% error	Field data (psi)	FEA data (psi)	% error	Field data (psi)	FEA data (psi)	% error
G1-W-1	Tension	364	566	-56%	290	512	-77%	171	464	-172%
G1-W-2	Tension	1043	632	39%	658	557	15%	481	427	11%
G1-AVG	Tension	703	599	15%	474	534	-13%	326	446	-37%
G2-W-1	Tension	223	215	3%	212	108	49%	75	90	-20%
G2-W-2	Tension	-42	168	496%	57	182	-223%	-50	111	323%
G2-AVG	Tension	90	192	-112%	134	145	-8%	12	101	-707%
G3-W-1	Tension	459	610	-33%	276	488	-77%	512	427	17%
G3-W-2	Tension	405	565	-39%	193	479	-148%	350	343	2%
G3-AVG	Tension	432	587	-36%	234	484	-106%	431	385	11%
Average	Tension			68%			-77%			27%
G1-W-1	Compression	-533	-83	84%	-245	-59	76%	-243	-32	87%
G1-W-2	Compression	235	-119	151%	201	-35	117%	26	-14	154%
G1-AVG	Compression	-149	-101	32%	-22	-47	-117%	-109	-23	79%
G2-W-1	Compression	-223	-183	18%	-99	-153	-55%	-10	-140	-1278%
G2-W-2	Compression	-42	-182	-329%	-41	-160	-288%	-133	-149	-12%
G2-AVG	Compression	-133	-183	-38%	-70	-157	-123%	-72	-145	-101%
G3-W-1	Compression	-93	-108	-16%	-157	-98	38%	-138	-93	33%
G3-W-2	Compression	-68	-110	-60%	-105	-100	5%	-175	-95	46%
G3-AVG	Compression	-81	-109	-35%	-131	-99	25%	-157	-94	40%
Average	Compression			-25%			-18%			-162%

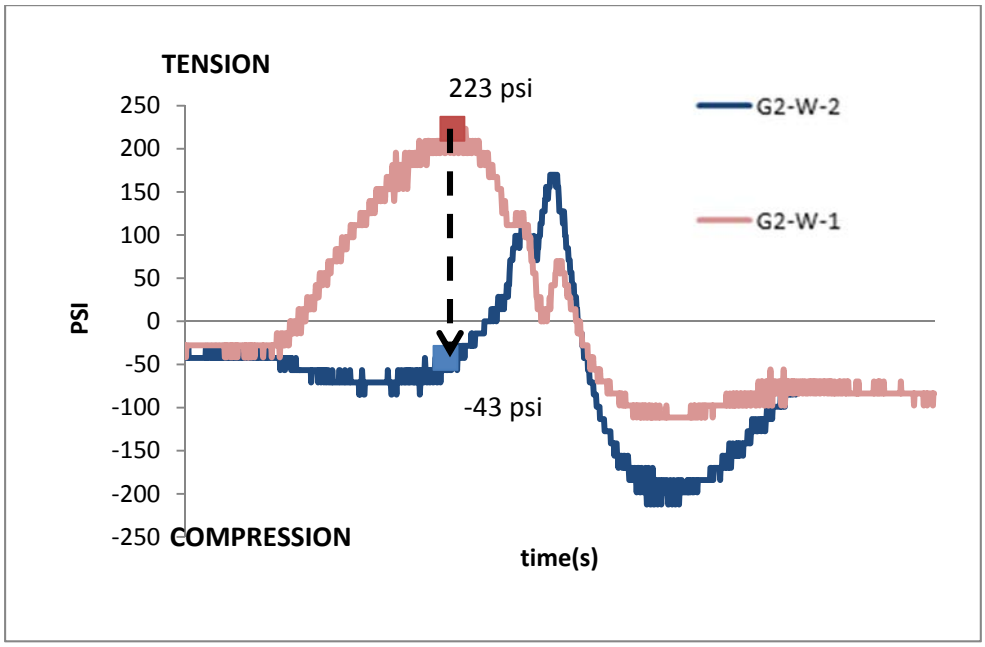

Figure 5.9 Web Field Test Results for Gauge Location G2-W During Pass 1 for US-13

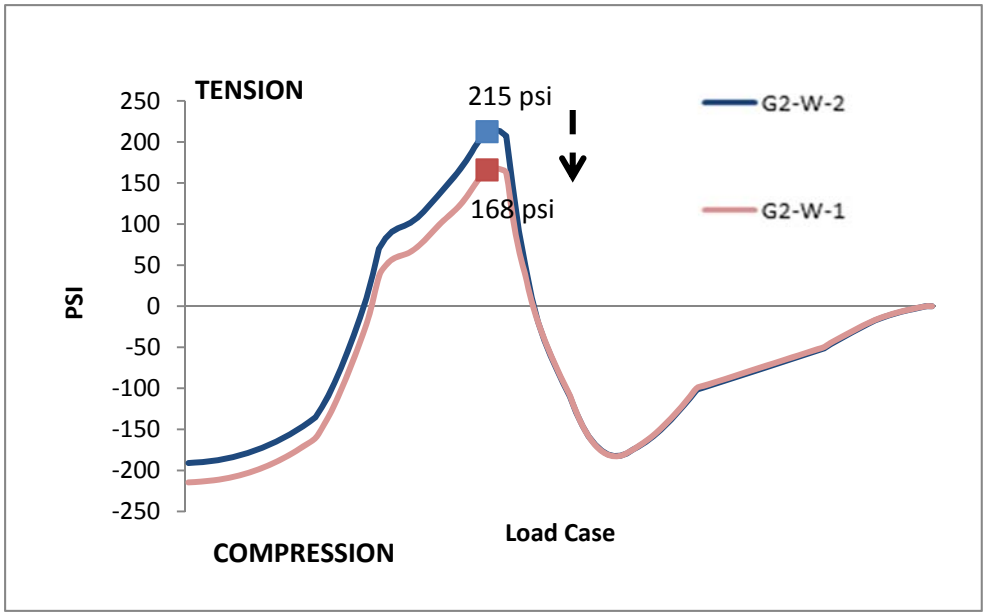

Figure 5.10 Web FEA Test Results for Gauge Location G2-W During Pass 1 for US-13

occurs at approximately the same point in time for both the bottom flange and web. However, if lateral bending is being applied to the girders then a stress gradient is expected, which is clearly shown in Figure 5.11 after the separation point.

This biaxial bending of the girders has a profound effect on the correlation of the field measurements and FEA results. Figure 5.12 shows typical FEA output, for stresses at the same loading and locations shown in Figure 5.12 (Locations G1-W and G1-BF). Figure 5.12 shows that while the bottom flange FEA results show a similar trend as the field results in Figure 5.11, the web FEA results have a much less significant lateral stress gradient. Supplemental analyses were thus performed in order to explore improving the accuracy of the model by modeling selected cross-frame members as shell elements and refining the manner in which the cross-frame elements are connected to the remainder of the structure. Specifically, all members of the instrumented cross-frame (4-4) framing into the instrumented G1 girder cross-section were modeled with shell elements and these members were connected to the girder connection plate via MPC links at 3 nodes at the end of each member; these MPC connections constrained all degrees of freedom on the cross-frame node relative to the displacements and rotations of the corresponding connection plate node. These three MPCs represent the three bolts used in the field to connect the cross-frames to the girder transverse stiffener serving as a connection plate.

Figure 5.13 shows the output based on these more refined models that corresponds to the data shown in the previous two figures (for G1-W and G1-BF under the same loading conditions). This shows that these more refined models are able to reproduce the fluctuations between tension and compression that were observed in the field data with remarkable accuracy. Figure 5.14 shows the percent errors of the original and more refined FEA relative to the field test measurements. These results show significant reductions in percent errors for both tension and compression for the two web gauges located adjacent to the cross-frame where refined modeling techniques

were used. The largest percent error reduction in tension was achieved at G1-W-2, where the error was reduced from 55% to 5%; the largest percent error reduction in compression was achieved at the same gauge, where the reduction was from 151% to 46%. These results suggest that either element type, shell-to-shell connectivity, or both might play a major role in the accuracy of the FEA web results, especially when considering that only one of the many cross-frames in the model is revised to obtain these dramatically improved results. This topic is further explored in the Section 5.1.1.3.

The second web stress-related metric that was used for FEM validation was the neutral axis, where the calculation procedure for this was as discussed in Section 5.2.3 The resulting neutral axis (NA) locations (measured from the bottom of the bottom flange) from the field test, FEA, and hand calculations are included in Table 5.4 below. Figure 5.15 graphically shows this same data. These results can be put in perspective relative to the following girder dimensions: the depth of the web is 66 inches; the depth of the steel section is 67.75 to 70.125 inches; and the depth of the entire composite section is 80.00 to 81.25 inches.

Theoretical values for the NA position for each of the locations were calculated based on the girder geometry (which varies slightly for each of the three cross-sections) assuming both a 4 ksi and 5 ksi compressive strength of concrete. Both of these data sets are reported in Table 5.5, although minimal sensitivity to these values is observed. As a result, expected NA values are between 54 and 58 in. The FEA NA positions compare relatively well to these results, where the values vary based on load position between 59.3 and 63.3 inches for G1, between 45.7 and 51.6 inches for G2, and 56.2 and 57.6 inches for G3. The data in Table 5.4 shows that the NA position typically lowers as the pass number increases (i.e., the load moves farther from the instrumented location). Weaker correlation with theoretical expectations is obtained in the field

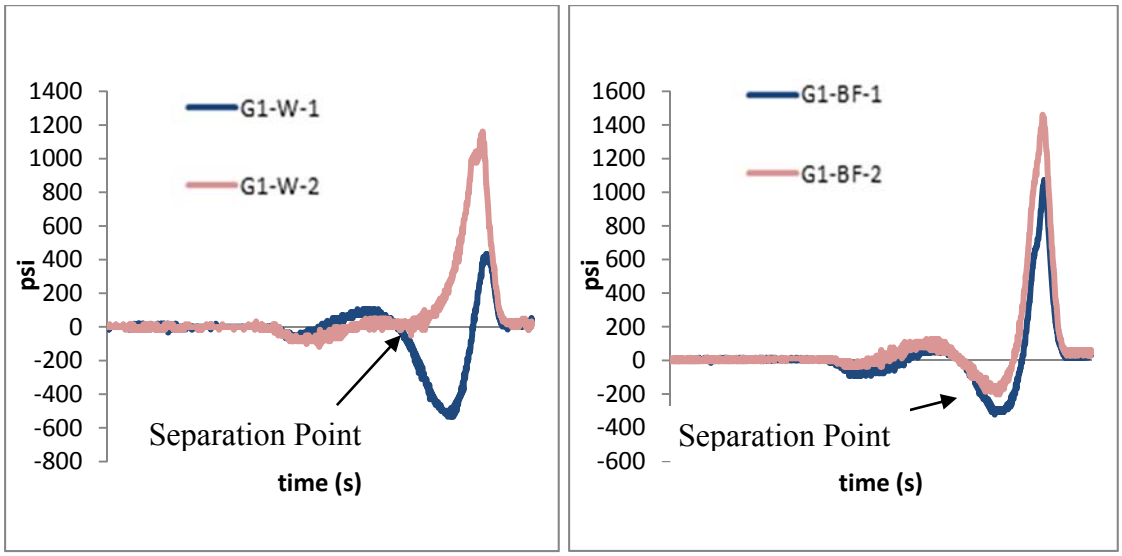

Figure 5.11 Web (left) and Bottom Flange (right) Stresses during Pass 1, Field Data, US-13

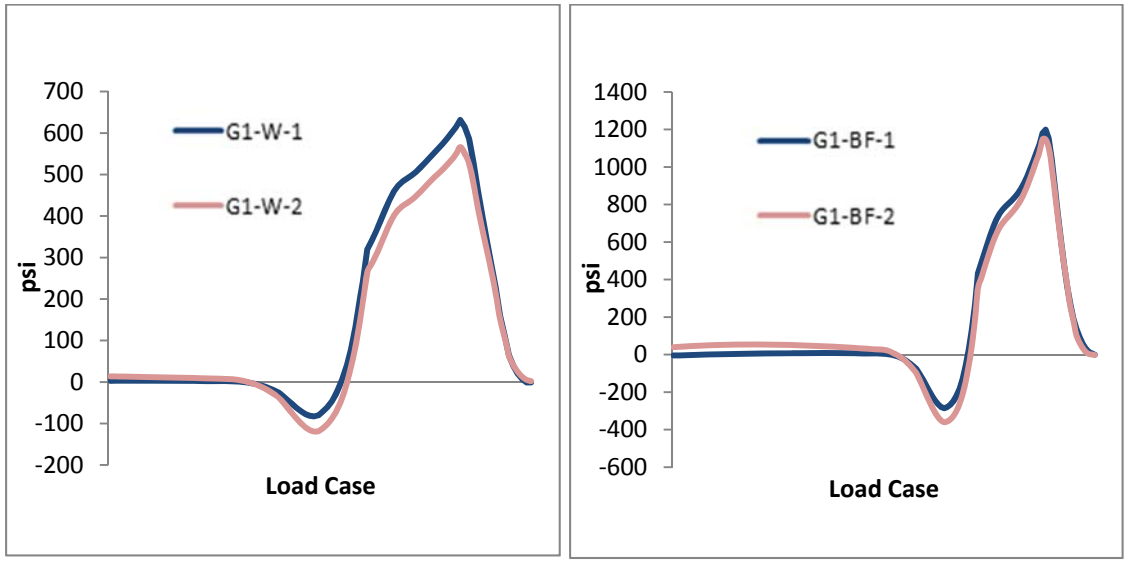

Figure 5.12 Web (left) and Bottom Flange (right) Stresses during Pass 1, FEA with Cross-frames Modeled as Beam Elements, US-13

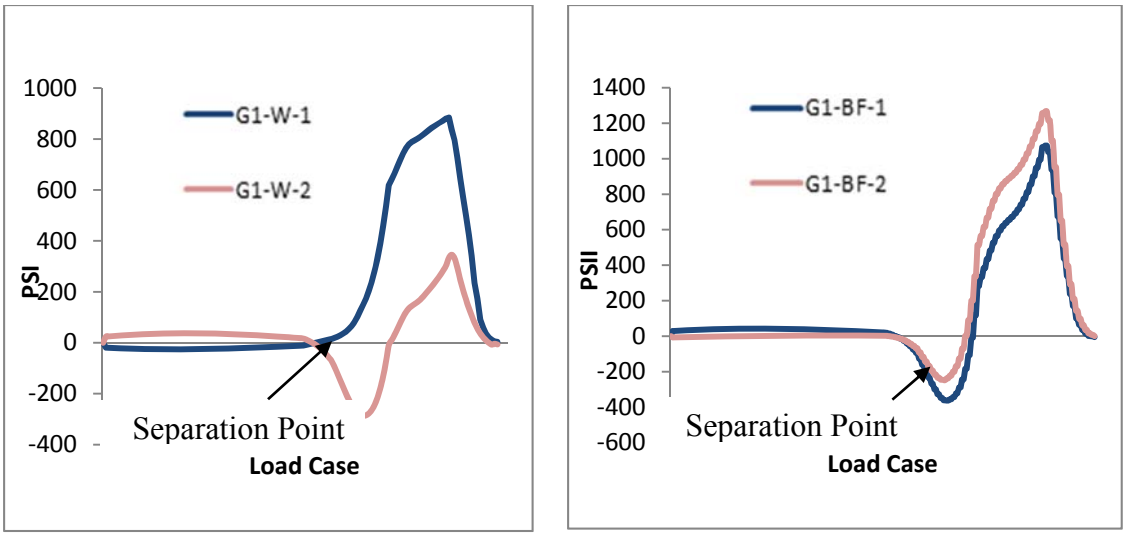

Figure 5.13 Web (left) and Bottom Flange Stresses (right) During Pass 1, FEA with Cross-frames Modeled as Shell Elements, US-13

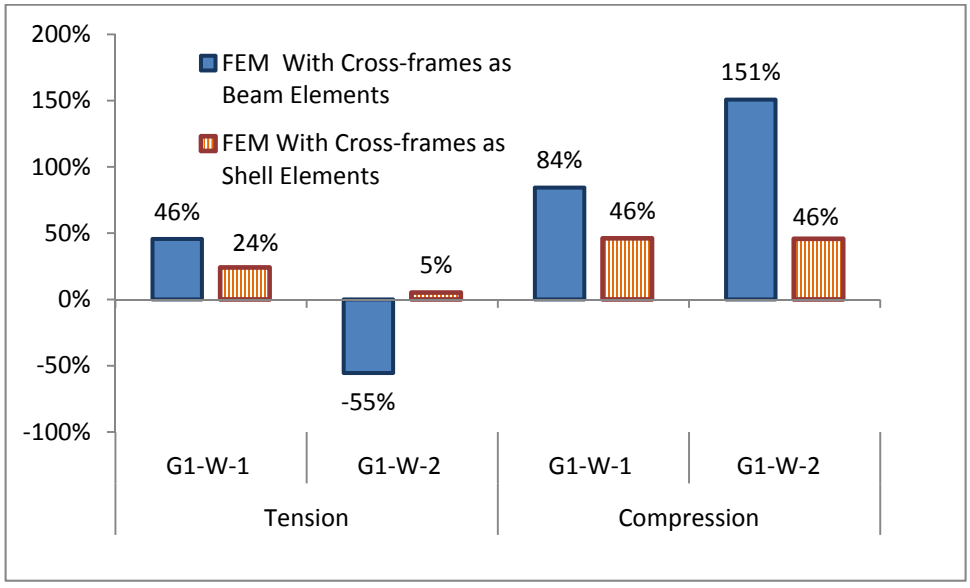

Figure 5.14 Percent Errors Between Field Measurements and FEMs Modeled with Beam and Shell Elements

results, where NA positions are between 59 and 86.1 inches for G1 (where the latter value is entirely unrealistic considering the depth of the entire cross-section is only 79.5 inches at this cross-section), between 37.8 and 43.3 inches for G2, and 31.5 and 35.2 inches for G3. This weaker correlation is influenced by the lateral stress gradient in the field web stresses, which generally produces lower average field web stresses than those

from the FEA, which in turn predicts a lower NA position. No lateral stress gradient is assumed in the theoretical calculations, explaining the better correlation with the FEA results, where a minimum stress gradient is predicted. Thus, the favorable comparison between the FEA and theoretical NA positions suggest that the vertical bending stiffness is being properly modeled.

Table 5.5 Neutral Axis Locations for Field Tests, FEA, and Theoretical Calculations, US-13

	Field Test N.A. Estimates (in)			**FEA N.A. Estimate (in)**			**Theoretical N.A. (in)**	
Gauge Location	Pass 1	Pass 2	Pass 3	Pass 1	Pass 2	Pass 3	4 ksi	5 ksi
G1	86.1*	64.0	59.0	63.3	60.0	59.3	57.0	58.2
G2	32.1	31.5	35.2	57.4	57.6	56.2	54.5	55.8
G3	86.1*	64.0	59.0	63.3	60.0	59.3	57.0	58.2

* Calculated NA is higher than total depth of composite section

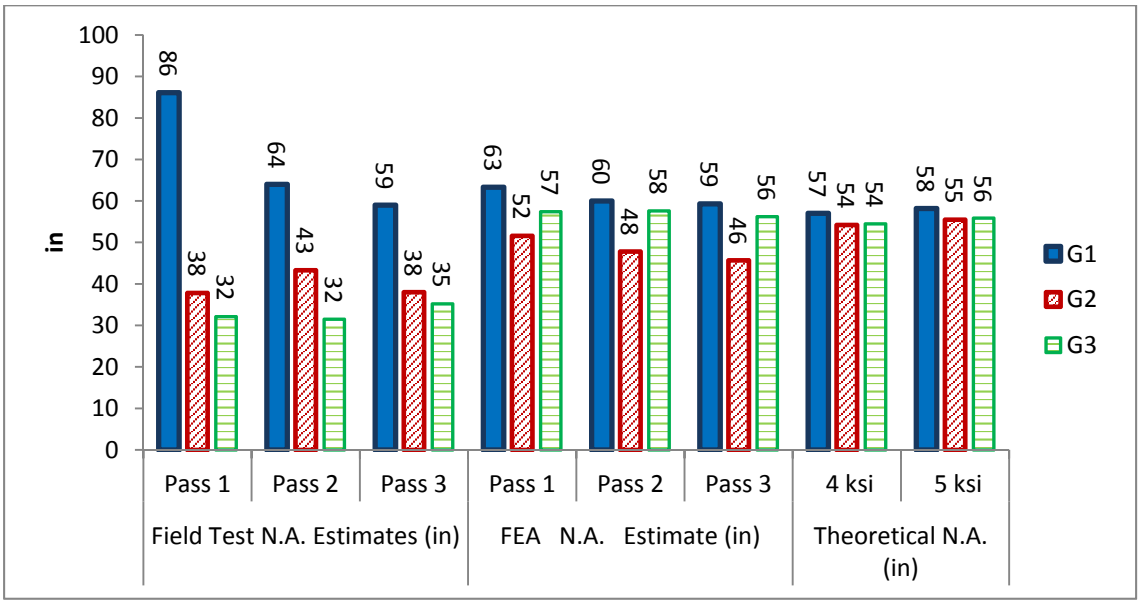

Figure 5.15 Neutral Axis Locations for Field Tests, FEA, and Theoretical Calculations, US-13

5.3.1.3 **Cross-frame Results for US-13**

5.3.1.3.1 **Field and FEA Data**

Tables 5.6 through 5.8 list the maximum tensile and compressive stress values recorded from the more-heavily loaded concentric leg field gauges and the FEA for each of the three passes of the load vehicle, respectively. The percent errors reported in Tables 5.6 through 5.8 are calculated relative to the field data, in the same manner as calculated for the bottom flange and web results discussed above. Four cases were excluded from the tables because relevant data points were missing from the signal. These criteria for data exclusion were based on visual inspection of the stress plots as shown in Figure 5.16, which shows a typical excluded signal. Furthermore, a maximum tensile value of -2 psi is indicated for Gauge 12-3-H during Pass 3 because this is the maximum stress recorded for at this gauge location which never experiences tension.

Figures 5.17 and 5.19 provide a graphical view of the data shown in Tables 5.6 through 5.8. Here it is shown that the FEA accurately produces the general trends observed in the field testing and that a favorable quantitative comparison is obtained in some cases, but that in regions of peak stress the field test results are typically of higher magnitude than the FEA results. These figures also show that the FEA accurately captures locations and conditions leading to of peak stress. Specifically, it is found that the maximum overall cross-frame stress in the FEA (3166 psi, in tension) occurred at the same location and under the same load pass as in the field test (4-4-G during Pass 1). Similarly, the maximum overall cross-frame compressive stress in the FEA (2502 psi) also occurred at the same location (4-4-C) and under the same loading pass (Pass 1) as it was in the field test.

The best overall correlation between the field and FEA data was achieved for the maximum tensile stresses measured at Gauge 4-4-C during Pass 2 (Figure 5.18); in this case the calculated FEA result was the same as the field result. The best correlation

Table 5.6 Maximum Cross-frame Stresses, US-13, Pass 1

	Tension			Compression		
Gauge Position	**Field data**	**FEA data**	**% Error**	**Field data (psi)**	**FEA (psi)**	**% Error**
4-4-A	678	382	44%	-2979	-2502	16%
4-4-C	627	382	39%	-3133	-2502	20%
4-4-E	3300	3166	4%	-	-	NA
4-4-G	4218	3166	25%	-612	-292	52%
4-4-I	1162	377	68%	-157	-105	33%
4-4-J	1052	377	64%	-140	-105	25%
11-3-B	1356	843	38%	-893	-727	19%
11-3-F	924	406	56%	-1540	-1052	32%
11-3-H	777	406	48%	-1384	-1052	24%
11-3-I	419	57	86%	-261	-267	-3%
11-3-J	478	57	88%	-294	-267	9%
12-3-B	1062	732	31%	-297	-224	25%
12-3-D	458	732	-60%	-108	-224	-107%
12-3-H	658	686	-4%	-206	-288	-40%
12-3-I	1392	605	57%	-353	-324	8%
12-3-J	1315	605	54%	-339	-324	4%
12-4-A	761	248	67%	-2467	-1835	26%
12-4-C	151	248	-64%	-2916	-1835	37%
12-4-G	2850	747	74%	-839	-239	72%
12-4-I	226	604	-167%	-167	-323	-93%
12-4-J	244	604	-148%	-151	-323	-114%
14-3-B	1299	607	53%	-128	-129	-1%
14-3-F	918	1672	-82%	-83	-67	19%
14-3-H	1422	1673	-18%	-52	-67	-29%
14-3-I	2453	1209	51%	-163	-93	43%
14-3-J	2491	1209	51%	-146	-93	36%

Table 5.7 Maximum Cross-frame Stresses, US-13, Pass 2

	Tension			Compression		
Gauge Position	**Field data**	**FEA data**	**% Error**	**Field data**	**FEA (psi)**	**% Error**
4-4-A	493	473	4%	-2506	-2351	6%
4-4-C	473	473	0%	-2326	-2351	-1%
4-4-E	2224	2386	-7%	-	-	NA
4-4-G	2488	2387	4%	-423	-320	24%
4-4-I	236	193	18%	-	-	NA
4-4-J	263	193	27%	-	-	NA
11-3-B	1624	1252	23%	-609	-571	6%
11-3-F	887	504	43%	-1476	-1318	11%
11-3-H	887	504	43%	-1334	-1318	1%
11-3-I	380	58	85%	-257	-405	-58%
11-3-J	447	58	87%	-284	-405	-42%
12-3-B	2082	1487	29%	-269	-183	32%
12-3-D	1227	1487	-21%	-111	-183	-64%
12-3-H	284	0	100%	-678	-483	29%
12-3-I	1192	535	55%	-260	-205	21%
12-3-J	1121	535	52%	-238	-205	14%
12-4-A	899	365	59%	-2627	-2002	24%
12-4-C	293	366	-25%	-2651	-2002	24%
12-4-G	2850	1456	49%	-839	-542	35%
12-4-I	594	7	99%	-780	-531	32%
12-4-J	244	7	97%	-620	-531	14%
14-3-B	3161	1727	45%	-160	-47	71%
14-3-F	1027	631	39%	-84	-210	-150%
14-3-H	774	632	18%	-48	-55	-14%
14-3-I	2897	1495	48%	-176	-78	56%
14-3-J	3016	1495	50%	-160	-78	51%

Table 5.8 Maximum Cross-frame Stresses, US-13, Pass 3

	Tension			Compression		
Gauge Position	**Field data**	**FEA**	**% Error**	**Field data (psi)**	**FEA (psi)**	**% Error**
4-4-A	647	546	16%	-2076	-1957	6%
4-4-C	537	546	-2%	-1830	-1957	-7%
4-4-E	1274	1704	-33%	-283	-343	-21%
4-4-G	1749	1705	3%	-438	-344	22%
4-4-I	319	249	22%	-263	-213	19%
4-4-J	105	249	-137%	-263	-213	19%
11-3-B	1946	1358	30%	-493	-501	-2%
11-3-F	873	1358	-56%	-2480	-501	80%
11-3-H	922	564	39%	-2340	-1696	28%
11-3-I	469	114	76%	-423	-546	-29%
11-3-J	653	114	82%	-357	-547	-53%
12-3-B	2297	1736	24%	-223	-161	28%
12-3-D	1518	1736	-14%	-111	-161	-44%
12-3-H	167	-2	101%	-1306	-1219	7%
12-3-I	781	346	56%	-168	-145	14%
12-3-J	725	345	52%	-160	-144	10%
12-4-A	766	436	43%	-2593	-1858	28%
12-4-C	228	0	100%	-2326	-1261	46%
12-4-G	1567	1029	34%	-399	-500	-25%
12-4-I	444	26	94%	-1117	-777	30%
12-4-J	374	26	93%	-972	-777	20%
14-3-B	3588	2135	40%	-142	-42	70%
14-3-F	36	149	-314%	-1638	-290	82%
14-3-H	42	149	-255%	-790	-290	63%
14-3-I	2634	1370	48%	-144	-70	52%
14-3-J	2761	1371	50%	-143	-70	51%

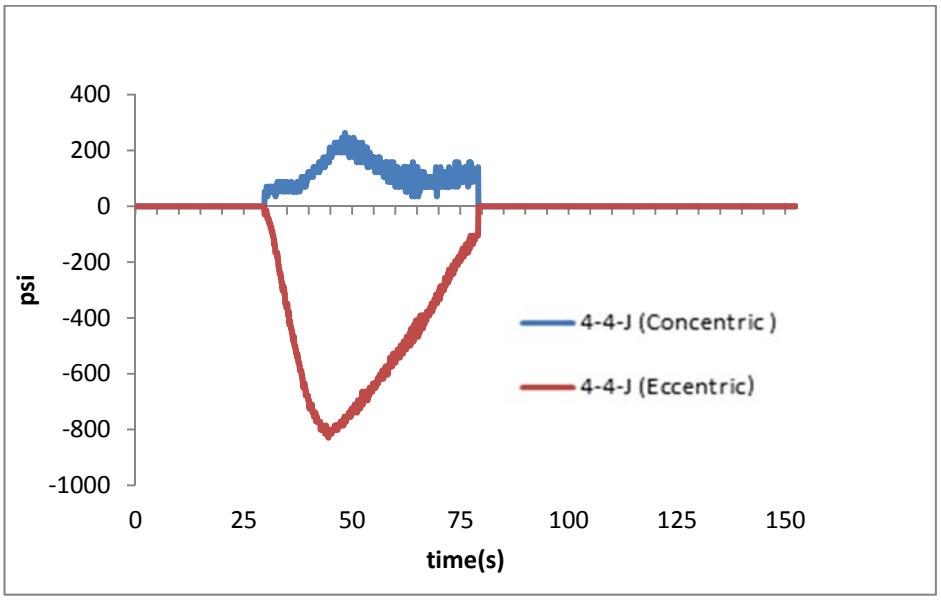

Figure 5.16 Typical Results from Gauges Excluded From Data Set, Gauge 4-4-J, Pass 2

correlation for maximum compressive stress (Figure 5.17) was achieved at: 14-3-B during Pass 1, 11-3-H during Pass 2, and 4-4-C during Pass 2 (Figure 5.18). In these cases the FEA results were only 1% different from the field results. It is also noted that two of these locations (4-4-C and 11-3-H) report stress values among the highest recorded for compression in Pass 2, indicating that the model does accurately capture peak stresses in some situations.

The highest absolute value of percent error (314%) was obtained for maximum tensile stress at Gauge 14-3-F during Pass 3 (Figure 5.19). However, the field and FEA stresses on which this percent error calculation is based are of relatively low magnitude such that the relative difference between the two values is only 113 psi. This also represents an unusual situation where the field result is lower than the FEA result, which may suggest a potential gauge malfunction at this gauge for this pass. Excluding results such as this where the highest values of percent error were based on the lowest values of relative error (which was quantified by excluding data sets where both the field and FEA results were less than 300 psi), the highest absolute value of percent error

is 82%, which occurs at 14-3-B during Pass 1. The highest relative error also occurs during Pass 1, 2103 psi at 12-4-G. This represents the most extreme situation where the field data reports significantly higher stress than the FEA.

Similar to the differences in web stresses discussed in the previous section, a reason for the discrepancy between the field and FEA results is likely related to the level of refinement of the cross-frame modeling. Specifically, in the physical connection, one leg of the angle is bolted to a girder connection plate as shown in the left side of Fig 5.20. This alignment results in a small offset distance between the point where the loads are transferred from connection plate to the centroid of the angle cross-section. As shown in the view of the FEM provided in the bottom right of Figure 5.20, this offset distance is not accounted for in the model. To explore the influence of these additional models were created where the cross-frames were modeled with shell elements (as mentioned previously in Section 5.3.1.2) and an offset distance of 0.785 in. was used. Because the cross-frame gauges were very close to the cross-frame connections (as shown conceptually in the bottom left figure of Figure 5.20), it was hypothesized that even a small deviation from accurately representing these end conditions could have a significant effect.

Figure 5.21 shows Cross-frame 4-4 (which had the highest recorded cross-frame stresses) modeled with shell elements and the gauge locations of interest on the right side of the figure (as well as the adjacent cross-frame, 3-4, modeled with beam elements on the left). Data was extracted from the shell cross-frame elements corresponding to these gauge locations and compared to the field data as shown in Table 5.9. The FEA data from the original model where beam elements were used to represent all cross-frames is also shown here for comparison. This shows that, in contrast to the girder results from the shell element model shown earlier, there is not a consistent improvement in the cross-frame stress correlation between the shell cross-frame and field cross-frame results. For example, while a reduction in error was achieved at

Gauges 4-4-I and 4-4-J, the error was increased for gauges 4-4-A and 4-4-C. The error for Gauge 4-4-G in tension remained the same (at 25%), while the error for the same gauge in compression differed by only 1%.

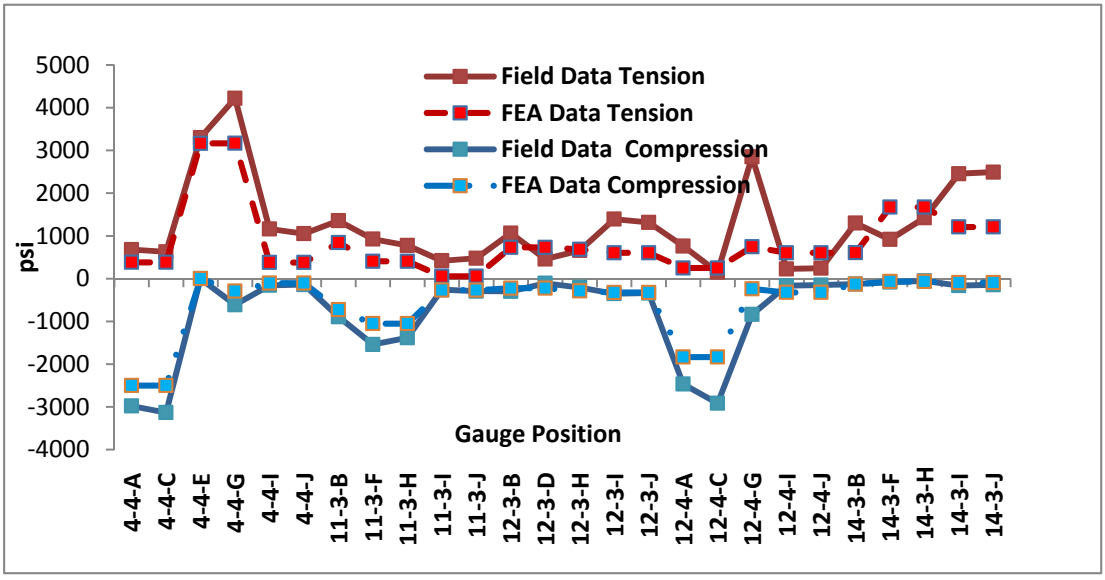

Figure 5.17 Maximum Tensile and Compressive Cross-frame Stresses for US-13, Pass 1

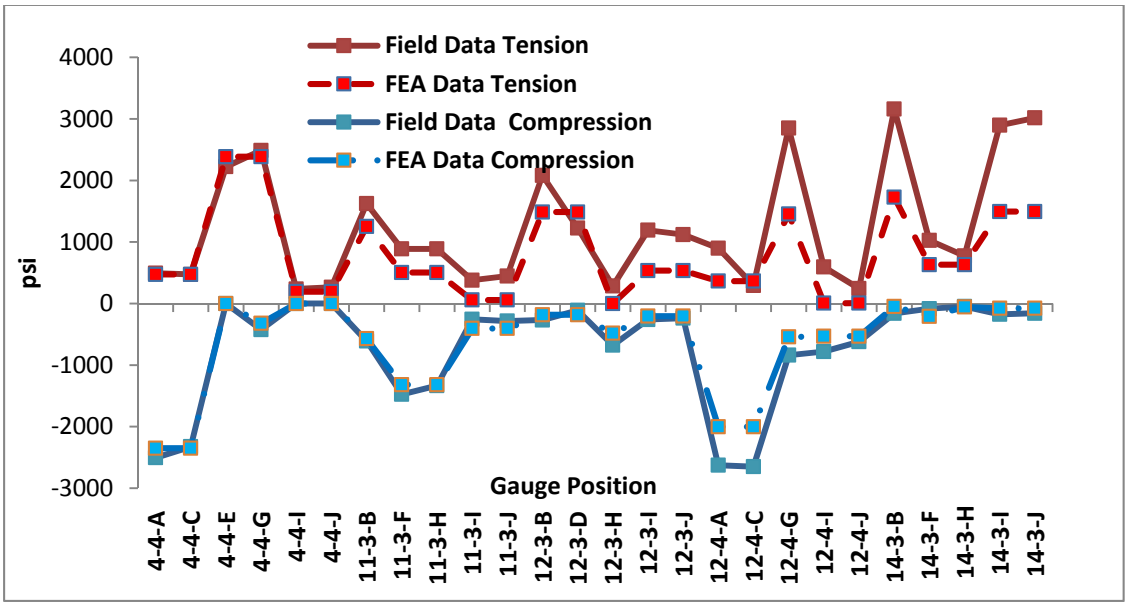

Figure 5.18 Maximum Tensile and Compressive Cross-frame Stresses for US-13, Pass 2

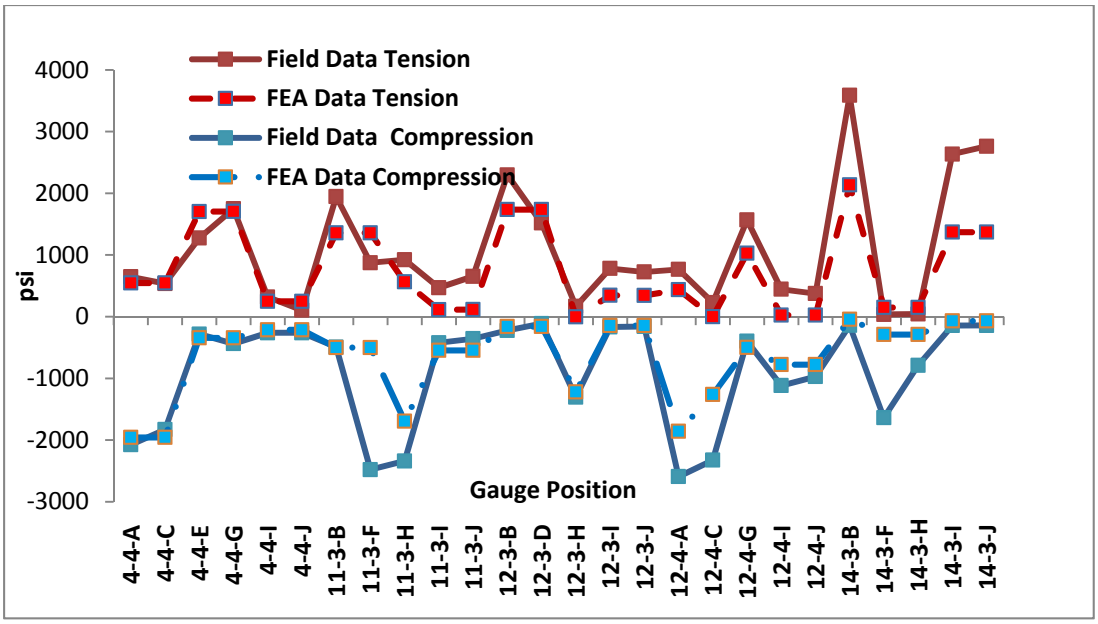

Figure 5.19 Maximum Tensile and Compressive Cross-frame Stresses for US-13, Pass 3

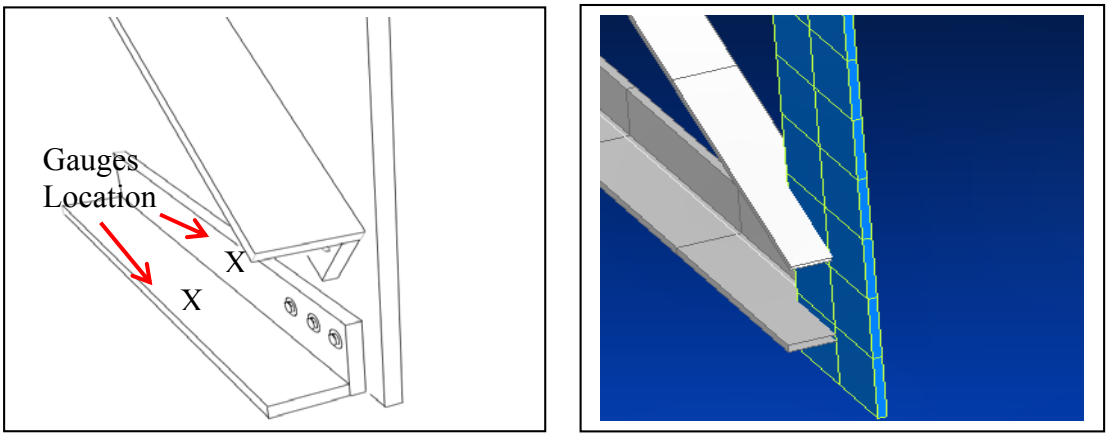

Figure 5.20 Cross-frame Connection Detailing, Field (left) and Rendered View of Original FEM (right

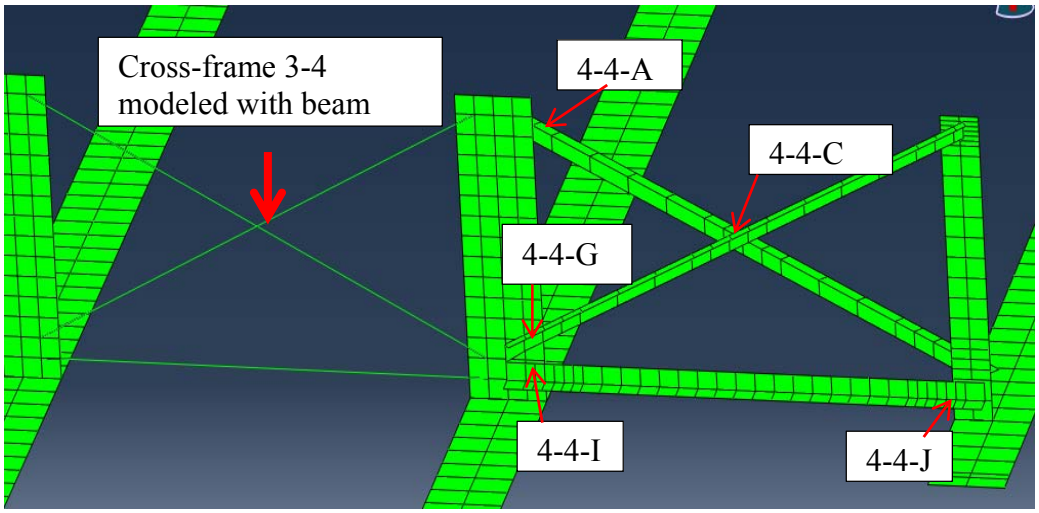

Figure 5.21 Cross-frame 4-4 Modeled with Shell Elements, US-13

Table 5.9 Percent Error Comparison Between Field, Shell FEA, and Beam FEA Stresses in Cross-frame 4-4, US-13, Pass 1 Measurements and FEA of Shell Modeled Cross-frame 4-4

		4-4-A	4-4-C	4-4-G	4-4-I	4-4-J	Average (Using Absolute Values)
Tension	Field Stress (psi)	678	627	4218	1162	1052	
	Shell Element Stress (psi)	320	323	3180	483	1452	
	Shell Element % error	53%	48%	25%	58%	-38%	44%
	Beam Element Stress (psi)	382	382	3166	377	377	
	Beam Element % Error	44%	39%	25%	68%	64%	48%
Compression	Field Stress (psi)	-2979	-3133	-612	-	-	
	Shell Element Stress (psi)	-2242	-2304	-300	NA	NA	
	Shell Element % error	25%	26%	51%	NA	NA	34%
	Beam Element Stress (psi)	-2502	-2502	-292	NA	NA	
	Beam Element % Error	16%	20%	52%	NA	NA	29%

5.3.1.3.2 **Observed Structural Response**

The maximum overall tensile stress (4218 psi) was recorded in the field at Gauge 4-4-G during Pass 1, while the maximum compressive stress (3133 psi) was also recorded in the field during the same pass and on the same cross-frame, but at different gauge location (4-4-C). This cross-frame (4-4) is adjacent to the obtuse corner of the bridge (see Figure 4.3) and these two specific gauge locations are in equivalent positions near the connection plate connecting the two opposing inclined members on which these gauges are installed (see Figure 4.5).

These locations of maximum cross-frame stress, close to the bridge support, may be unexpected if the cross-frames are only considered as secondary elements. Based on a 1-D analysis, as used in present design methods, for this 2-span continuous bridge it would be found find that maximum negative bending moments in the girders are at the pier support, while maximum positive bending moments are at mid-span locations. Thus, if only the cross-frames role in load distribution and lateral bracing is considered, it would be expected that the maximum cross-frame stresses would occur at the location of the maximum girder bending stresses.

However, in skewed bridges it is known that the obtuse corner of the bridge is a critical point in the structure. The FEA results based on the load passes used in the field testing for this bridge confirm this by reporting a maximum reaction force (31,348lb) at the south end of Girder 5 (at the obtuse corner) that is 19% larger than the maximum reaction force (25,46lb) at the same end of the adjacent girder (Girder 4, see Figure 5.22) despite the fact that the loading inducing these reactions is closer to Girder 4.

Thus, these reactions are one means of quantifying the torsional force component induced by the skewed supports, which is shown to amplify both the reactions and cross-frame stresses in the obtuse corner of the bridge.

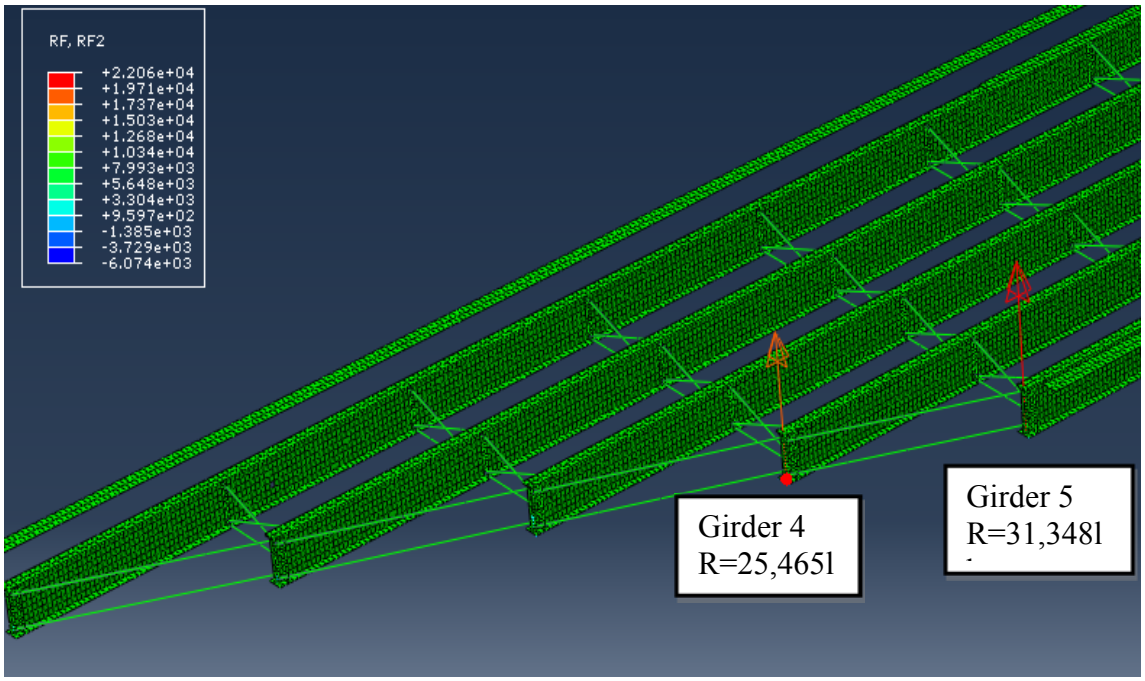

Figure 5.22 Girder 4 and Girder 5 Vertical Reaction Forces at South Support, Pass 1, US-13

To further put these peak cross-frame stresses in perspective, adjacent girder and cross-frame readings can be compared. During the field test the maximum measured stress was at the bottom flange mid-span gauges (at G3-BF-1 during Pass 1) and equal to 1475 psi. This is 25% larger than the maximum girder stress measured at the instrumented cross-section near the south support (G3), which was 1180 psi at gauge G1-BF-1 at the left end support (1180 psi). At the same time, the maximum stress measured in the adjacent cross-frame (at Gauge 14-3-J) during the same pass (2491 psi) is 41% less than the maximum measured cross-frame stress near the south abutment (4218 psi at Gauge 4-4-G). This further demonstrates the effects of bridge skew on cross-frames stresses.

The difference in stresses along the length of cross-frame members can also be used to evaluate cross-frame behavior. For example, if only axial loads are present in a member, the stress would be equal along the length of the member (excluding the possibilities for changes in load, and therefore stress, where connections to other

members occur). Therefore, in such a situation, gauges that are placed at different cross-sections on the same cross-frame members would record the same stresses under the same loading. However, the results show differences in measured stresses, especially in diagonal members experiencing tension. Such data provides a means for assessing the relative magnitudes of axial and bending forces in these members. For example, Gauges 4-4-E and 4-4-G are located on the same diagonal member of the cross-frame. During Pass 1 the difference between the maximum stresses in the two gauges located on the concentric leg at these locations was 918 psi (3300 psi versus 4218 psi, respectively). When maximum readings from eccentric leg gauges from the same locations (4-4-E and 4-4-G) were compared the difference was 1078 psi (stress at 4-4-E was 1134 psi, while stress at 4-4-G was 56 psi). Comparing these variations in stress both along the length of the member and within the cross-sections suggests that the diagonal cross-frame member on which these gauges are attached are experiencing stresses not only from axial loads, but from bending moments as well.

This phenomenon was also shown in the FEA results. Figure 5.23 shows FEA bending moments about the beam elements' local x –axis, which corresponds to the vertical plane, and thus lateral bending moments for Cross-frame 4-4 during Pass 1. Figure 5.24 shows equivalent data for bending moments about the beam elements' local y –axis, which is in the horizontal plane, and thus represents the effects of vertical bending. The bending moments shown in both of these figures correspond to Load Case 108, which is the load case that produced the peak stresses in the cross-frame. These results show that all cross-frame members are subjected to a significant amount of biaxial bending. Furthermore, the results also corroborate the field result that bending of the diagonals is more significant and variable than bending of the bottom chord. Specifically, the results show that the largest recorded x-axis bending moment (3362 lb*in), which occurs in the cross-frame diagonals, is 3.5 times larger than the corresponding output in the bottom chord of the cross-frame (963 lb*in). Similarly, the

largest recorded y-axis bending moment (3069 lb*in), which also occurs in the cross-frame diagonals, is 3.4 times larger than the corresponding output in the bottom chord of the cross-frame (-896 lb*in).

5.3.2 **Field Measurements and FEA Results for SR-299**

The results for SR-299 are organized in three primary sub-sections that follow the same format of the US-13 results. The first (Section 5.3.2.1) presents bottom flange field and FEA bottom flange data. This section also presents an analysis of the observed levels of lateral bending of the bottom flange. Section 5.3.2.2 presents web field and FEA data. Lastly, Section 5.3.2.3 presents cross-frame field and FEA data.

5.3.2.1 **Bottom Flange Results for SR-299**

As was the case for US-13, three girder cross-sections are instrumented for SR-299. However, in contrast to the US-13 instrumentation plan, the three cross-sections are located on two different girders, as previously discussed in Chapter 4. Specifically, Cross-sections G1 and G2 are located near mid-span of the east span of Girder 5, while Cross-section G3 is located on Girder 11 near the east obtuse corner of the bridge. The values reported in Table 5.10 and 5.11 are maximum concurrent stress gauge pair are identified and recorded and then the concurrent stress value occurring at the same time in the opposite gauge of the gauge pair is recorded. The same procedure is repeated for the FEA results, where concurrent stresses in gauge pairs due to common loading positions are recorded for each gauge pair. Percent error was calculated relative to the field test results as described in previous sections. Recall that as discussed in Chapter 4, the transverse position of the truck varied slightly during the two days of field testing

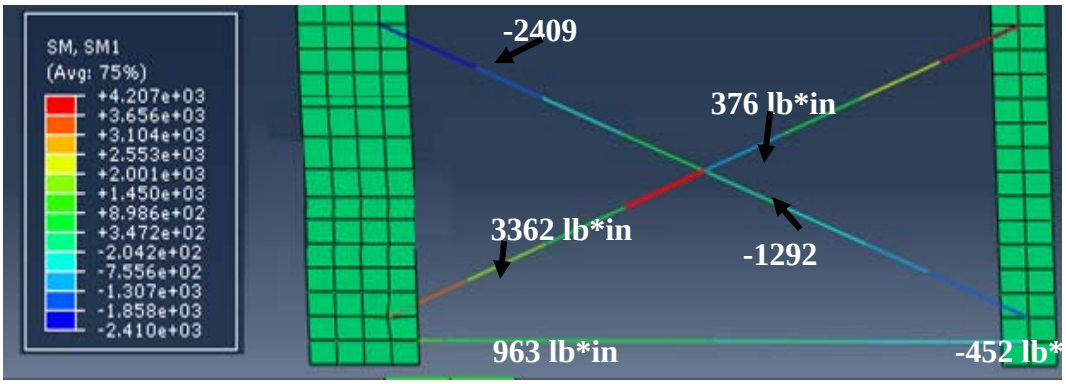

Figure 5.23 FEA Bending Moments about Beam Element Local x-axis, Lateral Moments, Cross-frame 4-4, Pass 1, Load Case 108, US-13 (in-lb)

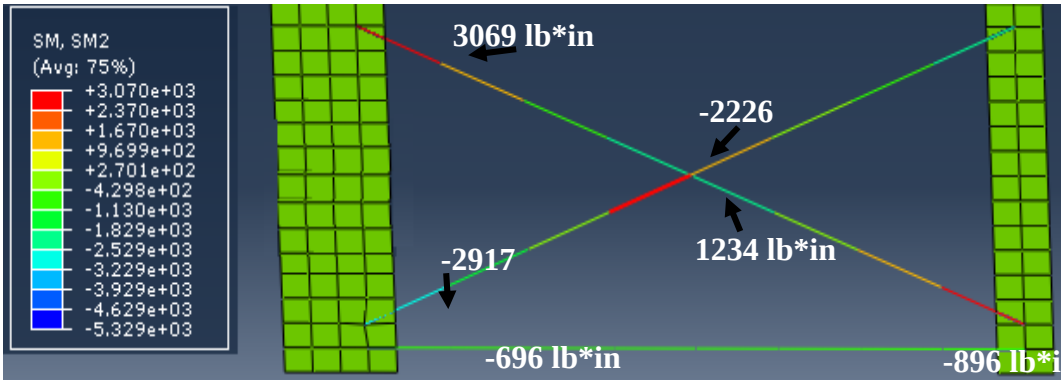

Figure 5.24 FEA Bending Moments about Beam Element Local y-axis, Vertical Moments, Cross-frame 4-4, Pass 1, Load Case 108, US-13 (in-lb)

and thus results for each day are reported separately. Figures 5.25 and 5.26 report this same data graphically.

These results generally show a larger deviation in field and FEA results than was obtained for US-13. Specifically, the FEA results for the passes which should maximize the maximum (tensile) stress results for each cross-section (i.e., Pass 1 for G1 and G2 and Pass 2 for G3) are much higher than the corresponding field results, 40% higher on average. In contrast, the compressive FEA stresses are 20% lower than the field results on average. One possible explanation for this difference is unintended fixity in the physical bearings that cause the peak positive bending moments to be lower in the field. The average percent difference for all individual gauges reported in Tables 5.10 and 5.11 is 2% despite all gauges having absolute values much larger than this. This

suggests that the loading effects and structural stiffness of the bridge are captured with reasonable accuracy, but that loading is being distributed differently in the field and FEA. Figures 5.25 through 5.28 also show that the FEA generally reproduces the trends in spatial variation in stress values, but that the magnitudes are not reliably predicted.

The best overall correlation between the field and FEA data was achieved for maximum compression stress at G2-BF-2 during Pass 1 Day 1 (Figure 5.26). In this case the FEA result was only 4% lower than the field data. The best correlation for maximum tension stress was achieved at G2-B2-1 during Pass 1 Day 1, where the FEA result was 12 % larger than the field result (Figure 5.25). Both of these situations involve the load pass traveling over the respective gauge locations.

In contrast, the worst overall correlation (467%) for both compression and tension stresses was at G1-BF-2 when Pass 2 Day 2 (loading on opposite side of the structure) caused compression in this gauge (Figure 5.28). For tension, the worst correlation (196%) occurred at the same gauge (G1-BF-2) during the same pass (Pass 2 Day 2, Figure 5.27). In both of these cases, the poor numerical correlation is due to the fact that the opposite gauge of the gauge pair (G1-BF-1) is the gauge where the maximum force effect was recorded and the FEA predicts significant amounts of lateral bending such that the concurrent G1-BF-2 readings are of opposite sign than both the maximum FEA G1-BF-1 stresses and the field results at both bottom flange gauges at this cross-section. By comparing the average bottom flange stresses when G1 is in tension due to this load pass (Table 5.10), it is seen that the vertical bending stresses correlate well (8% error). This fact coupled with a comparison of the relative magnitudes of the field and FEA stresses at each B1 gauge due to this load pass indicates that the poor correlation that is observed is due to the FEA predicting significantly more lateral bending than what is observed in the field.

This may be due to the level of refinement of the cross-frame modeling under-representing the lateral bending restraint in the FEA. Furthermore, if the peak stresses,

in contrast to the concurrent stresses, for G1-BF-2 in tension and compression in the field and FEA are compared, the relevant quantities are 154 psi and 43 psi for tension (respectively) and 127 psi and 161 psi for compression (also respectively). This suggests that, while the correlation of the compression data in particular significantly improves when viewed in terms of maximum stresses as opposed to concurrent stresses, it is recommended that future modeling of such situations should consider more detailed modeling of cross-frames and cross-frame-to- girder connections in order to accurately model the late lateral bending restraint provided by the physical cross-frames. This effect appears to be more critical in the staggered cross-frame configuration of SR-299.

The largest field tensile stress (1748 psi) was recorded in two scenarios: at G1-BF-1 during Pass 1 Day 1 and at G2-BF-1 during Pass 1 Day 2. The largest field measured compressive stress (296 psi) was also recorded in the latter situation, at G2-BF-1, during Pass 1 Day 2. The largest FEA tensile stress (3247 psi) was also computed in one of the situations producing the maximum field conditions, at G1-BF-1 during Pass 1 Day 1. The largest FEA compressive stress (256 psi) was computed at the opposite gauge in the same cross-section (G1-BF-2) during Pass 1 Day 2. This is the same loading scenario producing the maximum field response; while the gauge location corresponding to this effect is different in the field result, the two gauge locations differ only by a longitudinal distance of 2 ft. while being on opposite sides of the girder cross-section. In other words, in the FEA data, the maximum is obtained at cross-section G1 (adjacent to a cross-frame) while in the field data, the maximum is obtained at either Cross-section G1 or Cross-section G2 (located between cross-frames) and significant sensitivity to the Day 1 versus Day 2 load position is observed.

The theoretical maximum positive bending stress for an end span of a continuous-span bridge is typically assumed to be at a location of 40% of the span length, measured from the abutment. For this span of interest, this equates to 53.5 ft from the east abutment. Therefore, Cross-section G2 is closer to the theoretical location

of maximum bending stress and it would be expected to see that maximum tensile stresses recorded at these gauges. In the field results this occurs for Pass 1 Day 2, but not Pass 1 Day 1. As shown in Table 5.12, this statement is true in terms of both peak stress as well as average, vertical bending, stress although it is seen here that lateral bending constitutes 42 to 46% of the maximum vertical bending stress for each pass. Viewing the corresponding FEA results shown in Table 5.13, it is seen that the maximum vertical bending stress is obtained in Cross-section G2, as would be theoretically expected. However, Table 5.13 also demonstrates that the lateral ending stresses are significantly greater at cross-section G1 in the FEA, both relative to FEA Cross-section G2 results and the field results. This suggests either the lateral bending force is being over-estimated in the FEA or the lateral bending restraint is being under-estimated. Much less sensitivity to the Day 1 versus Day 2 load positions is also observed in the FEA results compared to the field results.

As was done in the US-13 model, the cross-frame modeling was also refined in select cross-frames of the SR-299 model to explore the influence of this refinement on the FEA accuracy. Specifically: Cross-frames 12-5, 12-4, 14-8, 14-9 and 14-10 were simultaneously modeled with shell elements instead of beam elements (as shown in Figure 5.29); the cross-frame-to-stiffener gusset plates were included in the model and connected to the stiffener with MPC elements; and connections between the cross-frames and gusset plates were formed via two MPC elements at each end of each member, with all degrees of freedom of the two adjoining elements being constrained. These latter two MPC elements were used to simulate the length of the weld connecting the angle and the gusset plate. Given that the typical length of the weld was 4 in. and the element size of the cross-frames is 3.5 in., two MPC elements are the number of these connections most accurately replicating the field conditions for this mesh size. It is noted that this is the same process used in refining the cross-frames in the US-13 model

Table 5.10 Maximum Concurrent Bottom Flange Stresses, Pass 1, SR-299

		Day 1		
Gauge Location	Action	Field Test (psi)	FEA (psi)	% error
G1-BF-1	Tension	649	503	22%
G1-BF-2	Tension	1748	3247	-86%
G1-AVG	Tension	1199	1875	-56%
G2-BF-1	Tension	1121	2161	-93%
G2-BF-2	Tension	1024	1752	-71%
G2-AVG	Tension	1073	1957	-82%
G3-BF-1	Tension	80	60	25%
G3-BF-2	Tension	46	37	20%
G3-AVG	Tension	63	48	24%
Average	Tension			-31%
G1-BF-1	Compression	-131	-255	-94%
G1-BF-2	Compression	-222	-253	-14%
G1-AVG	Compression	-177	-254	-44%
G2-BF-1	Compression	-196	-219	-12%
G2-BF-2	Compression	-180	-173	4%
G2-AVG	Compression	-188	-196	-5%
G3-BF-1	Compression	-226	-86	62%
G3-BF-2	Compression	-194	-9	95%
G3-AVG	Compression	-210	-47	77%
Average	Compression			7%

		Day 2		
Gauge Location	Action	Field Test (psi)	FEA (psi)	% error
G1-BF-1	Tension	1093	564	48%
G1-BF-2	Tension	1172	2780	-137%
G1-AVG	Tension	1132	1672	-48%
G2-BF-1	Tension	1748	2128	-22%
G2-BF-2	Tension	719	1454	-102%
G2-AVG	Tension	1234	1791	-45%
Average	Tension			-53%
G1-BF-1	Compression	-213	-152	28%
G1-BF-2	Compression	-192	-256	-33%
G1-AVG	Compression	-202	-204	-1%
G2-BF-1	Compression	-296	-184	38%
G2-BF-2	Compression	-55	-200	-265%
G2-AVG	Compression	-175	-192	-10%
Average	Compression			-63%

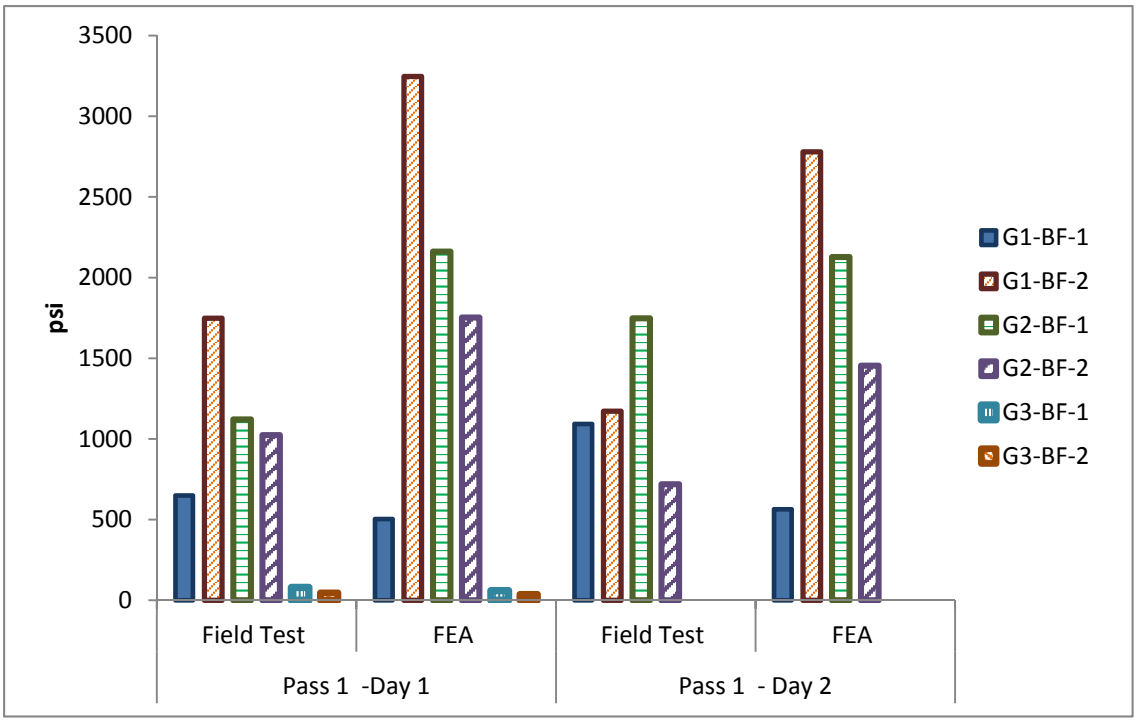

Figure 5.25 Maximum Concurrent Bottom Flange Tension Stress Data, Pass 1, SR-299

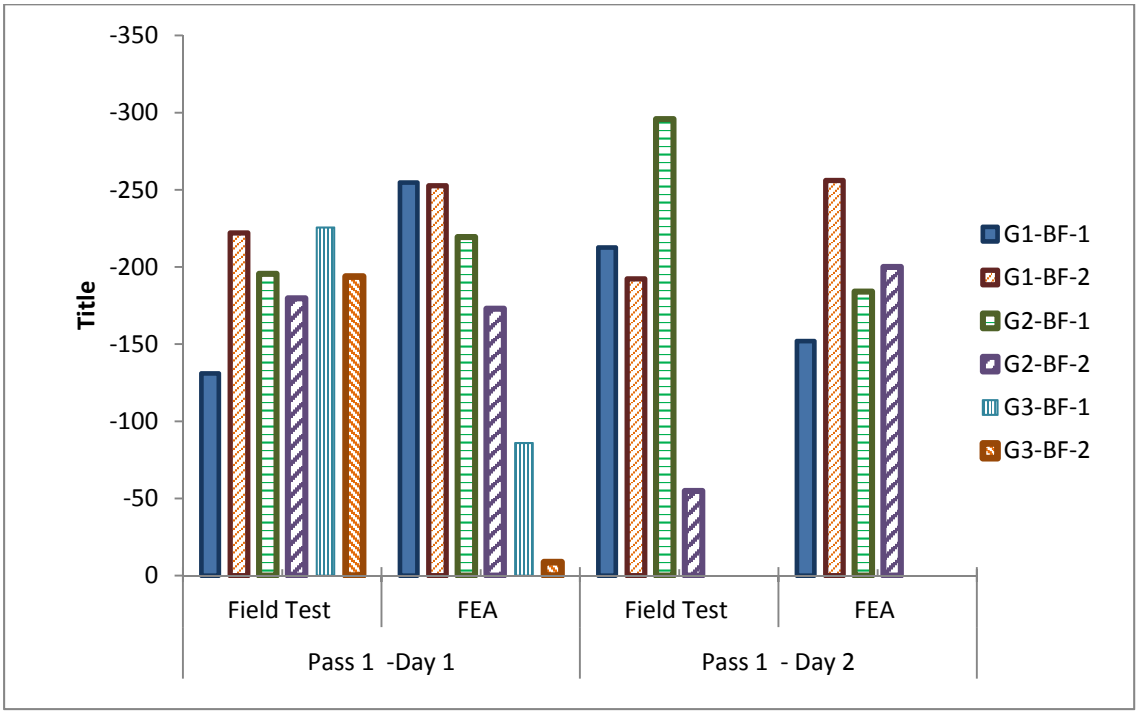

Figure 5.26 Maximum Concurrent Bottom Flange Compression Stress Data, Pass 1, SR-299

Table 5.11 Maximum Concurrent Bottom Flange Stresses, Pass 2, SR-299

		Day 1		
Gauge Location	Action	Field Test (psi)	FEA (psi)	% error
G1-BF-1	Tension	259	313	-21%
G1-BF-2	Tension	83	-2	103%
G1-AVG	Tension	171	155	9%
G2-BF-1	Tension	206	374	-82%
G2-BF-2	Tension	121	-62	151%
G2 -AVG	Tension	164	156	5%
G3-BF-1	Tension	853	1744	-104%
G3-BF-2	Tension	731	1577	-116%
G3-AVG	Tension	792	1661	-110%
Average	Tension			-12%
G1-BF-1	Compression	-117	-98	16%
G1-BF-2	Compression	-163	-102	37%
G1-AVG	Compression	-140	-100	38%
G2-BF-1	Compression	-148	-104	30%
G2-BF-2	Compression	-105	-79	25%
G2-AVG	Compression	-127	-91	28%
G3-BF-1	Compression	-75	-83	-10%
G3-BF-2	Compression	-38	-65	-73%
G3-AVG	Compression	-56	-74	-31%
Average	Compression			4%

		Day 2		
Gauge Location	Action	Field Test (psi)	FEA (psi)	% error
G1-BF-1	Tension	206	453	-120%
G1-BF-2	Tension	141	-135	196%
G1-AVG	Tension	173	159	8%
G2-BF-1	Tension	287	359	-25%
G2-BF-2	Tension	85	-63	174%
G2-AVG	Tension	186	148	20%
Average	Tension			56%
G1-BF-1	Compression	-146	-162	-10%
G1-BF-2	Compression	-114	417	467%
G1-AVG	Compression	-130	127	198%
G2-BF-1	Compression	-168	-102	39%
G2-BF-2	Compression	-76	-77	-2%
G2-AVG	Compression	-122	-90	26%
Average	Compression			115%

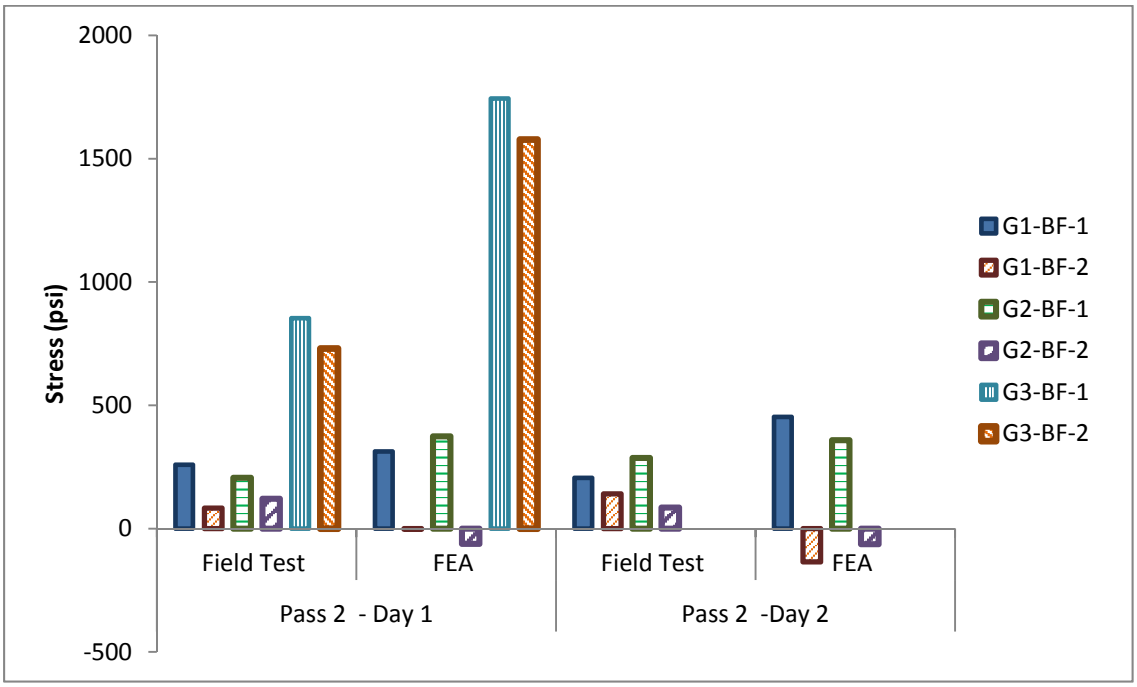

Figure 5.27 Maximum Concurrent Bottom Flange Tension Stress Data, Pass 2, SR-299

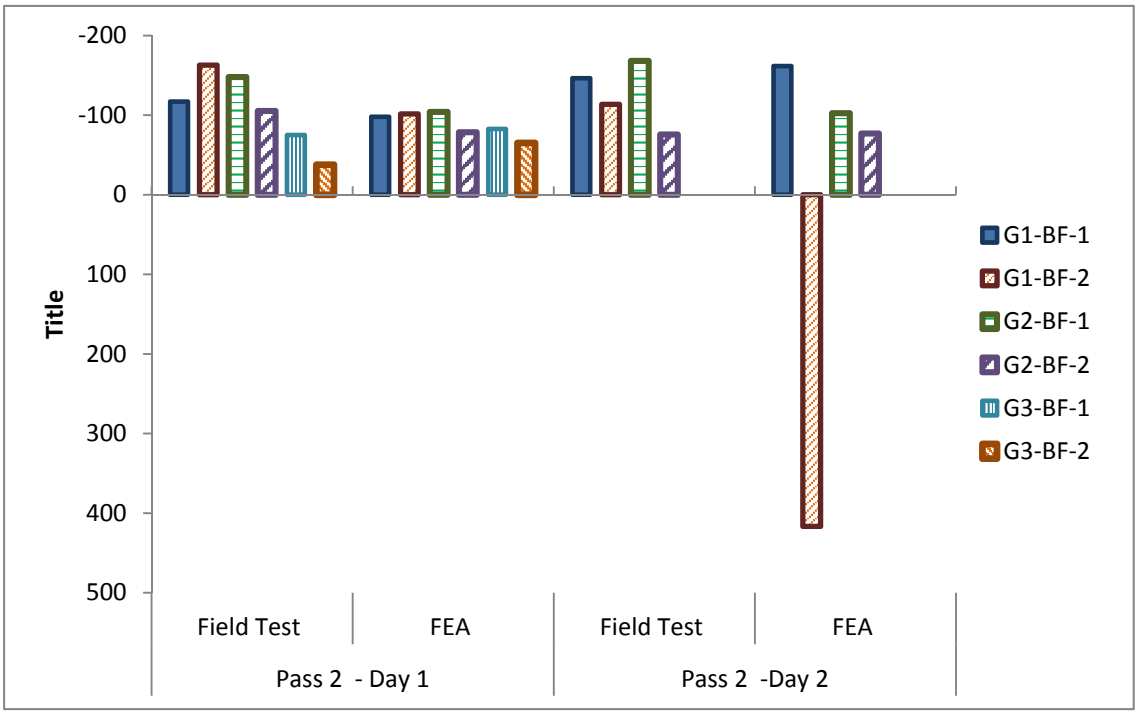

Figure 5.28 Maximum Concurrent Bottom Flange Compression Stress Data, Pass 2, SR-299

except that a greater number of cross-frames are simultaneously refined and the gusset plate (which does not exist in US-13) is added.

As a result of this effort, the percent error between the field and FEA data at G1-BF-2 during Pass 1 Day 2 (the gauge with the highest tension error during Pass 1) was reduced from 137% to 7% (a reduction in stress from 2780 psi to 1092 psi) in tension. A reduction in percent error were also detected at the opposite gauge of this gauge pair (G1-BF-1, which together are the only two gauges at which this intensive data analysis was performed) in tension; here the tensile stress percent error was reduced from 48% to 28% (corresponding to an increase in stress values from 564 psi to 789 psi). Comparing these values to the field data of these two gauges (1172 psi and 1093 psi, respectively), it is seen that the original FEA model significantly over-predicted the lateral bending in the girder and that the improved correlation is a direct result of improving upon this difference between the FEA and field results. When assessing the less critical compression results at this same girder cross-section under the same load pass, the refined FEA model also improves upon the overall correlation between the field and FEA results, but to a lesser extent. In terms of the percent error in the individual stresses, the percent error of the compression stress at G1-BF-2 was reduced from -33% to -11 % (a reduction in stress from256 psi to 236 psi) while the G1-BF-1 percent error was slightly increased from 28% to 38 % (based on a decrease in stress from 152 psi to 118 psi). These stress values can be considered relative to the field results at these two gauges of 192 psi and 213 psi, respectively.

These results show a significant influence of cross-frame modeling refinement on girder stress results, which suggests that further refinement of cross-frame and cross-frame connection modeling may further reduce the percent error between field and FEA results. Furthermore, this effect may be more pronounced for this structure (compared to US-13 where the bottom flange stresses obtained in the FEA with beam elements were generally satisfactory) due to the use of staggered cross-frames, and thus a greater

sensitivity to the rigidity of each individual cross-frame connection given that the cross-frame forces cannot be directly equilibrated by an opposing cross-frame on the opposite side of the girder cross-section.

The final portion of the bottom flange data analysis was to evaluate the relative contributions of vertical and lateral bending, as shown in Tables 5.12 and Table 5.13. The reader is referred to Section 5.3.1.1 for a discussion of the calculation process to obtain these values. The highest lateral bending stress (550 psi) was measured at G1-BF during Pass 1 Day 1, while the highest percent of lateral bending to vertical bending was measured at location G2-BF (69%) during Pass 1 Day 2 when compressive vertical bending stresses are present.

Similar behavior, in the sense that the highest overall lateral bending stress occurs when the girder is in positive bending but the lateral bending constitutes the largest percentage of the vertical stress when the girder is in negative bending, was also detected in the US -13 field results. However, the magnitudes of observed lateral bending stress in the field data of the two structures differ significantly. Specifically, the peak lateral bending stress in SR-299 is 3.7 times larger than the peak lateral bending stress observed in US-13 (550 psi vs. 149 psi). The lateral bending stress in SR-299 also

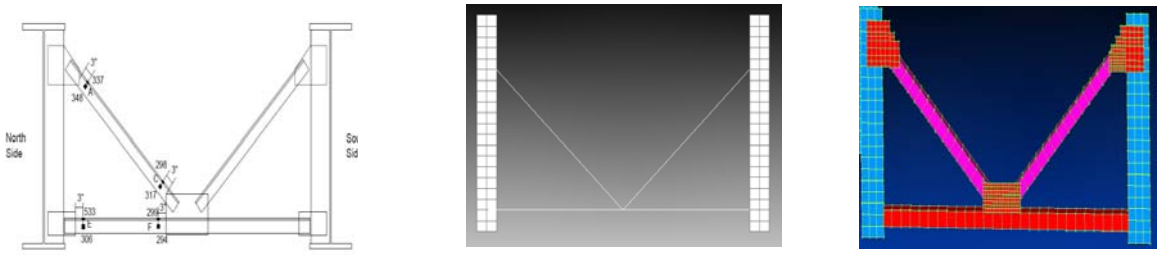

a) **b)** **c)**

Figure 5.29 Cross-frame Modeling, SR-299: a) Instrumented Cross-frame in the Field, b) Cross-frame Modeled with Beam Elements c) Cross-frame Modeled with Shell Elements

contributes more significantly to the total stress relative to the results for US-13, with SR-299 having a lateral to vertical bending stress ratio of 69% compared to the maximum value for this quantity in the US-13 results being 38%. The peak lateral bending stress of 550 psi occurs at cross-section G1 during Pass 1 Day 1 (constituting 46% of the vertical bending stress), although almost identical results are recorded at G2 during Pass 1 Day 2, where a lateral bending stress of 514 psi equal to 42% of the vertical bending stress was recorded. This points to a significant sensitivity to load position in the field results or SR-299. Furthermore, in general under the more critical positive vertical bending moments, the average lateral bending stresses at all cross-sections and passes is higher in SR-299 (28% versus 7%). It is hypothesized that this is due to the staggered cross-frame layout and this is a suggested topic for further evaluation in future studies.

Comparing the field and FEA data in Tables 5.12 and 5.13, respectively, it can be calculated that the FEA generally over-predicts the significance of the lateral bending stresses, with the lateral to vertical stress ratios in the FEA being 25% larger than those from the field test on average. Closer inspection reveals that this is primarily due to the FEA significantly over-predicting the significance of the lateral bending when G1 and G2 are in tension. The FEA ratios of lateral to vertical bending stress are on average 69% greater than the field results in these cases, while in all other cases the FEA lateral to vertical bending stress ratios are on average only 9% greater than the field results. In the FEA, the largest lateral ratio of lateral to vertical bending stress was computed during Pass 2 Day 2 at G1, where the lateral bending stress (289 psi) is 2.27 times larger than the maximum compressive vertical bending stress (12 psi). The largest magnitude of lateral bending stress (1372 psi) was computed at gauge location G1 during Pass 1 Day 1 in tension. This is one of the situations where the largest deviations in ratio of lateral bending stress were observed and this magnitude is also significantly higher than the maximum lateral bending stress in the field results, 550 psi.

5.3.2.1 **Web Results for SR-299**

Tables 5.14 and 5.15 report the maximum concurrent stress values in the web for the field and FEA results. Concurrent stresses are obtained in the same manner described previously, where the maximum tensile and compressive stresses for any gauge in each gauge pair are identified and recorded and then the concurrent stress value occurring at the same time (field results) or load case (FEA results) in the opposite gauge of the gauge pair is recorded. Percent error is calculated relative to the field test results, also consistent with the results presented in previous tables in this chapter. Table entries of "NA" were not instrumented during the pass of interest.

The highest web stress measured in the field (1009 psi) was at G2-W-1 during Pass 1 Day 2 and the highest web stress at a gauge location that was computed by the FEA was at the same gauge location during same pass and only 3% lower in magnitude (981 psi). The highest compressive stress measured in the field (193 psi) was at gauge location G2-W-1 during Pass 1 Day 2. The FEA also reported the highest compressive stress at the same gauge location during the same pass as the field results. These results differed in magnitude by 47% as the FEA value was 102 psi.

The best correlation between field and FEA results was achieved during the maximum tensile scenario discussed in the previous paragraph (Pass 1 Day 2 at G1-W-1), where the percent difference was 3%. The best correlation at an individual gauge location in compression was at G1-W-2 during Pass 1 Day 2, where the percent error is 12%, while the average web results at G1 when in compression due to Pass 2 Day 2 differ by only 6%.The worst overall correlation (431%) was when G2-W-2 was in compression during Pass 2 Day 2. However, the difference in the magnitude of the field and FEA results producing this percent error was only 90 psi. Furthermore, the recorded signal at this gauge was erratically varied between low values, with peaks oscillating between -30 and +21 psi. Since the peak tensile value at this gauge (21 psi) is

Table 5.12 Vertical and Lateral Bending Stresses (psi) For Bottom Flange, SR-299, Field Results

		Pass 1 Day 1				Pass 1 Day 2			
Action	Gauge Location	Field Test	Vertical bend.	Lateral bend.	% Lat/Ver	Field Test (psi)	Vertical bend.	Lateral bend.	% Lat/Ver
Tension	G1-BF-1	649	1199	-550	46%	1093	1133	40	3%
Tension	G1-BF-2	1748				1172			
Tension	G2-BF-1	1121	1073	49	5%	1748	1234	514	42%
Tension	G2-BF-2	1024				719			
Tension	G3-BF-1	80	63	17	27%	NA			
Tension	G3-BF-2	46							
Compression	G1-BF-1	-131	-177	46	26%	-213	-202	10	5%
Compression	G1-BF-2	-222				-192			
Compression	G2-BF-1	-196	-188	8	4%	-296	-175	120	69%
Compression	G2-BF-2	-180				-55			
Compression	G3-BF-1	-226	-210	16	8%	NA			
Compression	G3-BF-2	-194							
Pass Average					19%				30%

		Pass 2 Day 1				Pass 2 Day2			
Action	Gauge Location	Field Test (psi)	Vertical bend.	Lateral bend.	% Lat/Ver	Field Test (psi)	Vertical bend.	Lateral bend.	% Lat/Ver
Tension	G1-BF-1	259	171	88	51%	206	173	32	19%
Tension	G1-BF-2	83				141			
Tension	G2-BF-1	206	164	42	26%	287	186	101	54%
Tension	G2-BF-2	121				85			
Tension	G3-BF-1	853	792	61	8%	NA			
Tension	G3-BF-2	731							
Compression	G1-BF-1	-117	-140	23	16%	-146	-130	16	13%
Compression	G1-BF-2	-163				-114			
Compression	G2-BF-1	-148	-127	21	17%	-168	-122	46	38%
Compression	G2-BF-2	-105				-76			
Compression	G3-BF-1	-75	-56	19	33%	NA			
Compression	G3-BF-2	-38							
Pass Average					25%				31%

Table 5.13 Vertical and Lateral Bending Stresses (psi) For Bottom Flange, SR-299, FEA Results

		Pass 1 Day 1				Pass 1 Day 2			
Action	Gauge Location	FEA	Vertical bend.	Lateral bend.	% Lat/Ver	FEA	Vertical bend.	Lateral bend.	% Lat/Ver
Tension	G1-BF-1	503	1875	1372	73%	564	1672	1108	66%
Tension	G1-BF-2	3247				2780			
Tension	G2-BF-1	2161	1957	204	10%	2128	1791	337	19%
Tension	G2-BF-2	1752				1454			
Tension	G3-BF-1	60	48	11	24%	NA			
Tension	G3-BF-2	37							
Compression	G1-BF-1	-255	-254	-1	0%	-152	-204	52	25%
Compression	G1-BF-2	-253				-256			
Compression	G2-BF-1	-219	-196	-23	12%	-184	-192	8	4%
Compression	G2-BF-2	-173				-200			
Compression	G3-BF-1	-86	-47	-39	82%				
Compression	G3-BF-2	-9							
Pass Average					34%				29%

		Pass 2 Day 1				Pass 2 Day2			
Action	Gauge Location	FEA	Vertical bend.	Lateral bend.	% Lat/Ver	FEA	Vertical bend.	Lateral bend.	% Lat/Ver
Tension	G1-BF-1	313	155	158	101%	453	159	294	185%
Tension	G1-BF-2	-2				-135			
Tension	G2-BF-1	374	156	218	140%	359	148	211	143%
Tension	G2-BF-2	-62				-63			
Tension	G3-BF-1	1744	1661	83	5%	NA			
Tension	G3-BF-2	1577							
Compression	G1-BF-1	-98	-100	2	-2%	-162	127	289	227%
Compression	G1-BF-2	-102				417			
Compression	G2-BF-1	-104	-91	13	14%	-102	-90	13	14%
Compression	G2-BF-2	-79				-77			
Compression	G3-BF-1	-83	-74	9	12%				
Compression	G3-BF-2	-65							
Pass Average					46%				142%

Table 5.14 Maximum Web Stresses, SR-299, Pass 1

		Day 1			Day 2		
Gauge Location	**Action**	**Field Test (psi)**	**FEA (psi)**	**% error**	**Field Test (psi)**	**FEA (psi)**	**% error**
G1-W-1	Tension	NA			827	850	-3%
G1-W-2	Tension				181	783	-332%
G1-W-AVG	Tension				504	816	-62%
G2-W-1	Tension				1009	981	3%
G2-W-2	Tension				383	881	-130%
G2-W-AVG	Tension				696	931	-34%
G3-W-1	Tension	63	18	72%	NA		
G3-W-2	Tension	40	6	85%			
G3-W-AVG	Tension	51	12	77%			
Average	Tension			79%			-116%
G1-W-1	Compression	NA			-158	-103	35%
G1-W-2	Compression				-92	-103	-12%
G1-W-AVG	Compression				-125	-103	18%
G2-W-1	Compression				-193	-102	47%
G2-W-2	Compression				-173	-102	41%
G2-W-AVG	Compression				-183	-102	44%
G3-W-1	Compression	-168	-22	87%	NA		
G3-W-2	Compression	-179	-22	88%			
G3-W-AVG	Compression	-173	-22	88%			
Average	Compression			88%			28%

Table 5.15 Maximum Web Stresses, SR-299, Pass 2

		Day 1			Day 2		
Gauge Location	Action	Field Test (psi)	FEA (psi)	% error	Field Test (psi)	FEA (psi)	% error
G1-W-1	Tension	NA			125	80	37%
G1-W-2	Tension				33	53	-61%
G1-W-AVG	Tension				79	67	16%
G2-W-1	Tension				168	80	52%
G2-W-2	Tension				-30	77	359%
G2-W-AVG	Tension				69	78	-13%
G3-W-1	Tension	489	856	43%	NA		
G3-W-2	Tension	407	723	44%			
G3-W-AVG	Tension	448	790	43%			
Average	Tension			44%			97%
G1-W-1	Compression	NA			-92	-52	44%
G1-W-2	Compression				0	-46	100%
G1-W-AVG	Compression				-46	-49	-6%
G2-W-1	Compression				-112	-71	37%
G2-W-2	Compression				21	-69	431%
G2-W-AVG	Compression				-46	-70	-54%
G3-W-1	Compression	-66	-40	39%	NA		
G3-W-2	Compression	-63	-40	36%			
G3-W-AVG	Compression	-65	-40	38%			
Average	Compression			38%			153%

is concurrent to the peak compressive stress (112 psi) at gauge pair G2-W, the value of 21 psi was used for comparison with FEA results. Thus, the cumulative effect of inconsistent field data and small magnitudes of stress contribute to the high percent error at this gauge. The worst correlation in tension (359%) was at the same gauge location and pass.

The neutral axis (NA) locations implied by the web stress data discussed above and the flange stress data discussed in the previous section from the field and FEA data, along with the theoretical NA positions, are shown in Table 5.16 and Figure 5.30. All data shown here are locations relative to the bottom of the bottom flange, which can be considered relative to a web depth of 54 in., a steel girder depth of 56.0 to 58.5 in., and

a total composite cross-section depth of 67.50 to 69.25 in. Theoretical values for the neutral axis position were calculated separately assuming both 4 ksi and 5 ksi strength concrete, although as shown in the table, the results are not especially sensitive to this variation.

The theoretical calculations predict a NA position between 46 and 48 inches. This is achieved for one of the six combinations of cross-section and loading in the FEA (G3 Pass 2) and the FEA NA positions for all girder cross-sections when the load is placed to maximize the moment in that cross-section (i.e., Pass 1 for G1 and G2 and Pass 2 for G3) are within 10% of the lower-bound theoretical prediction and all FEA data is within 20% of the theoretical NA position. Larger variations are observed in the field results, both in terms of variation within the field NA positions and the variation between these values and either the theoretical or FEA positions. The most consistent results are obtained at G1, where the field results are within 10% of one another for the two passes and the field and FEA results are within 10% of one another for each corresponding pass. Interestingly, at this cross-section, both the field and FEA results show the NA position lowering as the loading moves farther from the point of evaluation in Pass 2 versus Pass 1. Good correlation (11% difference) is also obtained between G2 field data for Pass 2 and the FEA and theoretical results at this cross-section. The field data for gauge location G3 for Pass 1 produces neutral axis values much higher than theoretically expected and in the case of G3 Pass 1 does not even produce a neutral axis location physically located anywhere on the 67.5 in. deep composite cross-section.

When the NA locations for both bridges are compared some similarities are noticed. The largest percent difference in neutral axis locations for US-13 was 32%, while the largest percent difference for SR-299 was 47%; both of these differences

Table 5.16 Neutral Axis Calculation for SR-299

Gauge Location	Field Test NA Estimates (in)		FEA NA Estimates (in)		Theoretical NA Values (in)	
	Pass 1	Pass 2	Pass 1	Pass 2	4 ksi	5 ksi
G1	48.5	44.8	45.2	41.1	46.5	47.6
G2	62.0	42.4	42.7	38.2	46.5	47.6
G3	90.3*	59.1	43.4	46.3	46.5	47.6

*Exceeds depth of cross-section.

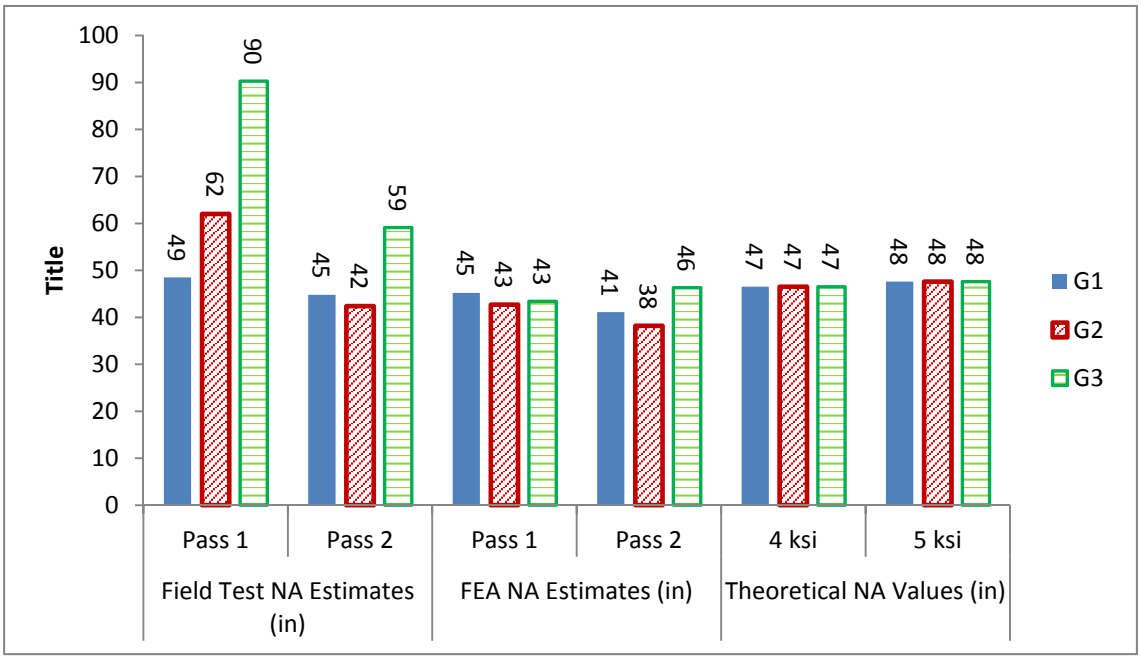

Figure 5.30 Neutral Axis Locations for SR-299: Field Tests, FEA, and Theoretical

occur at the cross-sections closest to the abutments (G3 for SR-299 and G1 for US-13). An additional similarity is that in both bridges, there are combinations of load passes and cross-sections that produce extrapolated neutral axis positions that are not located on the composite girder cross-section. One possible reason why the neutral axis is calculated above the total depth of the composite girders is that the girders are subjected to tensile axial loads. However, the supports at each abutment consist of expansion bearings designed to allow the girder to axially deflect so further field evaluation would

be necessary to evaluate whether this is a logical possible explanation for the observed data. A second possible reason could be that the web and bottom flanges are subjected to un-symmetric warping stresses. For example, the restraint provided by the concrete deck, prevents out-of-plane deflection of the top flange to a greater extent than the bottom flange is restrained. This type of distortion could increase the bottom flange stresses more so than the web stresses, producing a higher neutral axis position than what would be calculated assuming vertical bending and symmetric lateral bending.

5.3.2.2 **Cross-frame Results for SR-299**

As previously discussed in Chapter 4, strain gauges were placed on cross-frames close to mid-span (12-4 and 12-5), at the pier (8-4) and close to the obtuse corner of the bridge (14-8, 14-9 and 14-10). Tables 5.16 through 5.19 list the maximum recorded tensile and compressive stress values for the field and FEA results for each of the four passes of the load vehicle, respectively. The percent errors reported here are computed relative to the field test results as was done in previous presentations of this type of data. Figures 5.31 through 5.34 report the same stress data graphically and demonstrate that despite rather high percent differences, the FEA is reasonably accurate at capturing the general trends observed in the field results. Three cases were excluded from the tables because of irregularities and excessive noise in the data signal.

The highest cross-frame stress for this structure was a tensile stress of 1560 psi during the field test at 12-4-B during Pass 1 Day 2. The highest compressive stress (1365 psi, see Figure 5.32) was measured during the field test at 12-5-A during the same pass. These two gauges where highest tensile and compressive stresses were

Table 5.17 Cross-frame Maximum Stresses, SR-299, Pass 1 Day 1

	Tension			Compression		
Gauge Location	Field data (psi)	FEA (psi)	% error	Field data (psi)	FEA (psi)	% error
14-8-B	33	0	100%	-243	-165	32%
14-8-D	45	0	100%	-216	-165	24%
14-8-H	55	44	19%	-410	-190	54%
14-8-G	38	44	-15%	-244	-190	22%
14-9-B	12	1	95%	-217	-135	38%
14-9-D	11	1	94%	-195	-135	31%
14-9-H	74	38	49%	-173	-99	43%
14-9-G	72	38	47%	-212	-99	53%
14-9-E	70	36	48%	-482	-253	48%
14-10-A	162	128	21%	-19	-23	-25%
14-10-C	145	157	-8%	-3	-23	-705%
14-10-F	63	36	43%	-238	-253	-6%
14-10-E	51	36	31%	-285	-253	11%

Table 5.18 Cross-frame Maximum Stresses, SR-299, Pass 1 Day 2

	Tension			Compression		
Gauge Location	Field data (psi)	FEA (psi)	% error	Field data (psi)	FEA (psi)	% error
8-4-B	258	396	-53%	-303	-410	-35%
8-4-D	141	396	-181%	-212	-410	-93%
8-4-H	210	212	-1%	-	-212	-
8-4-G	153	212	-39%	-	-212	-
12-4-B	1560	470	70%	-79	-4	95%
12-4-D	1450	470	68%	0	-4	100%
12-4-H	1395	834	40%	-205	-29	86%
12-4-G	1320	834	37%	-210	-29	86%
12-5-A	80	19	76%	-1366	-1016	26%
12-5-C	70	19	73%	-1125	-1016	10%
12-5-F	1233	925	25%	-15	-38	-153%
12-5-E	1482	925	38%	-28	-38	-36%

Table 5.19 Cross-frame Maximum Stresses, SR-299, Pass 2 Day 1

	Tension			Compression		
Gauge Location	Field data (psi)	FEA (psi)	% error	Field data (psi)	FEA (psi)	% error
14-8-B	44	0	100%	-914	-514	44%
14-8-D	63	0	100%	-705	-514	27%
14-8-H	1438	603	58%	-72	-41	43%
14-8-G	1227	603	51%	-70	-41	41%
14-9-B	699	204	71%	-52	-17	67%
14-9-D	635	204	68%	-45	-17	62%
14-9-H	847	587	31%	-45	-27	40%
14-9-G	945	587	38%	-59	-27	54%
14-9-E	248	848	-242%	0	-47	100%
14-10-A	53	30	43%	-931	-935	0%
14-10-C	33	30	9%	-774	-935	-21%
14-10-F	1061	866	18%	-59	-35	41%
14-10-E	1198	866	28%	-79	-35	56%

Table 5.20 Cross-frame Maximum Stresses, SR-299, Pass 2 Day 2

	Tension			Compression		
Gauge Position	Field data (psi)	FEA (psi)	% error	Field data (psi)	FEA (psi)	% error
8-4-B	231	285	-23%	-345	-288	17%
8-4-D	113	285	-152%	-226	-288	-27%
8-4-H	210	187	11%	-17	-176	-935%
8-4-G	205	187	9%	-17	-176	-935%
12-4-B	51	98	-92%	-21	0	100%
12-4-D	39	98	-151%	-38	0	100%
12-4-H	125	0	100%	-313	-204	35%
12-4-G	130	0	100%	-280	-204	27%
12-5-A	48	3	94%	-115	-62	46%
12-5-C	52	3	94%	-108	-62	43%
12-5-F	-	0	-	-	-216	-
12-5-E	89	0	100%	-429	-216	50%

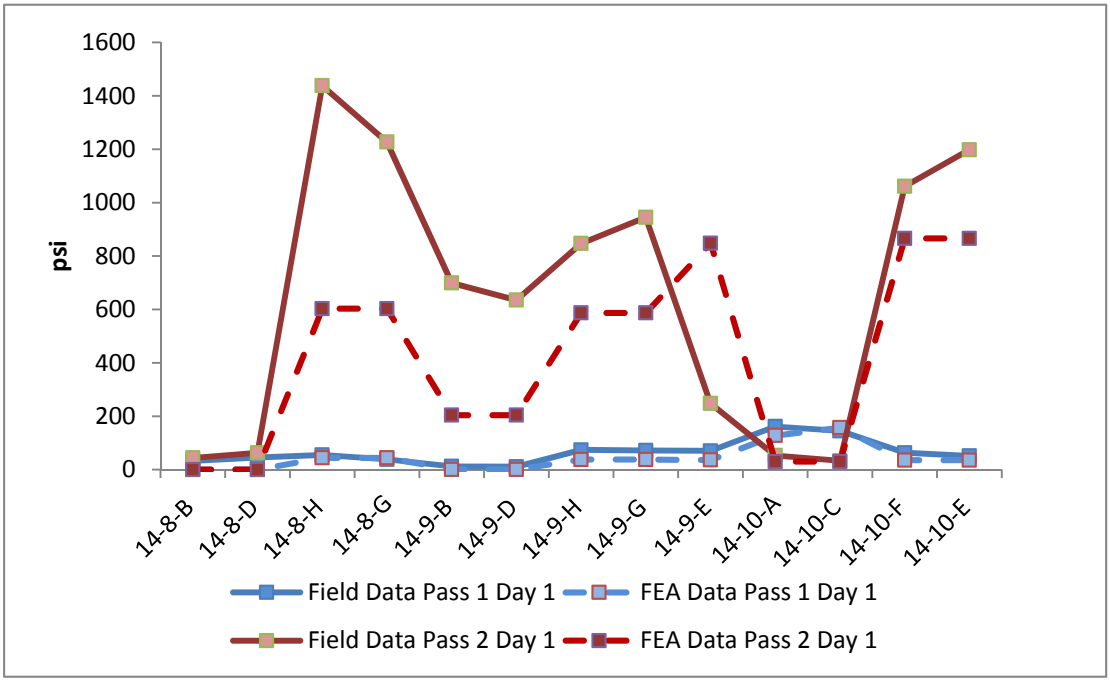

Figure 5.31Maximum Tensile Cross-frame Stresses, SR-299, Pass 1 Day 1 and Pass 2 Day 1

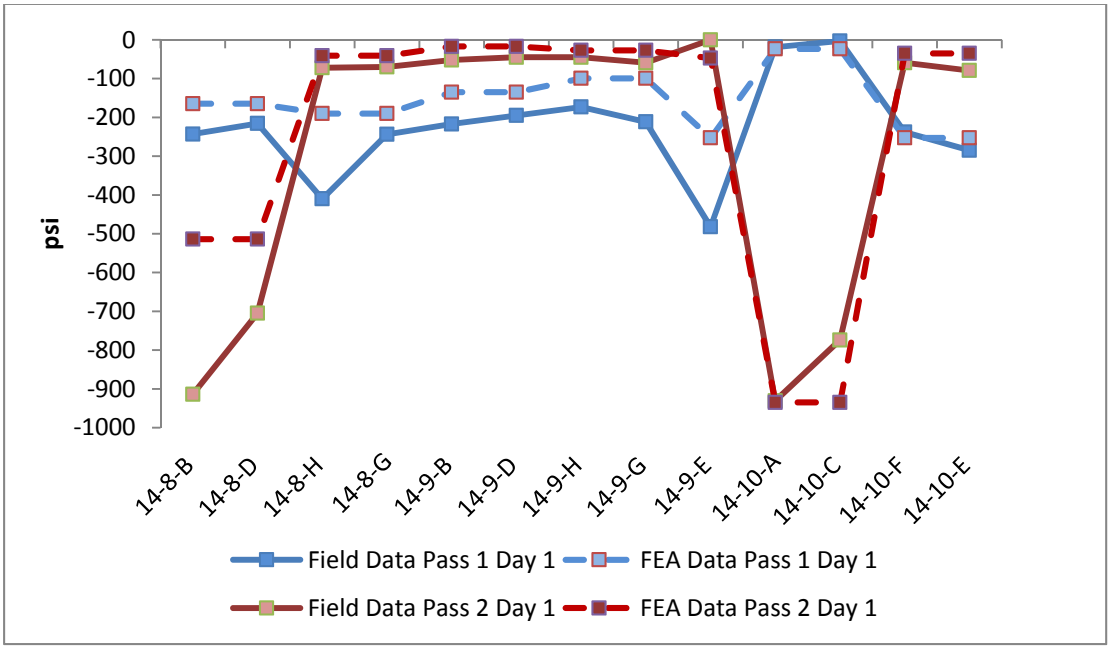

Figure 5.32 Maximum Compressive Cross-frame Stresses, SR-299, Pass 1 Day 1 and Pass 2 Day 1

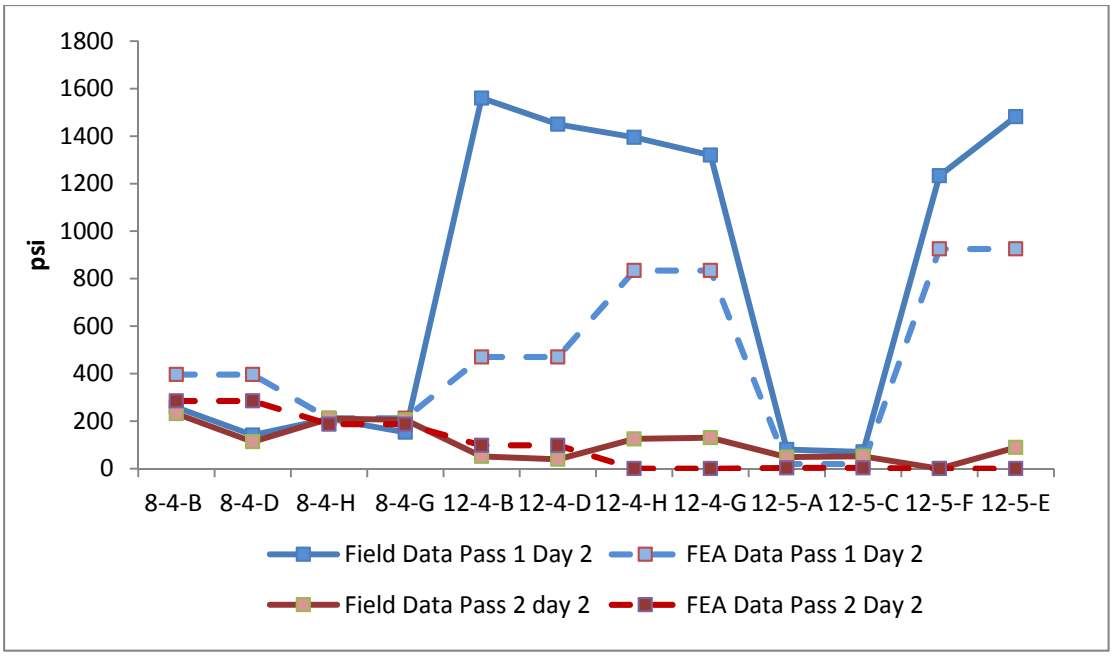

Figure 5.33 Maximum Tensile Cross-frame Stresses, SR-299, Pass 1 Day 2 and Pass 2 Day 2

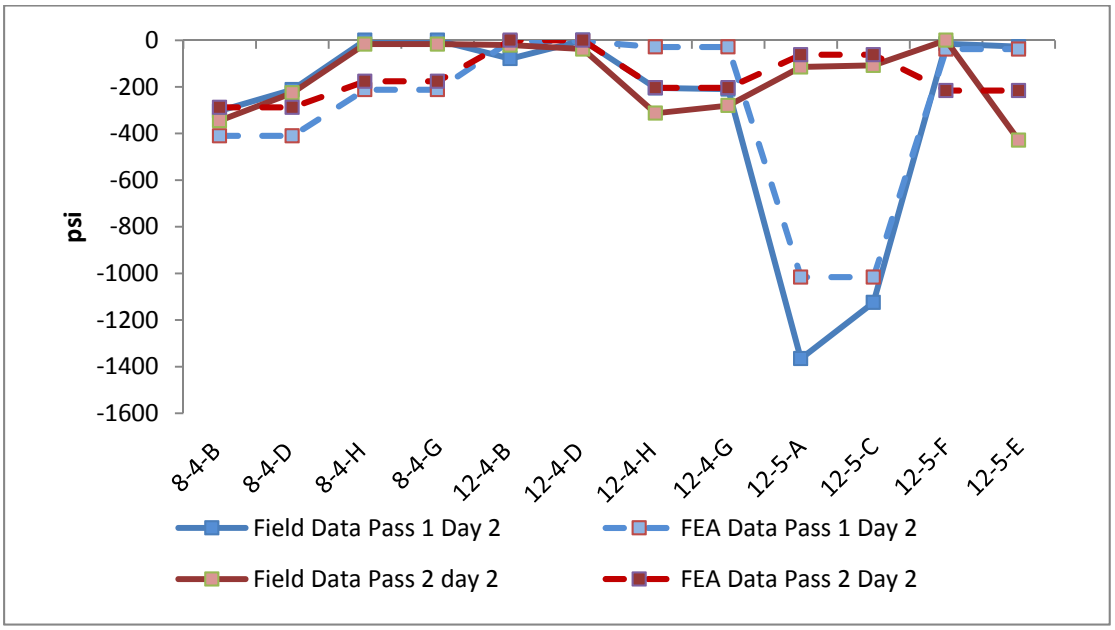

Figure 5.34 Maximum Compressive Cross-frame Stresses, SR-299, Pass 1 Day 2 and Pass 2 Day 2

recorded are located at the top end of opposing diagonals bracing opposite sides of Girder 5. The highest tensile stress obtained from the FEA (834 psi) was also recorded due to the same load pass and on the same cross-frame as in the field test, but at a different gauge location, 12-4-G. In contrast to the location of 12-4-B at the top of the cross-frame diagonal framing into Girder 5, 12-4-G is on the bottom chord, 3 in. towards Girder 5 from the gusset plate that connects the diagonals with the bottom chord. The FEA results for peak compressive cross-frame stress are more similar to the field results, where the highest FEA compressive stress (1016 psi, see Figure 5.32) was recorded at 12-5-A (the same gauge location as the field results), again during Pass 1 Day 2.

The best overall correlation between field measurements and FEA results was obtained at cross-frame location 14-10-A when Pass 2 Day 1 causes compression (the worst-case scenario for this location); the difference between measured and calculated stresses was 0%. The best correlation in tension (8%) was obtained on the same cross-frame at 14-10-C during Pass 1 Day 1 (see Figure 5.31). The location of Cross-frame 14-10 on which these most favorable correlations were achieved is close to the east obtuse corner of the bridge. Furthermore, these affected gauge locations (14-10-A and 14-10-C) are located on the same cross-frame diagonal, where Location A is at the end of the member framing into the girder and Location C is at the end of the member framing into the bottom chord of the K-frame. The general trend in the comparison between the FEA and field results was that the cross-frame field data display higher stresses than the FEA results (which are graphically illustrated in Figures 5.31 through 5.34). This is similar to the trend observed in the cross-frame stress data for US -13.

In comparing the magnitudes and associated locations of peak stress in the two bridges, recall that the maximum cross-frame stress (4218 psi) in US-13 was recorded at a gauge location close to the abutment (4-4-G). This peak stress measured at 4-4-G was 18% higher than the peak stress in any other instrumented location on another cross-

frame in the same bridge (3588 psi at 14-3-B). Furthermore, while the average tensile stresses at the instrumented locations of Cross-frame 4-4 do not vary significantly from the average tension stress recorded at other gauges, the compressive stresses in Cross-frame 4-4 is 2.6 times the average compressive stress at the remaining gauge locations. In contrast, the maximum stress in SR-299 (1560 psi) was measured near mid-span (in Gauge 12-4–B) and is 37% of the US-13 maximum recorded cross-frame (4-4-G) stress and 43% of the US-13 maximum recorded mid-span cross-frame stress (14-3-B). In comparing the peak stresses recorded near the abutments in the two structures, the maximum stress measured in cross-frames near the abutments in SR-299 (1198 psi at 14-10-E) is 28% of the maximum cross-frame stress measured in US-13.

FEA was also used to assess, and later confirm, that these general trends of higher cross-frame stress in US-13 were applicable when expanding the consideration to all possible cross-frame locations rather than only instrumented locations. Specifically, selected load cases (those producing the maximum force effects at the gauge locations) were reviewed and the maximum tensile and compressive cross-frame stresses occurring anywhere in the models were recorded. Comparing the peak overall cross-frame stresses (which occur adjacent to the abutment in US-13 and two lateral bracing spacings away from the obtuse corner of the abutment in SR-299) in the FEA of the two structures it is shown that the maximum value for SR-299 (1160 psi at 13-10-E and 13-10-F) is 35% of the maximum value for US-13 (3268 psi at 4-4-D). The US-13 FEA maximum occurs on the same diagonal on which the peak value was obtained from the subset of instrumented locations, at Gauge 4-4-G, and is only 3% larger than this value. The SR-299 13-10-E and 13-10-F maximums are 25% higher than peak stress measured at instrumented location 14-10-E (866 psi), which is in a corresponding location on the next bay of cross-frames closer to the abutment.

The FEA maximum cross-frame stress near mid-span in SR-299 was also significantly less (48%) than the corresponding US-13 value. Specifically, a stress of

1054 psi was recorded at location 13-5-D in SR-299 (which is only slightly larger than the peak stress at an instrumented mid-span cross-frame location of 1016 psi) compared to a stress of 2215 psi at location 14-2-F (which again is only slightly, 4%, larger than the peak stress at a corresponding instrumented location, 2215 psi at 14-3-B in the adjacent cross-frame. Thus, it is concluded that the instrumented locations are representative of general trends in the model and that regardless of whether cross-frame stresses of the two bridges are compared in terms of overall maximums or maximums at common locations, the peak stresses in US-13 are consistently significantly higher (more than double in all cases). This trend is most significant at the abutments where the peak US-13 stresses are nearly four times the corresponding SR-299 stresses.

The key differences between the two bridges that are likely causes of these observed differences in cross-frame stress magnitudes are skew angle and cross-frame configuration. Compared to Bridge US-13, Bridge SR-299 has a smaller skew angle. It also differs in that it has a staggered cross-frame configuration while US-13 has inline cross-frames. Results show that cross-frames at bridge US-13 are exposed to higher stresses than cross-frames at bridge SR-299, while being subjected to the same loadings. Based on the known relationship between skew and torsional force, the higher skew of US-13 is a likely reason for the increased cross-frame stresses (independent of loading and girder geometry) in this bridge.

It is also noted that these differences in cross-frame stresses are not strongly related to variations in girder dimensions or stress. The maximum bottom flange stress (1475 psi) measured in US-13 near mid-span (at G3-BF-1) is 15 % smaller than the maximum bottom flange stress (1749 psi) measured near mid-span in SR-299 (at G2-BF-1). In contrast, the maximum bottom flange stress near the abutment in US-13 (1180 psi at G1-BF-1) is 28% higher than the maximum bottom flange stress at a corresponding location in SR-299 (853 psi at G3-BF-1). As with the cross-frame results, FEA was again used to assess where the comparison of instrumented locations was

representative of general trends. For the selected load cases evaluated, to which these results may be sensitive, it is shown that greater stress occurs in SR-299, 4385 psi versus 3286 psi in US-13. (The location of maximum bottom flange stress in US-13 is at the north end of Girder 2, 4.5 feet from the abutment, on the west edge of the bottom flange. The location of maximum bottom flange stress in SR-299 is at the south edge of Girder 4, 44 ft. from the east abutment.) Thus, these variations in girder stress are small considered relative to the fact that the cross-frame stresses in US-13 are more than double those observed in SR-299. This same trend applies when the average stresses at gauge pairs are compared. The peak average stress of a bottom flange gauge pair near mid-span at US-13 (1353 psi) is only 9 % larger than the corresponding value at mid-span at SR-299 (1234 psi); the peak average stress of a bottom flange gauge pair near the abutment in US-13 (1096 psi) represents the largest difference at corresponding locations between the two bridges, being 41 % larger than the corresponding value near the abutment in SR-299 (792 psi), which is still significantly less than the differences in cross-frame stress.

A stress distribution trend throughout the cross-frame members was detected while analyzing cross-frame field measurements for SR-299 that was not detected in the cross-frames of US-13. Table 5.20 summarizes these results, where during Pass 1 Day 2, which is the pass that theoretically should produce the highest stresses at mid-span, the maximum cross-frame stress (1560 psi) was measured at 12-4-B, while at the same time, the stress at the adjacent gauge location on the other side of the same girder (12-5-A, see Figure 5.35) was only 80 psi. When analyzing cross-frames near the abutment, similar behavior was detected; the stress recorded at 14-9-B was 699 psi while the stress at the adjacent gauge location on the other side of the girder (14-8-B, see Figure 5.35) was 44 psi. Similarly, the stress on the other side of 14-9, in 14-10-A (see Figure 5.35) was 53 psi. A different behavior is seen in the bottom chord stresses at cross-frames near the abutment, where peak cross-frame stresses during Pass 2 were recorded.

Specifically, bottom chord stresses in 14-8-H (which experiences the highest stress under Pass 1) and 14-10-E were significantly increased (by 70% and 41%, respectively) when compared to bottom chord stress reported at 14-9-H, which is at the instrumented end of the bottom chord between Cross-frames 14-8 and 14-10, with higher stresses recorded at the cross-frame two girders removed from the east obtuse corner of the bridge(14-8-H, see Fig. 5.35). The adjacent bottom chord stresses near mid-span at locations 12-4-H and 12-5-E (shown in Fig. 5.34) are more consistent with one another, differing by only 6%.

A final note on the behavior of SR-299, particularly in contrast to US-13, is that because SR-299 has a staggered cross-frame configuration, unbalanced cross-frame forces will create additional lateral bending in the bottom flange. This is depicted by Figure 5.36, which shows an example view of the bottom flange, stiffener, and cross-frame FEA mesh with the directions of cross-frame centroidal stresses when equilibrium is reached. These force effects will create additional stresses in cross-frame members, and thus a process synonymous with a loop that repeats until equilibrium is reached.

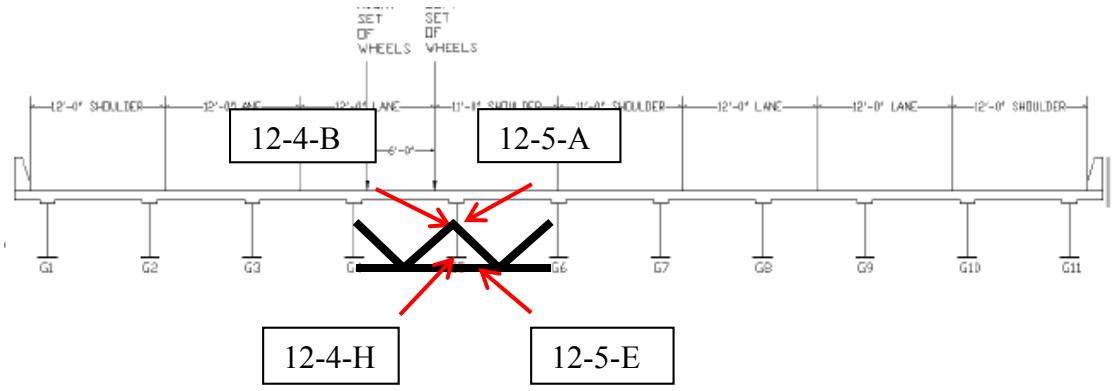

Figure 5.34 Adjacent Cross-frame Gauges of Interest during Pass 1, SR-299

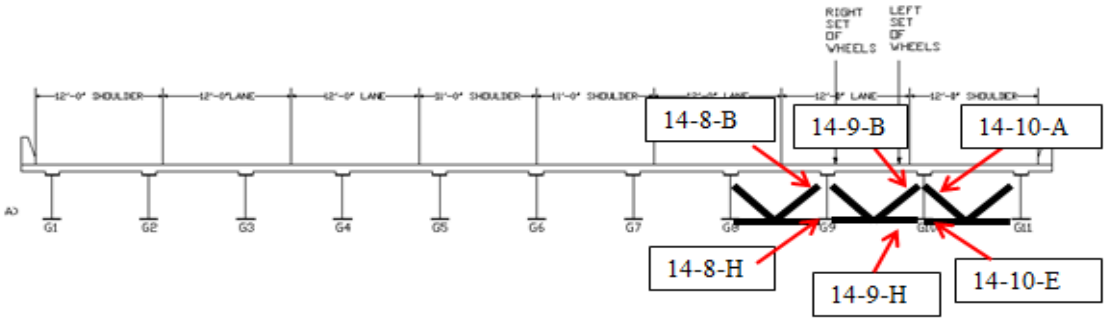

Figure 5.35 Adjacent Cross–frame Gauges of Interest during Pass 2, SR-299

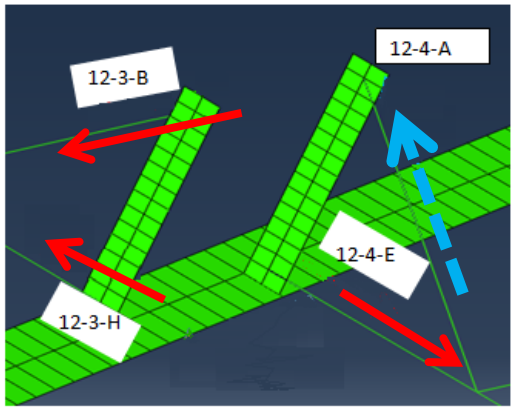

Figure 5.36 Direction of Cross-frame Forces at Equilibrium, SR-299. Blue Arrow (Dashed) Represents Compressive Forces, Red Arrow (Solid) Represents Tensile Forces

Table 5.21 Concurrent Stresses in Adjacent Cross-frames (psi)

	Peak Stress		**Concurrent Stress**	
Mid-span Diagonal Member Gauges	**12-4-B**	1560	**12-5-A**	80
Mid-span Bottom Chord Gauges	**12-5-E**	1482	**12-4-H**	1395

	Peak Stress		**Concurrent Stresses**			
Abutment Diagonal Member Gauges	**14-8-B**	44	**14-9-B**	699	**14-10-A**	53
Abutment Bottom Chord Gauges	**14-8-H**	1438	**14-9-H**	847	**14-10-E**	1198

5.4 **Conclusion**

This chapter has reviewed the results from the field testing in comparison to the corresponding FEA data for the purpose of validating the FEA modeling techniques and discussed the structural behavior implied by these results. The FEA validation efforts show that the FEA accuracy is very sensitive to the manner in which the cross-frames are modeled. The primary FEA study was based on modeling cross-frame members with beam elements. Accurate FEA results were obtained in only some cases when using this approach, with only the bottom flange results for US-13 providing generally reliable data. Much improved accuracy resulted when refined modeling of the cross-frame members was applied, which included: using shell elements for these members as opposed to beam elements, more accurately modeling the connections between the cross-frames and the remainder of the structure, and including cross-frame gusset plates in the models when applicable.

The raw data from the field results was also used to evaluate the extent of lateral bending in the girders, calculate neutral axis positions, and compare magnitudes and locations of peak stress. These results show that the more highly skewed structure experiences significantly greater stresses in the cross-frame members while there is no significant difference in peak girder stresses. Additional variables between the two bridges are the cross-frame configuration and layout, which will be further examined in the next chapter. The results also reveal some deviations between the field response and theoretical expectations that may be due to differences in the intended and actual fixities of the supports, warping of the girder cross-sections, or both.

Chapter 6

PARAMETRIC ANALYSIS

This chapter discusses the results of a parametric study aimed at evaluating the influences of cross-frame configuration (referring to x- or k-frames) and cross-frame layout (referring to inline or staggered cross-frames on the elastic and inelastic response of a representative structure. Section 6.1 provides a more detailed introduction to this work. Section 6.2 then provides a description of the data analysis methodology used in the parametric analysis. Section 6.3 presents linear-elastic analysis results obtained from the application of a standard AASHTO HS-20 design vehicle moving across the bridge in the same transverse position as Pass 1 in the field testing described in Chapter 4. Section 6.4 presents non-linear results obtained from using the Riks method of analysis (described in Section 3.7) in an effort to compare the ultimate capacities of bridges with different cross-frame configurations and layouts. Lastly, Section 6.5 summarizes the results presented in this chapter.

6.1 Introduction

US-13 is used as the baseline model for this parametric study due to the improved correlation between the field and FEA results for this bridge and the reduced model size resulting from this narrower bridge. The fact that US-13 is the more highly-skewed bridge of the two evaluated has reason to both increase and decrease the bridge's system capacity. On one hand, Bechtel et al. (2009) have shown that high skew angles lead to greater system capacity as the skewed alignment causes significant differences in the magnitude of the moment in adjacent girders for any fixed position of loading. However, this work did not explicitly consider the cross-frames role in load distribution. On the other hand, it is known that bridges with higher skew, and the cross-frames within these bridges, tend to experience additional torsional loads (White, 2012).

These facts should be considered when forming general conclusions based on this work. Furthermore, Pass 1 from the field test was selected as the basis for the applied loading based on the results presented in Chapter 5 that this load path produced the best correlations between the field and FEA results.

It is known that placing cross-frames in discontinuous lines will reduce the transverse stiffness of the bridge. This will cause a decrease in cross-frame forces, but increase in flange lateral bending stress for the reasons discussed in Chapter 5. Additionally, it has been suggested that the diagonal members of K-frames are exposed to significantly lower stresses than the diagonal members of X-frames, suggesting that cross-frame configuration may play a role in increasing or decreasing system reserve capacity (Steel Bridge Design Handbook-Bracing System Design, 2012). The data reviewed in Chapter 5 confirms this is true for the bridges field tested in this work. Therefore, it was hypothesized that varying cross-frame configuration and layout may affect bridge behavior at elastic levels of loading as well as ultimate system capacity.

US-13 was used as the base model for the parametric study with all bridge models having identical overall bridge geometry and primary structural elements, including the girders, deck, haunch, parapet and supports. All combinations of two different cross-frame configurations (X-frame and K-frame) and two different layouts (inline and staggered) were then evaluated to form a set of four models in the parametric study. This base model was label X-frame Inline, meaning that the cross-frame configuration is X-frame and cross-frame layout is inline. The second model was labeled X-frame Staggered, meaning that the configuration was kept the same (X-frame) but the cross-frame layout was staggered. The third model was labeled K-frame Inline, which means that the cross-frame configuration was K-frame and the cross-frame layout was inline. And lastly, the fourth model was labeled K-frame Staggered, which means that the cross-frame configuration was K-frame and the cross-frame layout was staggered.

The configuration of the X-frames was exactly as exists in the actual US-13 structure, which was detailed in Chapter 2. The configuration and member sizes of the K-frames were exactly as in the actual SR-299 structure, which was also detailed in Chapter 2. However, the length of the K-frames was increased from 8.5 ft. to 8.75 ft. given the difference in girder spacings of the two bridges. Also, the depth of the K-frame was increased from 3.2 ft. to 4.8 ft. due to the change in girder depth of the two structures (such that the projections of the diagonals of the new K–frames coincide with top flange and web intersection). It is noted that these increased lengths would result in decreasing these members' compression capacities.

The location of the inline cross-frames (left side of Figure 6.1), which are placed perpendicular to the girders, also reflect the cross-frame layout used in the actual structure. Staggered cross-frames, which are also oriented perpendicular to the girders, are offset from each other (as shown on the right side of Figure 6.1) by 3.5 ft. on each side of a given girder. The stagger distance was determined based on two criteria. The first criterion was to keep the cross-frame spacing the same as it was in the original (X-frame inline) model to the extent possible and to not exceed this spacing, particularly in the negative bending regions over the pier so the girder lateral torsional buckling capacity is not decreased. The second criterion was that the first lateral bracing spacing from the abutment is placed so that the opposite end of the lateral brace intersects the adjacent girder at the abutment. It was found that an offset distance of 3.5ft satisfied both of these criteria while also having a practical value and was thus used in the study.

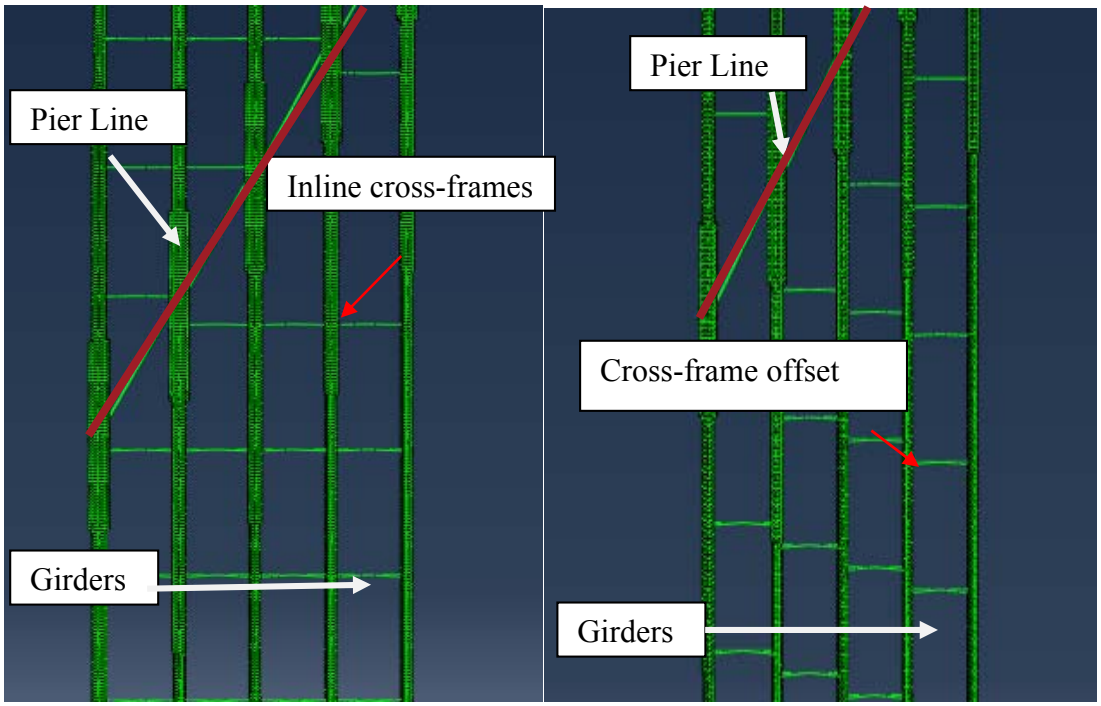

Figure 6.1 Inline (left) and Staggered (right) Cross-frame Layout used in Parametric Analysis

6.2 Data Analysis Metrics

This section discusses the data analysis metrics used in later sections of this chapter to inform the influence of cross-frame configuration and layout on structural performance. First, Section 6.2.1 discusses the data used to assess the linear-elastic behavior of the four parametric models, while Section 6.2.2 discusses the data analysis used when assessing the post-elastic response of the parametric models.

6.2.1 Linear-Elastic Analysis

For the linear-elastic analyses, the data extraction procedure was identical to the procedure used in Chapter 5 except that a more holistic view of the structure is considered, beyond evaluating only the instrumented locations. The maximum compressive and tensile stresses occurring anywhere in the bottom flange of the girders

and cross-frames along with the locations of these peak stresses as a vehicle traveling across the structure was simulated were extracted. Furthermore, the applied loading differs by applying self-weight of all members in addition to the live loading. This difference in loading was used because the force effects of this scenario are more informative for assessing the cross-frame stress output relative to strength capacities, which is also discussed herein. This is in contrast to the live load only scenario that was applied in the previous chapter, which was more appropriate for the stated goals of that work because only live load force effects were captured by the field instrumentation.

6.2.2 **Nonlinear-Plastic Analysis - Methodology**

The comparison of the inelastic response of different cross-frame configurations and layouts begins with comparing the maximum loading achieved in the analysis of each parametric model. This is quantified by the maximum load proportionality factors (LPF) achieved in each FEA, where LPF are multiples of the applied loading used in the field work that are resisted at each increment in the analysis as the displacement is gradually increased, provided equilibrium can be achieved when doing so. Thus, in the analysis output of this work, the LPF corresponds to the number of these vehicles that the bridges could theoretically support (for the analysis assumptions used here) when these trucks are co-located (i.e., stacked on top of one another). If equilibrium is achieved throughout the analysis, the maximum LPF is a measure a system capacity of the structure. If equilibrium is not achieved throughout the analysis (the solution is not converging), the LPF represents the highest level of loading that the FEM of the structure can be guaranteed to resist, but it is unknown to what extent, if any, loads higher than this loading could be resisted. This latter situation occurred for all four of the parametric FEM. Thus, the LPF at the final increment at which equilibrium was achieved were recorded for all four models. Then the lowest of these final LPF (which

equaled 57) from the four models was selected as a common loading used to compare the structural response of the four models at a common loading

In order to help designers to better understand the results from this analysis, the total magnitude of the applied loading is expressed in terms of an equivalent quantity of HS-20 design vehicles in the data analysis in Section 6.4. Specifically, when results are expressed in terms of a number of HS-20 design vehicles, this is based on multiplying the LPF from the analysis by the ratio of 55.1 kips of applied load to the HS-20 magnitude of 72 kip load. However, it is noted that the axle spacings of the test truck and design vehicle differ, so the HS-20 magnitudes should only be interpreted as an approximation.

The extent of yielding at this common level of loading was then assessed by counting the number of cross-frames that were yielded and calculating the total length of the bottom flanges that were both yielded and plastified. This is recorded at various loading levels, at LPF intervals of three to twenty (interval of two to fifteen HS-20 trucks) depending of the extent of the variation of the yielding. Cross-frames were considered yielded if any beam element constituting the cross-frame experienced a stress higher than the yield stress. The bottom flange is considered yielded at a given cross-section if the stress in any element within that cross-section exceeded the yield stress. The bottom flange is considered plastified if all elements comprising the bottom flange cross-section are yielded. For all elements the yield stress was considered to be 55 ksi based on the specified G50 material specification with a standard 10% over strength factor, a standard conservative assumption. The analysis of yielded elements was facilitated by using the Abaqus CAE post-processing program to view the output in a way that once the element von Mises stress exceeds the defined yield stress, the element is displayed in a different color (where red was used for cross-frame elements and white was used for the bottom flange elements).

The cross-frames response among the various models was compared by assessing the extent of yielding that is predicted in the cross-frames and the magnitudes of strain in the cross-frames. Specifically, as cross-frame elements yield, their location and the corresponding load magnitude was recorded. The peak cross-frame stains (tensile and compressive) and the location of the peak cross-frame strains were also extracted and compared among FEMs. Strain is used instead of stress for the cross-frames because the cross-frames cannot be modeled with non-linear material properties; thus, strain is the more practical output in this scenario.

The girder responses were assessed by evaluated yielding and plastification in the bottom flange. As bottom flange elements yield in previously un-yielded cross-sections, the length of these elements was added to the length of other yielded elements. If more than one element was yielded along the width of the bottom flange, only one element length was added to the yielded length calculation. Then the percent of the bottom flange that was yielded was computed. This was done by dividing the cumulative length of all yield bottom flange elements by the sum of the total linear feet of the girders in the north span of the bridge. The reason for using only one span in this calculation is that because the live load was placed on the north span of the bridge, there was a negligible effect on the bottom flanges and cross-frames in the south span of the bridge. Bottom flange plastification lengths are computed in the same way as yielded lengths, except that the plastification length criteria is that all elements along the width of the bottom flange must be yielded as illustrated by Figure 6.2. The final metric that was used in assessing the post-elastic behavior of the parametric models was the girder load distribution factors (GDF) at the final common increment of loading. The girder distribution factors (GDF) for each parametric model were calculated by dividing the bottom flange peak stress near mid-span by the sum of the bottom flange peak stress values in all girders at this same bridge cross-section. Mathematically, this can be expressed as GDFi of the ith girder and calculated by Equation 6-1.

$$GDF_i = \frac{\sigma_i}{\sum_{j=1}^{k} \sigma_j} \qquad \textit{Equation 6-1}$$

In this equation, σ_i is the peak stress in the bottom flange of Girder i at the selected cross-section and k is the number of girders. The left side of Figure 6.3 shows the mid-span location of the selected cross-section, which is 110 ft from the north abutment of Girder 5. This selection was made to better assess load distribution under peak positive vertical bending moments despite the fact that the highest bottom flange stress was recorded at the north end supports and pier. The stress contours in the figure on the right side of Figure 6.3 then indicates (via the dashed rectangle) the locations where bottom flange stresses were recorded for the calculation of GDFs and that this encompasses the peak stress in Girder 4 in this region of the bridge for the model shown here (K-frame Staggered).

These inelastic distribution factors were then compared with elastic distribution factors resulting from AASHTO design equations. However, the philosophy of the GDF values computed in this work differs from the behavior described by AASHTO distribution factors in two important ways. First, the stresses used in Equation 6-1 are

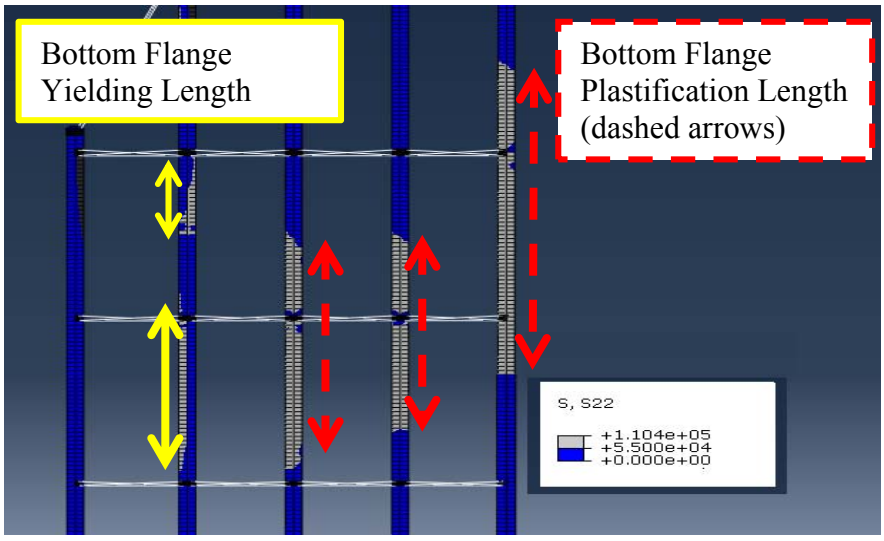

Figure 6.2 Bottom Flange Yielding (solid line) and Plastification (dashed line)

based on the total load applied in the model so they are representative of total load distribution, in contrast to the live load distribution factors calculated using AASHTO distribution factor equations. Second, by using peak stress rather than the peak average stress over the bottom flange cross-section, the effects of lateral bending are present in these results, in contrast to a typical live load distribution factor calculation that describes vertical bending effects only.

6.3 **Results of Linear Elastic Analysis**

Table 6.1 summarizes the cross-frame stress results obtained from the linear-elastic analysis under a moving HS-20 loading and Figure 6.3 reports these magnitudes graphically The locations listed in Table 6.1 refer to the cross-frame labelling conventions previously established in Chapter 4. This data shows that the maximum recorded compressive cross-frame stresses were higher than the corresponding tensile

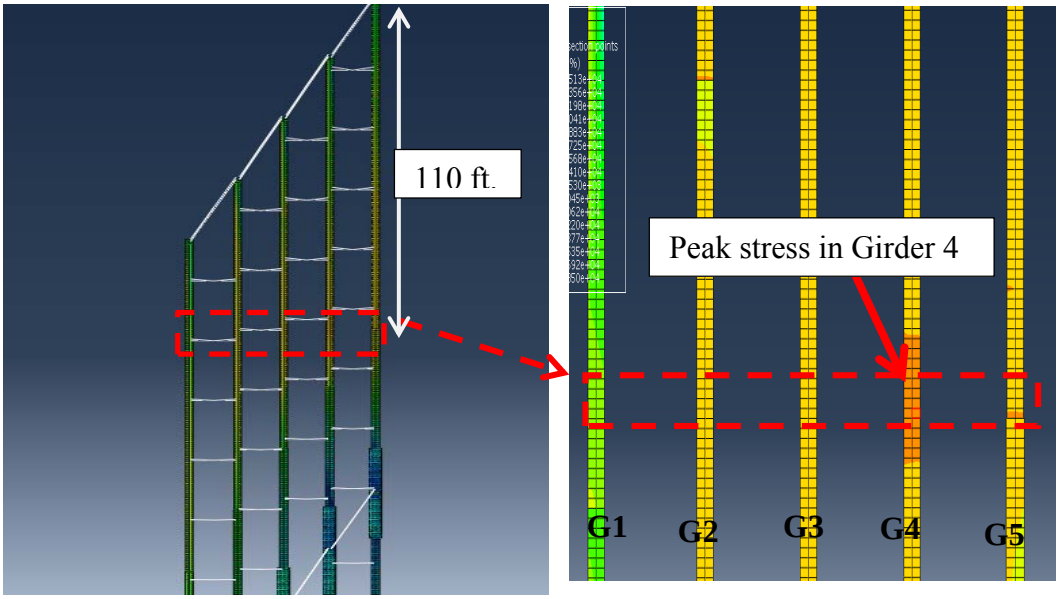

Figure 6.3 Visualization of Process for Determining Bottom Flange Stresses Used to Compute Girder Distribution Factors (GDF)

stresses in all models. The highest overall stress was 31.1 ksi of compression in the bottom chord of Cross-frame 12-4 in the K-frame staggered model. The highest tensile stress, of 17.2 ksi was recorded in the east diagonal of Cross-frame 4-4 in the X-frame inline model. This finding is opposite what it had been recorded in Chapter 5, where maximum cross-frame tensile stresses were higher than maximum compressive cross-frame stresses. The reason for this discrepancy may be due to the fact that in these parametric analyses the loading included both the HS-20 vehicle and the self-weight of the structural elements while the analyses in Chapter 5, simulating the data collected by the field instrumentation, contained only live load.

In comparing the magnitudes of cross-frame stresses predicted by the four models, there is no clear trend for the compression results. However, the tensile results show that the greater transverse stiffness of the inline cross-frames does contribute to greater stresses in these members, as would be expected. The locations of maximum cross-frame stresses in all models are in cross-frames adjacent to either the pier support or an abutment. Specifically, the location of maximum cross-frame stress in both tension and compression in the X-frame Inline model was at the south obtuse corner of the bridge (in opposing diagonals of Cross-frame 4-4). In all other models, the maximum compressive and tensile stresses occur in various cross-frames adjacent to the pier.

In order to better understand the significance of the magnitude of the stresses developed in these cross-frames, tensile and compressive capacities of cross-frame members were computed. Tensile capacities of the L3½ x 3½ x ⅜ and L4 x 4 x ½ cross-frame members were calculated based on both the yielding and fracture limit states. The fracture stress was calculated using Equation 6-2,

$$f_{t\_f} = \phi \cdot U \cdot f_u \qquad \textit{Equation 6-2}$$

where: f_{t_f} is tensile stress capacity of the cross-frame member based on the fracture limit state; ϕ is the resistance factor for tension net rupture, which is equal to 0.75; U is the shear lag factor; and f_u is the assumed ultimate stress of steel, which is assumed to closely mimic the properties of Grade 50 steel and is thus assigned a value of 65 ksi. The shear lag factor is calculated by Equation 6-3,

$$U = 1 - x/L \qquad \textit{Equation 6-3}$$

where: x is connection eccentricity and L is length of connection. Tensile capacity based on the yielding limit state (f_{t_y}) is calculated by Equation 6.4,

$$f_t = \phi \cdot f_y \qquad \textit{Equation 6-4}$$

where: $\boldsymbol{\phi}$ is the resistance factor for yielding on the gross area ($\boldsymbol{\phi}$ =0.9) and $\boldsymbol{f_y}$ is the assumed yield stress of steel, which is again assumed to closely mimic the properties of Grade 50 steel and is thus assigned a value of $\boldsymbol{f_y}$=50 ksi. The contrast between using minimum assumed properties in these design checks versus statistically probable material strengths in the modeling input should be noted, although this difference does not affect the resulting comparison between applied stress and tensile stress capacity because it will be shown below that the tensile stresses are resisted elastically by a significant margin.

Table 6.2 summarizes the resulting tensile stress capacity (ft_f and ft_y) of the two sizes of cross-frame members as well as the minimum stress capacity of the two limit states (ft). Here it is shown that the tensile stress capacity for both sizes of cross-frame members is fairly close to one another (4% difference).Furthermore, the governing tensile capacity of the bottom chord members (39.2 ksi) is 2.3 times larger than largest demand in the bottom chord (17.1 ksi, in the K-frame inline model). Similarly, the governing tensile stress capacity of the diagonal members (40.6 ksi) is 2.4 times the largest demand experienced by these members (17.2 ksi). The results show

Table 6.1 Maximum Cross-frame Stresses due HS-20 Loading

Action	Model	Maximum Stress Value (ksi)	Location
Tension	X-FRAME INLINE	17.2	4-4 -East Diagonal
	X- FRAME STAGGERED	12.3	11-4 East Diagonal
	K-FRAME INLINE	17.1	9-2 Bottom Chord
	K-FRAME STAGGERED	14.4	12-4 East Diagonal
Compression	X-FRAME INLINE	20.6	4-4- Right Diagonal
	X-FRAME STAGGERED	27.4	10-3 West Diagonal
	K-FRAME INLINE	26.7	12-4 Bottom Chord
	K-FRAME STAGGERED	31.1	12-4 Bottom Chord

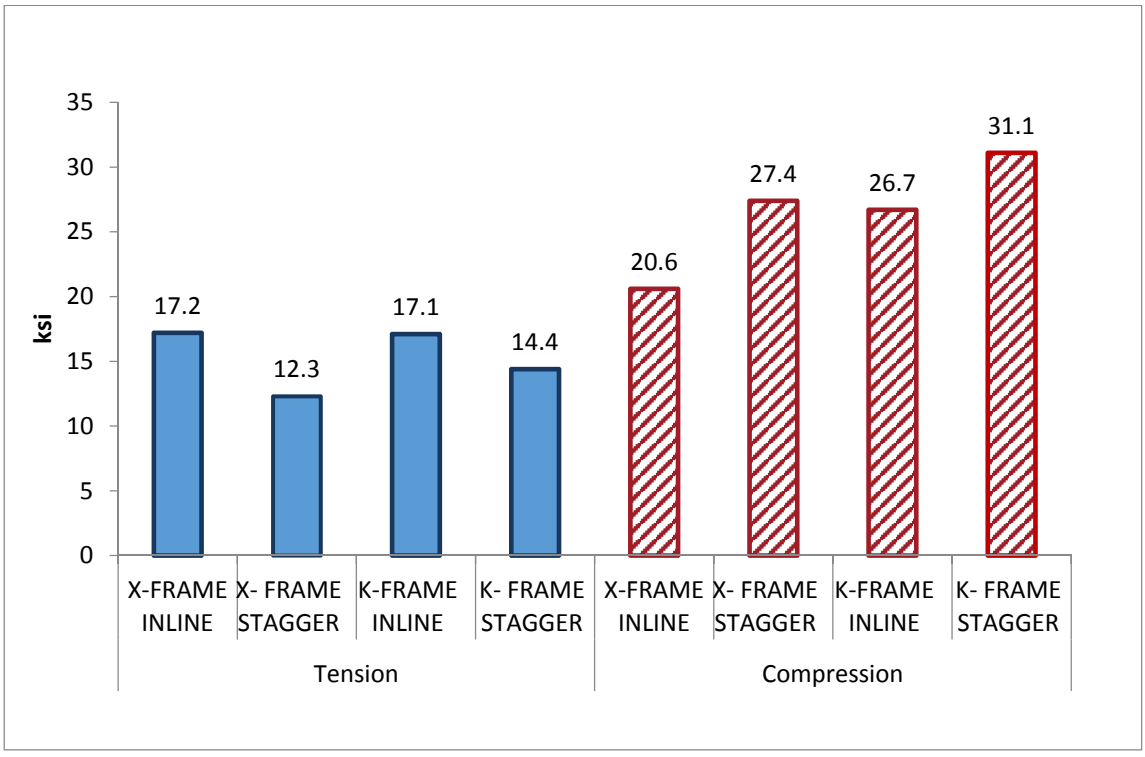

Figure 6.4 Maximum Cross-frame Stresses due to HS-20 Loading

that the cross-frame members can adequately resist the predicted tensile stresses, elastically resisting the tensile forces resulting from the applied loads.

To calculate compressive capacity of the cross-frame members, unbraced lengths for each member were first computed. The unbraced length of the bottom chord (L4 x 4 x ½) of X-frames is112 in. (which represents a slightly conservative estimate based on the center-to-center spacing of the girders less 1 in. clearance at each end of the member). In the K-frames, the connection plates connecting the mid-point of the bottom chord and the diagonals were considered a bracing point about all axes of the bottom chord such that the unbraced length of the bottom chord of K-frame members is half this length (56 in.). Similarly, the connection plate between the two diagonals of the X-frames is also considered a brace point about all axes of these members such that the unbraced length of the L3½ x 3½ x ⅜ members serving as diagonals in the X-frames is taken as 59 in. The unbraced length of the K-frame diagonal members is taken as 62 in. Article 4.6.2.5 AASHTO LRFD Bridge Design Specifications (2012) states that the effective-length factor, *k*, for trusses and frames with bolted or welded connections at both ends "may be taken as 0.750". This value is assumed to apply to the present situation.

Table 6.2 Tensile Capacity of Cross-frame Members

Member Location	Angle	x (in.)	L (in.)	U	f_{t_f} (ksi)	f_{t_y} (ksi)	f_t (ksi)
Diagonal	3½ x 3½ x ⅜	1.00	6.00	0.83	40.6	45	40.6
Bottom Chord	4 x 4 x ½	1.18	6.00	0.80	39.2	45	39.2

Compressive capacities of the cross-frame members is then calculated based on the following equation adapted from AISC (2008) Section 16,

$$f_c = \phi_c \cdot F_{cr} \qquad \textit{Equation 6-5}$$

where f_c is compressive stress capacity , ϕ_c is the resistance factor for axial compression equal to 0.9, and F_{cr} is the critical buckling stress. The critical buckling stress is determined as follows:

$$F_{cr} = Q\left(0.658^{Q\lambda_c^2}\right)F_y \quad \text{when} \quad \lambda_c\sqrt{Q} \leq 1.5 \qquad \textit{Equation 6-6}$$

and

$$F_{cr} = 0.877F_e \qquad \text{when} \quad \lambda_c\sqrt{Q} > 1.5 \qquad \textit{Equation 6-7}$$

where F_e is elastic critical buckling stress given by

$$F_e = \frac{\pi^2 E}{\left(\frac{KL}{r}\right)^2} \qquad \textit{Equation 6-8}$$

and

$$\lambda_c = \left(\frac{kl}{r\pi}\right)\sqrt{\frac{F_y}{E}} \qquad \textit{Equation 6-9}$$

In these equations, F_y is the nominal yield stress (taken as 50 ksi), L is the member length, r is the radius of gyration, and E is elastic modulus (taken as 29,000 ksi). Since the effective length (kl) is equal about all axes, only the minimum radius of gyration, r_z for the members of interest, is needed to evaluate the governing buckling capacity. The reduction factor Q is based on the b/t (width/thickness) plate slenderness ratios of the angle, where if the following inequality is satisfied, Q equals unity.

$$\frac{b}{t} \leq 0.446\sqrt{\frac{E}{F_y}} = 10.741 \qquad \textit{Equation 6-10}$$

Comparing this limit to the aspect ratios of the members of interest:

For L4 x 4 x ½: $\frac{b}{t} = \frac{4}{0.5} = 8$

For L3½ x 3½ x ⅜: $\frac{b}{t} = \frac{3.5}{0.375} = 9.3$

Therefore, for both angle sections the reduction factor Q = 1.0.

Table 6.3 summarizes the resulting compression stress capacities for all cross-frame members. Because no member has slenderness limit larger than 1.5, Equation 6-6 was used to calculate compression stress capacities in all cases. Figure 6.5 compares these strengths with the peak stresses for each member type. These results show that for four of the eight cross-frame member categories, demand exceeded capacity. These cases were both member types in the X-frame Staggered model and the bottom chord (4x4x1/2) in both K-frame layouts. The most critical member was the bottom chord (4x4x1/2) in the X-frame staggered model where demand was 29% larger than capacity (17.6 ksi versus 13.6 ksi). The X-frame Inline model was the sole model to have all cross-frame stresses to be below their calculated capacities.

To further investigate the effects of cross-frame configuration and layout on bridge behavior under service loads, bottom flange stresses were also analyzed. Table 6.4 summarizes the maximum magnitudes of longitudinal bottom flange stresses and the location where these stresses occur in the four parametric models. The highest stress, which was tensile, was 25.6 ksi and recorded in the X-frame inline model at Girder 3 five feet from the north abutment. The highest compressive stress was of nearly equal magnitude (25.3 ksi) and recorded in the K-frame staggered model at Girder 1, 15 ft. south of the pier support.

The locations of the maximum recorded longitudinal stresses in the bottom flange elements are typically near the supports, either the abutments or the pier. The peak stress may at first glance seem unexpected since the vertical bending moment at the abutments is zero and tensile stresses in the bottom flange over the pier are counterintuitive. However, these peak stresses are shown by Figure 6.6 to be due to

lateral bending forces, where the left side of the Figure 6.6 shows compressive stresses (indicated by negative values and blue) on the right side of the bottom flange occurring simultaneously with tensile stresses (indicated by positive values and red) on the left side of the same bottom flange cross-section, 5 ft. from the north abutment for the model shown, with other models producing similar results. The left side of Figure 6.6 also shows that moving away from the abutment the peak stresses decrease despite the fact that the vertical bending moment is increasing and that eventually the side of the flange on which peak stresses are experienced alternates.

In comparing these results to the bottom flange stresses discussed in Chapter 5(where only live load effects were considered, in contrast to the dead and live load effects considered in this chapter), the previously-reported location of maximum stress among the locations that were instrumented was at mid-span of the south span. This stress profile was recorded when the loading vehicle is 10 ft from the same mid-span location (load case 47FT, meaning the back axle of the truck is at a longitudinal distance 47 ft. from the Girder 4 north abutment). The overall maximum tensile and compressive girder stresses occurring anywhere in the US-13 model discussed in Chapter 5 occur in Girder5 close to the south abutment, which is shown in the right side of Figure 6.5.

Table 6.3 Compression Capacity for Cross-frame Members

	3½ x 3½ x ⅜ (Diagonal)		4 x 4 x ½ (Bottom Chord)	
	X-frame	**K-frame**	**X-frame**	**K-frame**
r_z	0.683		0.776	
Unbraced length (in)	59	62	112	56
$Q\lambda_{cz}$	0.86	0.90	1.43	0.72
$*\phi F_{cr-z}$ (ksi)	21.97	21.19	13.59	24.73

* ϕF_{cr-z} = compressive capacity about minor principle axis.

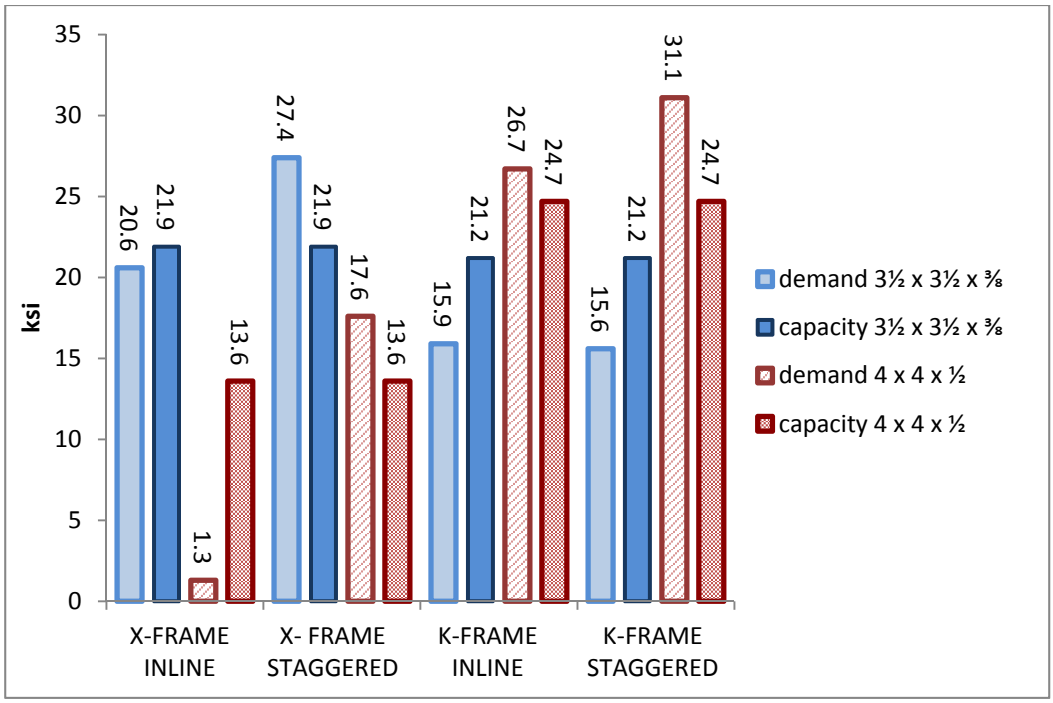

Figure 6.5 Comparison Between Compression Capacity and Demand for Cross-frame Bottom Chords and Diagonals

Table 6.4 Maximum Longitudinal Bottom Flange Stresses due HS-20 Loading

Action	FEM	Maximum Stress Value (ksi)	Location of Maximum Stress
Tension	X-FRAME INLINE	25.6	Girder 3, 5 ft. from north abutment BF East Edge
	X- FRAME STAGGERED	20.3	Girder 4, 5.5 ft. from north abutment BF West Edge
	K-FRAME INLINE	23.8	Girder 2, 4.5 ft. from north abutment BF West Edge
	K-FRAME STAGGERED	16.5	Girder 5, 11 ft. south from cross frames 5-4 BF West Edge
Compression	X-FRAME INLINE	23.2	Girder 3 , 5 ft. from north abutment BF West Edge
	X-FRAME STAGGERED	25.2	Girder 1, 15 ft. south from the pier support BF East Edge
	K-FRAME INLINE	22.6	Girder 5, at pier location BF Middle
	K-FRAME STAGGERED	25.3	Girder 1, BF East Edge, 15 ft. south from pier support

Thus, under both live load as well as the combination of dead load and live load, the maximum stresses in this model occur due to lateral bending and near the abutments. For this live load only case, the maximum stresses were also recorded when the moving applied load was in close proximity to the location of peak stress (during load case 287FT for this bridge with a total length of 330 ft.). Additionally, it is noted that magnitudes of maximum live load stress (shown in the legends of Figure 6.6 in psi) are only 11% of the maximum stresses due to the combination of service dead and live loads, which can be seen via comparison of the peak values of the legends of the two figures in Figure 6.6.

In comparing the bottom flange stress results from the four parametric models, it is seen that the greatest similitude and differences relate to whether inline or staggered cross-frames are used. This is particularly evident in the maximum reported tensile stresses shown in Table 6.4, where the inline cross-frames lead to bottom flange stresses that are 26 to 44% greater than the corresponding model with staggered cross-frames. This result is expected given the greater transverse stiffness of these models. However, the opposite trend is observed in the compression results, where the staggered cross-frames produce compressive bottom flange stresses that are 10% higher than the maximum compressive stresses in the inline models. This location of maximum compressive stress occurs at a critical location in Girder 1 where a cross-frame connects to the girder near the transition to a smaller bottom flange area. Given the different cross-frame layout of the inline cross-frames, the inline cross-frames do not align with the same point on Girder 1 and thus the maximum stress in these models is located elsewhere. Comparing the X-frame versus K-frame results, it is seen that the X-frame results typically have higher bottom flange stresses than the corresponding K-frame model. On average, this percent difference is 8%. The influence of cross-frame configuration and layout on girder stresses is further explored for their influence on inelastic behavior in the following section.

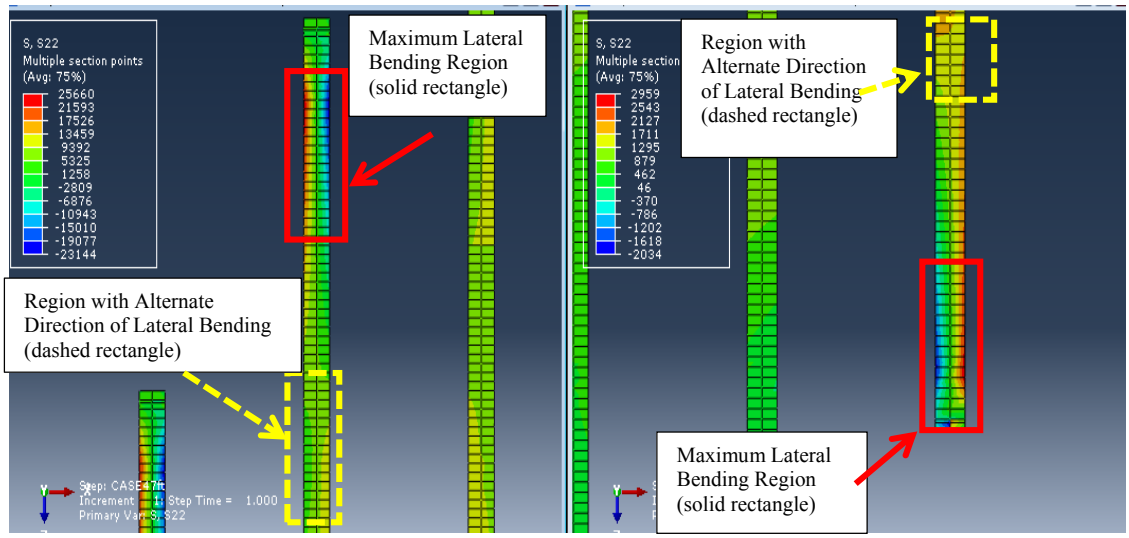

Figure 6.6 Stress Distribution under Maximum Stress Conditions for X-frame Inline Model: Dead load and Live Load (on Left) and Live Load Only (on Right)

6.4 Nonlinear-Plastic Analysis Results

6.4.1 Maximum Loading Results

Each of the four parametric models discussed in the previous section were also analyzed using the Riks method of analysis, which was described in Chapter 3. The goal of these analyses was to evaluate the non-linear response of the bridge as the girder design capacities are exceeded and load is redistributed up to the point where a system capacity of each model was obtained. Each of these models withstood high levels of loading up to loads between 57 and 82 times the wheel loads of the test vehicle used in the field testing described in Chapter 4. However, these maximum loading values represent the final loading at which equilibrium could be achieved in the analysis and there is no structural failure at these loading levels, such that these values can be considered a lower bound estimate of possible system capacities of these structures for the analysis assumptions used in these models (most notable of which are that adequate

transverse force redistribution mechanisms exist through elastic cross-frames and composite deck). At these high levels of loading, significant yielding and force redistribution occurred in the girders, as will be discussed later in this section. This demonstrates the significant reserve capacity and mechanisms for achieving this reserve capacity that is known to exist in steel girder bridges.

Conceptually, to fully exhaust the load-carrying capacity and load-path redundancy of this structure type, a failure mechanism must exist in all girders. For this two-span continuous structure, this means plastic hinges must be generated in each span and over the pier in each girder, for a total of 15 plastic hinges is this five girder cross-section. Given this significant level of plasticity that must be generated, it is not surprising that analytical convergence difficulties resulted when attempting to simulate this scenario. An additional complication in fully exhausting the load-carrying capacity is that it is only the live load in a fixed location (i.e., in only one span) that is being increased throughout the analysis such that the vertical bending moments in the opposite span are relatively low. Thus, at the maximum loading achieved in each of the models, four of the five girders had plastified near mid-span of the loaded span, one or two of the girders had plastified over the pier, and (other than this yielding over the pier) none of the girders had plastified in the span without live load.

Figure 6.7 shows the final load proportionality factors (LPF) from each analysis. In order to help designers to better understand the results from this analysis, the total magnitude of the applied loading, corresponding to multiples of the vehicle used in field testing (55.1 kips as shown on the left upper side in Figure 6.7), was scaled by the ratio of the field testing load to the total 72 kip load of an AASHTO HS-20 design loads

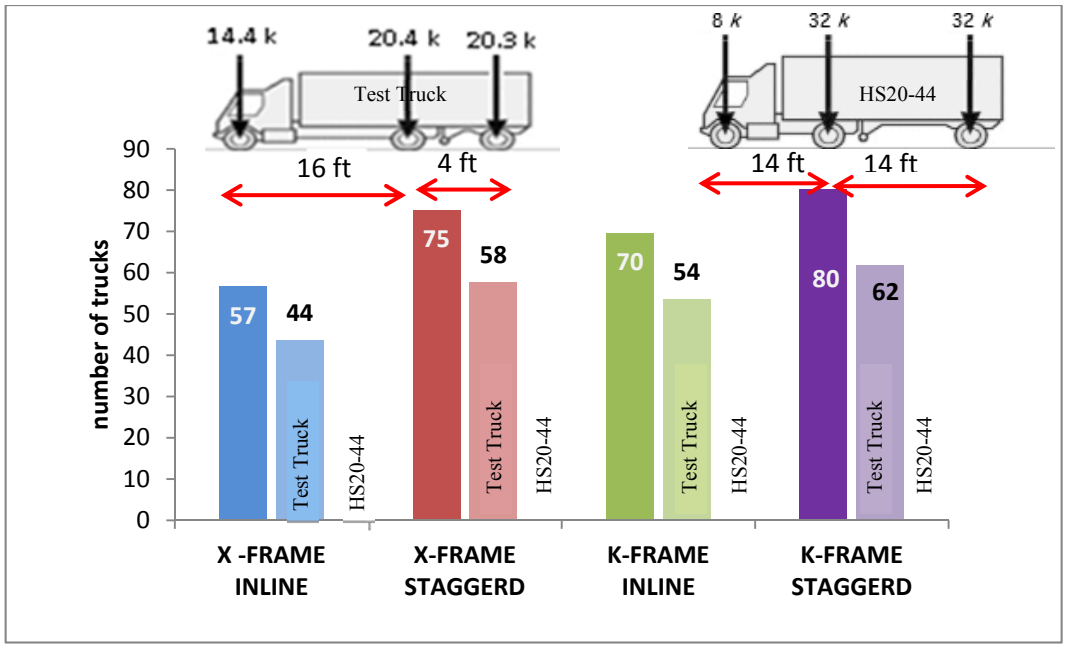

Figure 6.7 Load Proportionality Factors from Parametric Models

(shown on the right upper side in Figure 6.7). However, it is noted that the axle spacings of the test truck and design vehicle differ (as shown in the schematics inset into Figure 6.7), so the HS-20 magnitudes should only be interpreted as an approximation. Since convergence errors happened at different loads in each model, the model with the lowest ultimate load (57 test trucks in the X-frame inline model) established the load used as a baseline for comparison between the four models.

6.4.2 Cross-Frame Response

The cross-frame responses in each parametric model were first evaluated to determine the number of cross-frames in which the von Mises stress exceeded the yield stress, as previously explained in Section 6.2. As an example, Figure 6.8 shows the locations of yielded cross-frames in the north span of interest via red- colored elements and labels on these cross-frames for the K-frame Staggered model; the scope of the figure also includes Cross-frame 11-4 in the south span and the cross-frame connection plates in which yielding in these elements can also be observed. The locations of these

cross-frames and the location of the yielded element within the cross-frame (i.e., within a diagonal or bottom chord) as well as the LPF when the yield stress was exceeded were recorded for each parametric model. The LPF was converted to corresponding number of HS-20 trucks and the results were compiled in increments of 2 to 15 HS-20 trucks as shown in Table 6.5. In Table 6.6, the counts of the yielded cross-frame members and cross-frames is provided, where the first number in the ratio represents the number of yielded members (categorized by diagonals and bottom chords) or cross-frames in the north span of the bridge and the second number represents the total number of cross-frames in the north span of the bridge, where the live load is applied and the majority of yielding occurs. Specifically, all except for two of the yielded cross-frames are in the north span. These two exceptions are listed and denoted with an asterisk in the Table 6.5, Diagonal 10-3 and Diagonal 11-4, but not included in the summary counts in Table 6.6.

The results shown in Table 6.6 are also shown graphically in Figure 6.9. These results demonstrate that the most cross-frame yielding occurred in the K–frame Inline model which had 54% of its cross-frames in the north span yield, with 25% of cross-frames having at least one diagonal yield and 50% of the bottom chords experiencing. The model with second highest amount of cross-frame yielding (based on the established methodology for quantifying this) was the X-frame Inline model, which had 44% of its cross-frames yield where all of these had at least one diagonal yield and 13% of the bottom chords in this span were yielded. This total amount of yielding was similar to that observed in the K-frame Staggered model, which had 41% of its cross-frames yield; however, in this case the members which were yielded was reversed, with all of the yielded cross-frames having a yielded bottom chord and 17% of the diagonals in the span experiencing yielding. The X-frame Staggered model experienced significantly less cross-frame yielding, with only 14% of the north span cross-frames yielded; similar to the X-frame Inline model, the cross-frame diagonals experienced

more severe stress states with all cross-frame yielding in this model occurring in the diagonals. Thus, general conclusions from this analysis are that inline cross-frames experience higher stresses than a corresponding configuration of staggered cross-frames and that the most heavily stressed members in the X-frames are the diagonals while the most heavily stressed members in the K-frames are the bottom chords.

In comparing these results to the relative magnitudes of cross-frame stress resulting from the linear-elastic analysis discussed in Section 6.3, some interesting similarities and differences are observed. Recall in the linear-elastic results, the X-frame Inline model showed the highest cross-frame tensile stress and the K-frame Staggered model showed the highest cross-frame compressive stress. Thus, it might be expected to see the largest number of yielded cross-frame to be in one of these two models. Additionally, the linear-elastic analysis showed that X-frame Inline and K-frame Staggered models had highest bottom flange stresses in tension (25.6 ksi) and compression (25.3 ksi), respectively. However, it is the K-frame Inline model that showed the largest number of yielded cross-frames. This greater extent of yielding coupled with lower stress magnitudes suggests that this model is more efficient at distributing and / or redistributing load among the girders. This hypothesis will be evaluated using the bottom flange stress results in the following section (Section 6.4.3). It is also noted that the K-frame Inline model is also the only one of the four models where there are both some cross-frames with only a diagonal member yielded and other cross-frames with only a bottom chord yielded. Additionally, the disparity between the amount of bottom chord and diagonal yielding (as quantified by the percent difference of these two percentages) is smallest in the K-frame Inline model. These facts also suggest that load is more uniformly distributed throughout the cross-frames. Figure 6.10 shows the locations of yielded cross-frames in the north span of the K-frame Inline model via red- colored elements and labels on these cross-frames. Comparing this

Table 6.5 Comparison of Cross-frame Yielding in Parametric Models

Number of HS-20 Trucks	X-Frame Inline	X-Frame Staggered	K-Frame Inline	K-Frame Staggered
0-15	Diagonal 14-4		Diagonal 12-4, 13-4, 15-4 Bottom Chord 12-4, 15-4, 17-2	Diagonal 12-4, 15-4 Bottom Chord 12-4
16-23	Diagonal 13-4, 15-4	Diagonal 12-4, 14-4, 15-4	Diagonal 18-3 Bottom Chord 18-3	Diagonal 13-4 Bottom Chord 13-4, 14-4, 19-4
24-31	Diagonal 15-3 Bottom Chord 17-2	Diagonal 13-4	Diagonal 11-3 Bottom Chord 19-4, 13-4, 13-2	Diagonal 16-4
32-35	Diagonal 14-3, 17-2		Bottom Chord 12-2, 12-1, 13-3, 14-4	Diagonal 11-4* Bottom Chord 13-3, 13-2, 14-2
36-38	Bottom Chord 18-3		Diagonal 15-2, 12-1	Bottom Chord 12-3
39-42	Diagonal 12-2,12-3,12-4, 13-2, 14-2, 16-1 Bottom Chord 17-2, 16-1	Diagonal 10-3*	Diagonal 13-1 Bottom Chord 13-1, 11-3, 16-1, 12-3 , 13-3	Diagonal 12-3
43-44	Diagonal 18-3, 14-2			Bottom Chord 13-1, 15-3, 14-2

*Cross-frames on the south span of the bridge, not included in Table 6.6.

figure to Figure 6.8, this trend of more uniform load distribution in the inline model can also be visually observed.

Table 6.6 Summary of Yielded Cross-frames in North Span

	X-Frame Inline	X-Frame Staggered	K-Frame Inline	K-Frame Staggered
Cross-frames	14/32 (44%)	4/29 (14%)	17/32 (53%)	12/29 (41%)
Diagonals	14/32 (44%)	4/29 (14%)	8/32 (25%)	5/29 (17%)
Bottom Chord	4/32 (13%)	0/29 (0%)	16/32 (50%)	12/29 (41%)

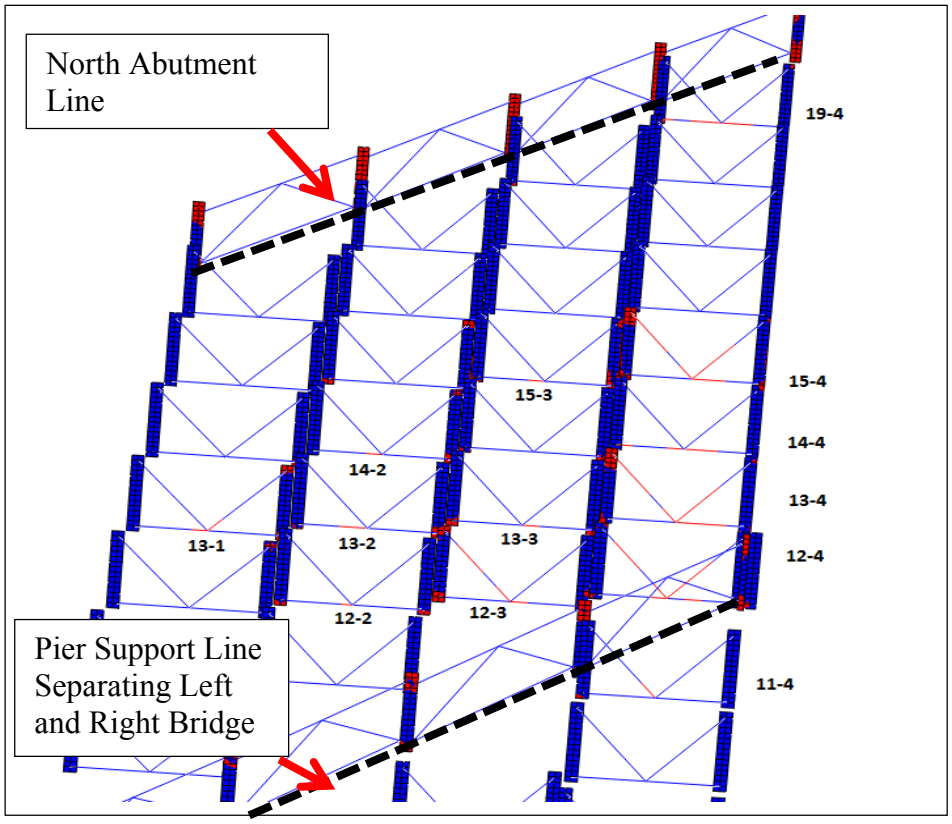

Figure 6.8 Yielded Cross-frames in K–frame Staggered Model

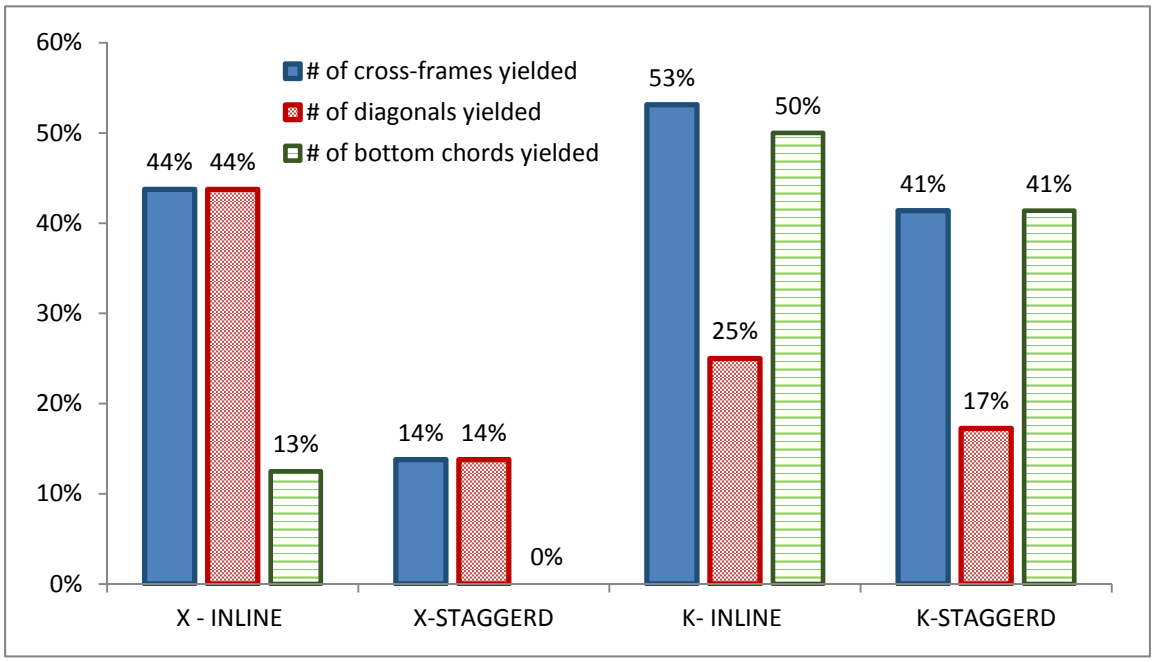

Figure 6.9 Comparison of Extent of Cross-frame Yielding in Parametric Models

6.4.3 Bottom Flange Results

Table 6.7 presents a summary of the progression of bottom flange yielding and plastification as load is increased in the parametric models. As discussed in Section 6.2, the bottom flange is considered yielded if the computed stress in the any bottom flange element exceeds the assumed yield stress of 55,104 psi and Abaqus post-processing tools were used to spatially visualize stresses exceeding this limit through color-coded stress contours. The bottom flange is considered plastified if all elements in any bottom flange cross-section exceeded the assumed yield stress. Table 6.7 considers yielding and plastification at three locations along the length of each girder: the region over the pier supports, locations near mid-span of the loaded north span, and the north end. The region of the pier support is a logical location for girder yielding as this is theoretically the location of peak negative vertical bending moment in a two-span continuous structure. Similarly, “mid-span” is used as a concise label to generally refer to locations

near mid-span, which would be expected to be the locations of peak positive bending moment in a two-span continuous structure subjected to vertical bending moment. The yielding and plastification observed at the north ends of the girders is less intuitive and occurs due to the large amount of lateral bending stress occurring at these locations where the plastification that occurs is due to one side of the bottom flange yielding in compression and the other side yielding in tension. At the Table 6.8, the percentage of the girders in the bridge cross-section that have yielded at each of the three locations of interest is summarized and Figure 6.11 presents this same data graphically. A final clarification of the format of Table 6.7 is that the girder labels are abbreviated for conciseness in that Girder 1 is labeled G1, Girder 2 is labeled G2, etc.

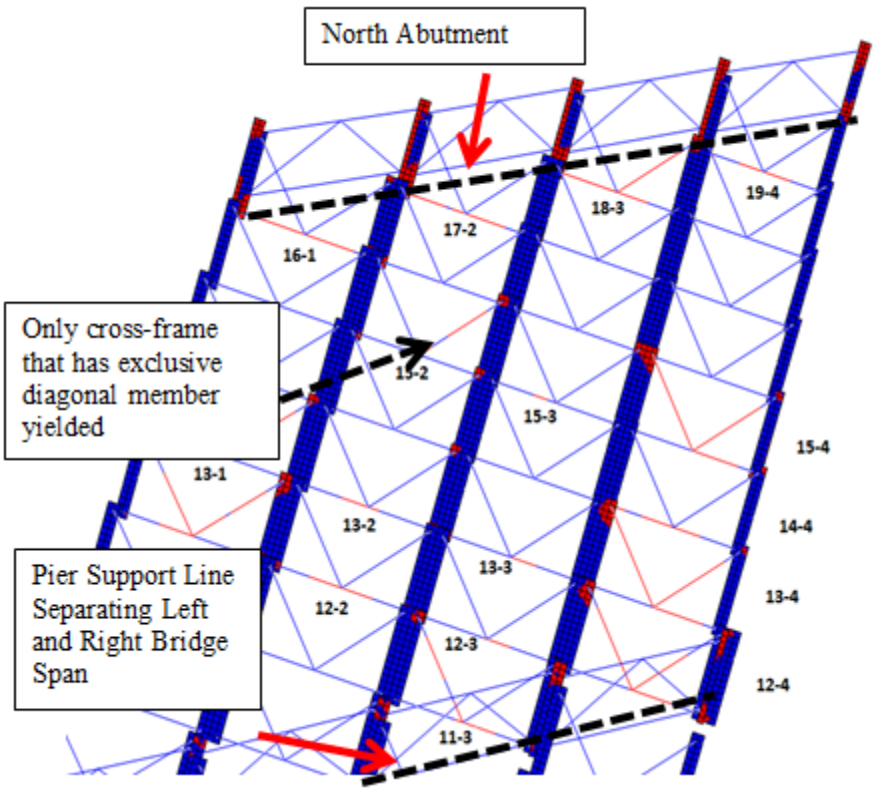

Figure 6.10 K-frame Inline Cross-frames Yielding Pattern

The data in Table 6.7 and Figure 6.11 shows that highest percent of girder yielding (up to 100%) happens at the north end support and that girders at mid-span also experience extensive yielding, with all four parametric models having four of the five girders in the cross-section yielded at mid-span. The girder that is not yielded at mid-span is Girder 1, which is the exterior girder farthest from the applied loading. In contrast, only one or two girders (20 to 40% of the girders in the cross-section) have yielded at the pier support. The highest percent of plastification (80% in all models) was recorded at mid-span. Significantly less plastification occurs above the support and the pier (ranging from 0% to 40%). In all cases yielding starts above the supports, while plastification starts at mid-span. In comparing the results of the four models, the X-frame Staggered model experiences the least yielding, while the K-frame Staggered model experiences the least plastification, being the only model that did not have at least one girder plastified at the north end support.

In order to further synthesize the data shown in Table 6.7 and Figure 6.11, the percentage of the girder length that was yielded in each model as the loading increased was computed, as previously described in Section 6.2. This data is summarized by Figure 6.12. The data shows that the plasticity spreads less in the longitudinal direction in both inline models, with the two inline models following similar trends and having a total yielded length of 24% at the final loading of 44 trucks. In contrast, 33% of the girder length was yielded at the final loading in the staggered models, which also follow similar trends to one another. Additionally, Figure 6.12 shows that up to a loading of 23 trucks, there is not a significant difference between how the different models distribute load longitudinally. However, after 23 truck-loads there is a clear distinction between the different cross-frame layouts.

This finding that cross-frame layout has a greater influence on load redistribution patterns than cross-frame configuration is logical for these models where the cross-frames are modeled to have infinite strength. Thus, to further assess the

influences of cross-frame configuration, maximum cross-frame strains in the various models are summarized in Tables 6.9 and Table 6.10. These results show that the highest strain values were recorded in the diagonal member of the K-frame Staggered ($1.3x10^{-2}$) model in tension, while the highest compressive strain was recorded in the bottom chord member of the K-frame Inline ($1.0x10^{-2}$) model. This peak tensile strain is in the same order of magnitude but lower in value that typical values for the uniaxial tensile failure of steel; thus, it is likely that little difference in performance would result if the tensile non-linear properties were included in the analysis.

The peak compressive strains are of greater concern due to the potential for buckling in these members, where Figure 6.13 shows the compressive strain capacities relative to the maximum compression strains reported in Table 6.10. These capacities were based on dividing the compressive stress capacities previously reported in Table 6.3 by an elastic modulus of 29,000 ksi. This shows that the compressive capacities of both member types were exceeded in all four models. The largest difference was detected in the diagonal member of the K-frame Inline model where the capacity is only 7% of the demand. The bottom chord of this model is also shown to be strained well past its capacity, where the capacity is only 22% of the demand. The K-frame Inline maximum strains also exceed the compressive strain capacities by similar margins. In contrast, the X-frame Staggered model is observed as experiencing both the lowest magnitude of peak compressive strain and lower demand to capacity ratios. In comparison, the bottom chord strains in the X-frame Inline model are of nearly equal magnitude; however, the diagonal members in the X-frame Inline model experience nearly double the strain of the same members in a staggered configuration. Thus, it can be concluded that the load redistribution mechanisms enabling the girder responses shown here are not likely to be achieved with the current cross-frame members, but that modifications to the X-frame staggered configuration may provide the best opportunity for replicating the significant reserve capacity seen in the these models.

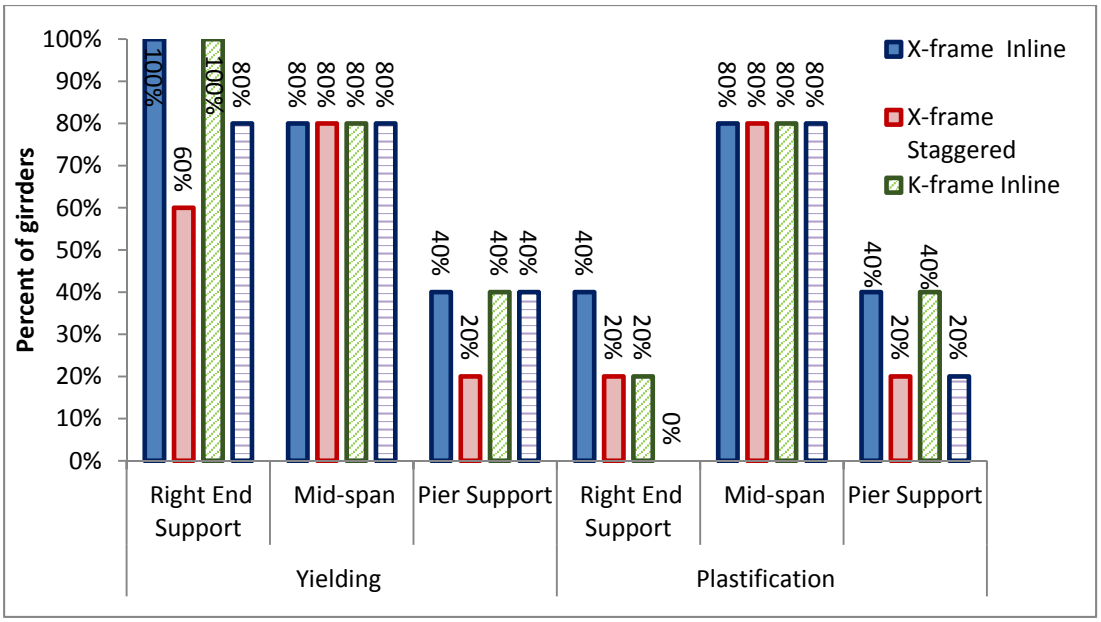

Figure 6.11 Percent of Girders That Has Bottom Flange Yielded and Plastified During Nonlinear Plastic Analysis

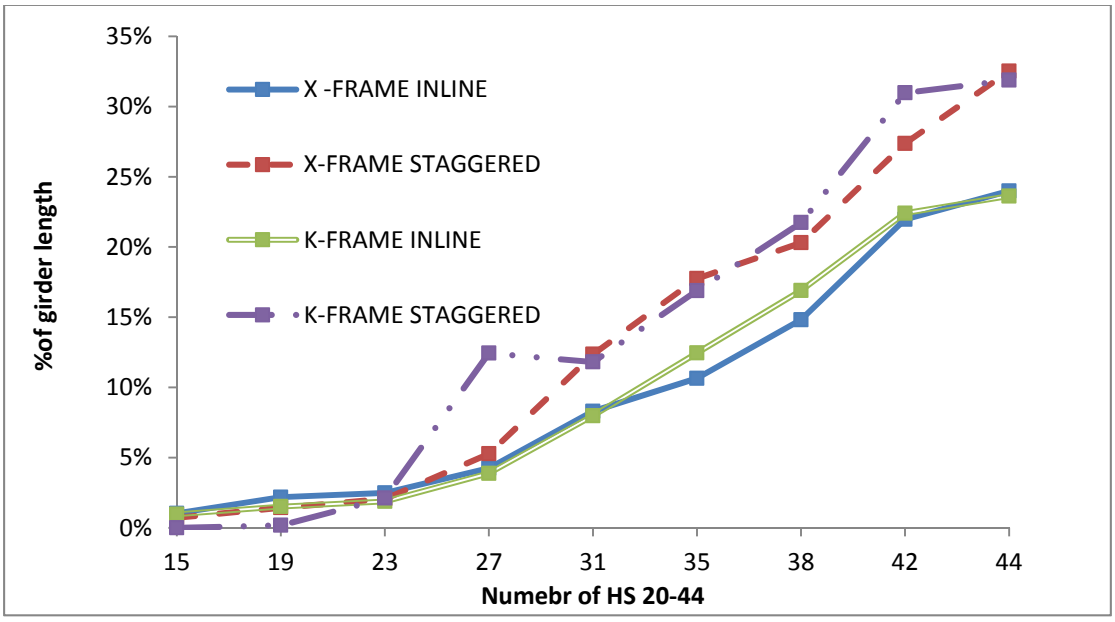

Figure 6.12 Percent of Linear Feet of North Span over which Bottom Flange has Yielded

Table 6.7 Bottom Flange Yielding and Plastification

Truck Increment	X-frame Inline	X-frame Staggered	K-frame Inline	K-frame Staggered
0-15	G2, G3, G4 at supports yielded. G2, G3, G4, G5 at mid-span yielded. G5 at pier yielded.	G4 at support yielded. G4 at mid-span yielded.		
16-23	G4 at mid-span plastified. G5 at pier plastified.	G3 at mid-span yielded. G5 at pier yielded.	G2, G3 at supports yielded. G5 at pier yielded. G4 at mid-span plastified.	G3 at support yielded. G4 at mid-span yielded. G5 at pier yielded.
24-31	G5 at mid-span plastified.	G4 at support plastified. G4, G5 at mid-span plastified. G5 at pier plastified.	G1 at support yielded. G3 at mid-span yielded. G5 at mid-span plastified. G5 at pier plastified.	G3, G5 at mid-span yielded. G3, G4 and G5 at mid-span plastified. G5 at pier plastified.
32-35	G3 at mid-span plastified. G2, G3, G4 at supports plastified.	G3 at mid-span plastified. G2 at support yielded.	G4, G5 at support yielded. G4 at pier yielded. G2 at support plastified.	G4 at pier yielded. G2 at support yielded.
36-38	G1, G5 at support yielded. G4 at pier yielded.	G2 at mid-span yielded.	G2 at mid-span yielded. G3 at support plastified.	G2 at mid-span yielded.
39-42	G2 at mid-span plastified.	G2 at mid-span plastified.	G2 at mid-span plastified. G4 at pier plastified.	G2 at mid-span plastified.
43-44	G4 at pier plastified.	G1 at support yielded.	G1 support at yielded.	G4, G5 at support yielded.

Table 6.8 Summary of Bottom Flange Yielding and Plastifications

	Location	X-frame Inline	X-frame Staggered	K-frame Inline	K-frame Staggered
Yielding	North End Support	5/5 (100%)	3/5 (60%)	5/5 (100%)	4/5 (80%)
	Mid-span	4/5 (80%)	4/5 (80%)	4/5 (80%)	4/5 (80%)
	Pier Support	2/5 (20%)	1/5 (20%)	2/5 (40%)	2/5 (40%)
Plastification	North End Support	2/5 (40%)	1/5 (20%)	1/5 (20%)	0/5 (0%)
	Mid-span	4/5 (80%)	4/5 (80%)	4/5 (80%)	4/5 (80%)
	Pier Support	2/5 (40%)	1/5 (20%)	2/5 (40%)	1/5 (20%)

Table 6.9 Maximum Tensile Cross-frame Strains

FEM	Maximum Tensile Strain	Cross-frame Location
X-FRAME INLINE	4.9×10^{-3}	17-2 Bottom Chord
X- FRAME STAGGERED	3.4×10^{-3}	14-4 Right Diagonal
K-FRAME INLINE	1.3×10^{-2}	15-4 Left Diagonal
K-FRAME STAGGERED	1.0×10^{-2}	13-4 Left Diagonal

Figure 6.14 shows the percentage of the girder length in the loaded span that was plastified in each model as the loading was increased. It was previously shown in Figure 6.12 that the yielded length of the various models began to diverge between after 23 trucks. Figure 6.14 shows that this is a logical result as this corresponds to when the bottom flange starts to plastify. The data in Figure 6.14 also suggests that the

Table 6.10 Maximum Compressive Cross-frame Strains

Cross-frame Member		Maximum Compressive Strain Demand	Compressive Strain Capacity	Capacity-to-Demand Ratio	Demand-to-Capacity Ratio
X-FRAME INLINE	Diagonal L3½x3½x⅜	0.00457	0.000755	16.52%	6.1
	Bottom L4x4x½	0.00062	0.000469	76.13%	1.3
X- FRAME STAGGERED	Diagonal L3½x3½x⅜	0.0028	0.000755	26.97%	3.7
	Bottom L4x4x½	0.0007	0.000469	67.00%	1.5
K-FRAME INLINE	Diagonal L3½x3½x⅜	0.01	0.000731	7.31%	13.7
	Bottom L4x4x½	0.0038	0.000852	22.41%	4.5
K-FRAME STAGGERED	Diagonal L3½x3½x⅜	0.0086	0.000731	8.50%	11.8
	Bottom L4x4x½	0.0046	0.000852	18.52%	5.4

inline cross-frame configurations result in slightly higher lengths of girder plastification than staggered cross-frame configurations. Comparing this observation with the observations on yielded lengths in Figure 6.12, where it is the staggered configurations displaying greater yielded lengths, it is concluded that the inline models tend to concentrate plasticity such that girder plastification is greater than in the staggered models, while the staggered models allow plasticity to spread to a greater extent such that girder yielding is greater than in the inline models. This is a logical result as the stagger promotes a greater longitudinal distribution of stress.

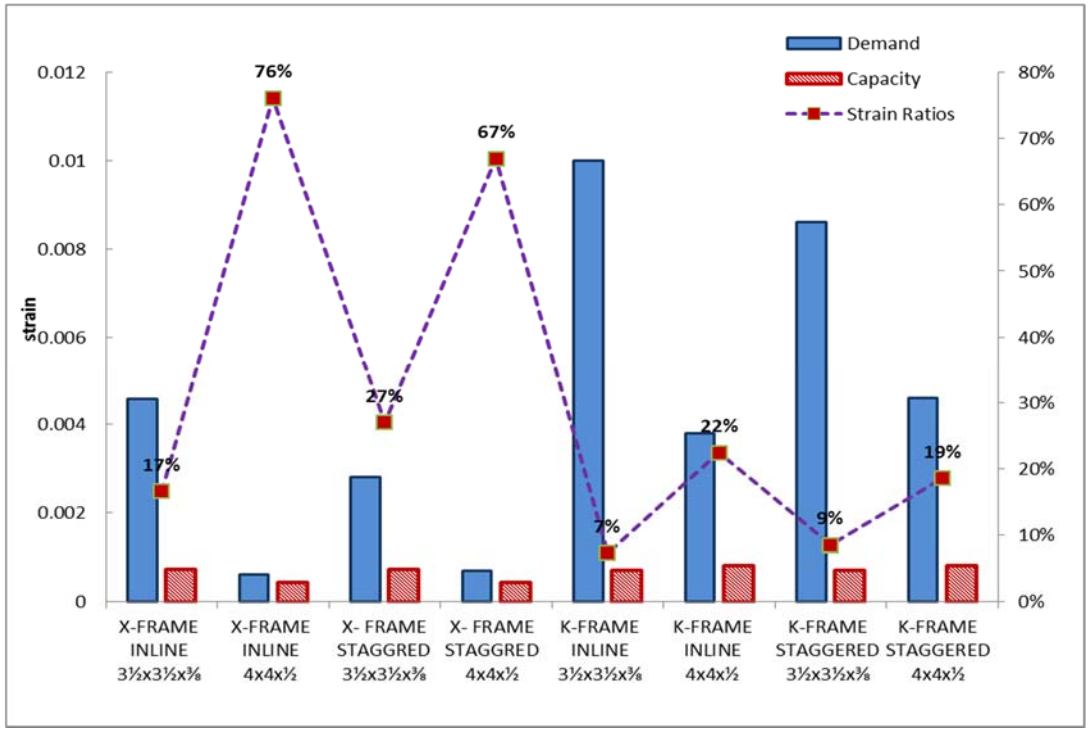

Figure 6.13 Comparison of Peak Compressive Strains Relative to Compressive Strain Capacities

Figures 6.15 and 6.16 show views of the general spread of plasticity that occurs in each cross-frame configuration, as viewed from the bottom of the bridge. Here yielded bottom flange and cross-frame elements are white and non- yielded elements are blue. The figures show the same regions of each model to similar scales. This shows that in the inline models the plasticity tends to spread from one girder to another in a path that is perpendicular to the girders, as load travels through the cross-frames. In contrast, in the staggered models, the yielded length is larger as the load has more points along the girder length where load can be transferred transversely due to the discontinuities in cross-frame placement. However, there are fewer points where the full bottom flange cross-section has yielded, indicating greater lateral bending

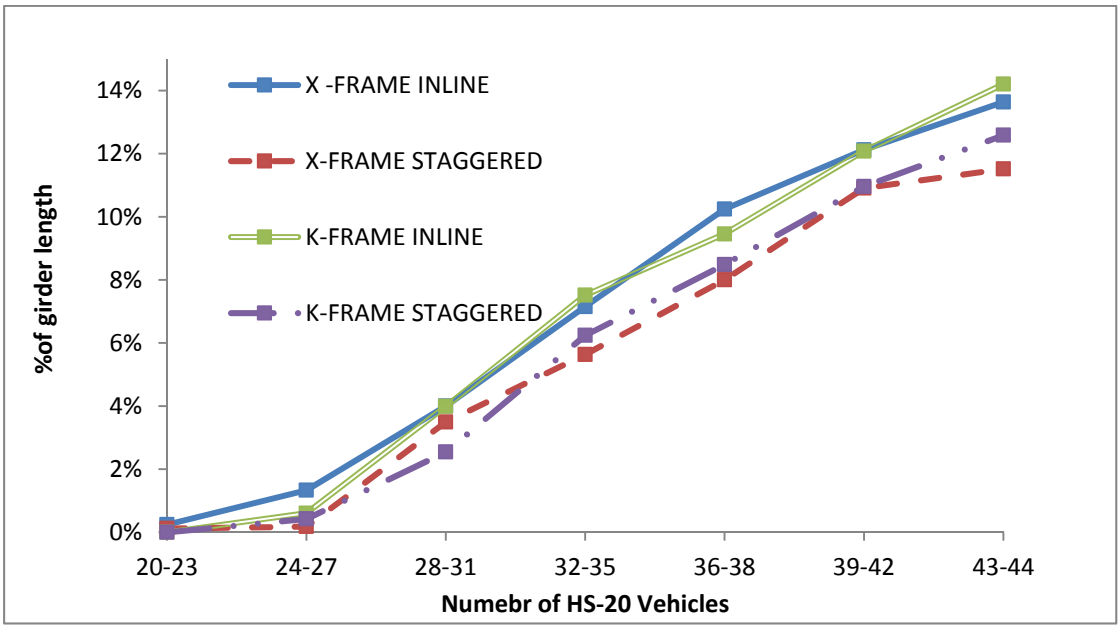

Figure 6.14 Percent of Linear Feet of North Span That Bottom Flange has Plastified

stresses in these models. These differences are again demonstrating that cross-frames are playing a vital role in load redistribution.

In order to assess how cross-frame layout and configuration affects the distribution of load, girder distribution factors (GDF) are computed (Equation 6-1) for the most-heavily stressed girder based on the stresses in a common cross-section near mid-span in each model as previously discussed in Section 6.2. Table 6.11 tabulates these GDF, where it can be seen that X-frame Inline and K-frame Staggered have the lowest GDFs (0.232), suggesting that these two models distribute load most efficiently. The X-frame Staggered has the largest GDF (0.250), but even this value is relatively close to the ideal inelastic load distribution factor of 0.200, which assumes equal load distribution to all five girders in the cross-section, hence GDF = 1/5 = 0.200. However, the calculation process discussed in Section 6.2 should be

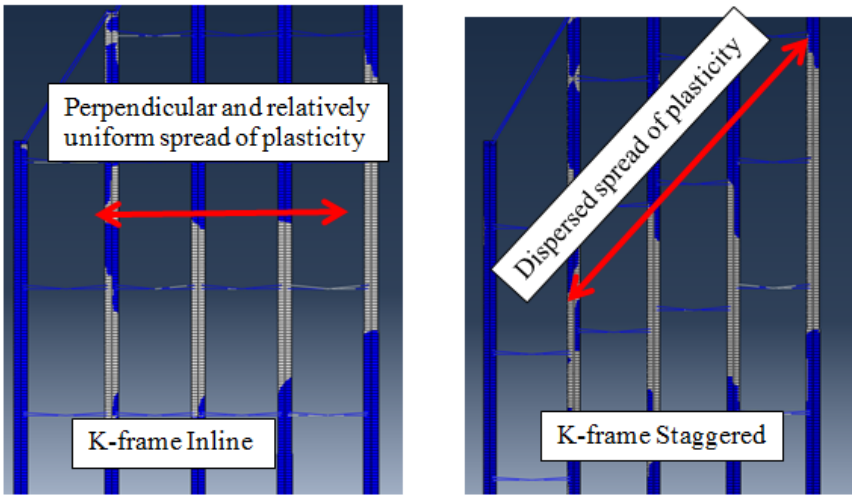

Figure 6.15 Spread of Plastification for K-frame Inline (left) and K-frame Staggered (right) Models

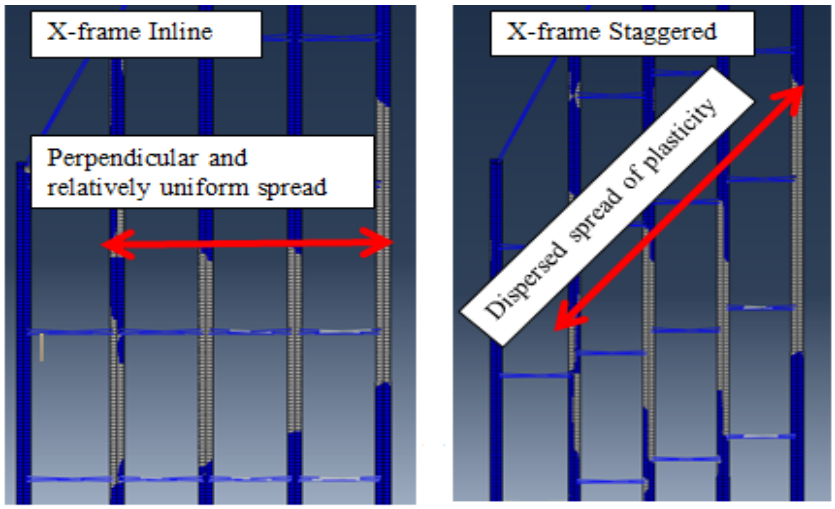

Figure 6.16 Spread of Plastification for X-frame Inline (left) and X-frame Staggered (right) Models

considered before placing emphasis on this result. Specifically, it should be recalled that: these GDF values are based on dead load and live load, which will lower the values compared to a non- uniformly placed live load only calculation; the stresses in Table 6.11 are not necessarily the maximum girder stresses and the GDF in Table 6.11 would decrease if peak stresses were used; and these are peak stresses in any element

comprising the bottom flange cross-section of interest and thus include lateral bending effects, which may also influence the magnitude of the GDF. Each of these influences should be carefully evaluated before definitive conclusions on this topic are suggested. For example, Table 6.12 evaluates the difference in results that are obtained when using only live load, where it is shown that the live load GDF are higher as would be expected, but the maximum difference between the distribution factors for common cases in Tables 6.11 and 6.12 is only 8%.

In comparing the results of the various models, the most significant difference is the stress distribution in Girders 4 and 5 in the X-frame Staggered model relative to the other three models. Specifically, in the X-frame Staggered model there is much higher stress in Girder 4 than in the other models, which results in a higher GDF for this model. This is likely because the location of the staggered inline cross-frame is adjacent to the point where the Girder 4 stress value was extracted. Thus, the higher GDF value for this model is likely indicating greater lateral bending in this model at this common location, and may not be indicative of a general load distribution trend.

Table 6.13 shows theoretical GDF factors based on various means of calculation specified in AASHTO LRFD Bridge Design Specifications (2012) for the cross-sections where stresses were reported in Tables 6.11 and 6.12. Here it is shown that for one lane loaded (as considered in the parametric model results in Tables 6.11 and 6.12), the interior girder has an elastic distribution factor of 0.39 and the exterior girder distribution factor is governed by the Lever Rule, which predicts a relatively high distribution facto of 0.82. The governing GDF for interior girder is 0.6 and the governing GDF for the exterior girder is again 0.82. Both of these values are significantly greater than the GDF values in Tables 6.11 and 6.12, suggesting that the

GDF have significantly decreased to inelastic behavior but the differences in the philosophies behind the AASHTO and Tables 6.11 and 6.12 data may be influential to this difference.

Table 6.11 GDF at Selected Cross-Section

FEM	GDF	Girder 1 BF Stress (ksi)	Girder 2 BF Stress (ksi)	Girder 3 BF Stress (ksi)	Girder 4 BF Stress (ksi)	Girder 5 BF Stress (ksi)
X-frame Inline	0.232	32.81	55.17	56.57	61.36	62.25
X-frame Staggered	0.250	30.99	55.15	56.63	66.92	57.71
K-frame Inline	0.234	28.93	55.17	56.72	61.71	60.76
K-frame Staggered	0.232	30.97	54.47	56.72	61.26	60.98

Table 6.12 Live Load GDF at Selected Cross-Section

FEM	GDF	Girder 1 BF Stress (psi)	Girder 2 BF Stress (psi)	Girder 3 BF Stress (psi)	Girder 4 BF Stress (psi)	Girder 5 BF Stress (psi)
X-frame Inline	0.250	22555	47718	49681	55419	58493
X-frame Staggered	0.262	20291	48324	48881	61012	53955
K-frame Inline	0.250	18717	47683	49677	55602	57130
K-frame Staggered	0.251	20323	47585	48373	55341	57411

Table 6.13 Theoretical AASHTO GDFs for Cross-Sections of Interest

	Interior Girders	**Exterior Girders**			
		Lever Rule	e*DF-interior	Cross-frames	**Governing**
One Lane	**0.39**	0.82	NA	0.52	**0.82**
Two Lanes	**0.60**	NA	0.60	0.51	**0.60**

6.5 **Conclusions**

The results from this chapter clearly showed that cross-frame and girder stresses are influenced by cross-frame configuration and layout at both the service and ultimate limit states. The most significant influence was observed in the cross-frame stresses. At service load levels, it was shown that peak compressive (governing) cross-frame stresses can vary by 50% in the different models, with K-frames in a staggered configuration producing the greatest stress and inline X-frames producing the lowest stress. While both cross-frame configuration and layout influenced this result, the cross-frame stresses were observed as being more sensitive to configuration, with the K-frames most consistently producing higher stresses. However, in assessing the governing compressive stress results relative to the buckling capacities of the cross-frame members, it was seen that the design stresses are exceed by as much as 29% under the service level loading and that this occurs in the bottom chord of the X-frame, which has a significantly reduced capacity compared to the other members, in the staggered model. This effect should be given careful consideration as a comparison of the predicted stresses relative to the buckling capacity of the cross-frame members showed that cross-frame members in three out of four models fail to provide sufficient capacity to resist the peak applied compressive stress in the cross-frames in the corresponding model. The X-frame Inline model serves as the exception to this statement and the peak applied stresses are 94% of the governing buckling stress in this model. Tensile stresses in the cross-frames indicated that these members have significant reserve capacity in tension under service loads.

As the ultimate behavior of the bridge models are assessed and the load magnitude equivalent of 44 HS-20 vehicles was applied, it was not surprising that the

cross-frame capacities were shown to be exceeded in all models. In comparing the results of the various models, cross-frame configuration was again revealed to be more influential in terms of cross-frame strains than the cross-frame layout. Peak cross-frame strain was detected in the K-frame Inline model, with the K-frame Staggered model generating similar results. In contrast, the X-frame Staggered model was observed as experiencing both the lowest magnitude of peak compressive strain and lower demand to capacity ratios. Thus, it can be concluded that the load redistribution mechanisms necessary for achieving the significant reserve capacity of which the girders are capable of achieving are not likely to be achieved with the current cross-frame members, but that modifications to the X-frame staggered configuration may provide the best opportunity for replicating the significant reserve capacity seen in the these models.

Clear, but less significant, influences on the girder response were also observed due to cross-frame configuration and layout. Specifically, in terms of peak bottom flanges stresses under service level loads, it was found that stagger increases the compressive stress (which is assumed to be the governing stress) by as much as 12%. With respect to the influence of cross-frame configuration, X-frames also typically had peak bottom flange stresses larger than the corresponding K-frame stresses, with this difference being 8% larger on average. In the assessment of the inelastic performance of the four parametric models, it was once again seen that the cross-frame layout was more influential on girder response as the staggered models produced similar trends to one another in terms of the progression of yielding and plastification in the models while the inline models also produced trends similar to one another but distinct from the staggered layout results. However, these effects do not

indicate any significant consequence on the structural performance of the girders in terms of peak magnitude of stress under service level loads or a significant difference in the load distribution characteristics of the girders based on the metrics used in this work.

Thus, when considering the differing effects of cross-frame configuration and layout on the cross-frame and girder responses, more emphasis is placed on the cross-frame results for two reasons. First, it has been shown that the cross-frames are more influenced by the variables evaluated at both the service and ultimate loading conditions. Second, while the girder properties are modeled with realistic properties, the cross-frames are modeled with linear-elastic properties that are not practical to achieve at the ultimate load levels considered. Thus, considering that the final girder stress state of all models was relatively similar in demonstrating favorable load redistribution, this load redistribution will be most likely to be achieved in situations where the cross-frame stress is minimized. Given these considerations, it is concluded that the X-frame staggered configuration is the one most likely to lead to the greatest reserve capacity in the system. Modifications to the member sizes used in these cross-frames likely provide the best opportunity for further increasing this reserve capacity.

Chapter 7

CONCLUSIONS

7.1 Summary of Scope of Work

The primary objectives of this research were to quantify the forces in cross-frames in skewed steel I-girder bridges through field testing, to create a finite element model that replicates the three-dimensional behavior of the bridge suggested by these forces, and perform an FEA parametric study evaluating cross-frame effects at elastic and inelastic load levels. Two bridges of varying skews in the state of Delaware were chosen based on parameters such as skew, cross-frame type, and cross-frame spacing. These bridges were SR 1 over US 13, a 65 degree skew bridge approximately 5 miles south of the Chesapeake & Delaware Canal in Delaware, and SR 299 over SR 1, a 32 degree skew bridge located in the Middletown-Odessa area of Delaware. Both bridges were heavily instrumented with strain transducers on the girders and cross-frames, with the majority of the instrumentation placed on the cross-frames given the research objectives. Over four days of field testing, eleven cross-frames and six girder cross-sections were tested between both bridges. Instrumentation layouts for both bridges were created based on a preliminary finite element analysis then slightly adjusted based on logistical constraints. Data was recorded each day for different passes of a weighed tri-axle dump truck provided by DelDOT. Ultimately, the field testing of both bridges was a success and a large amount of useful data was gathered.

The second primary component of the research was to create and analyze FEM of both bridges. The modeling techniques to create these models was discussed in Chapter 3. Chapter 5 then discussed both the results of these models relative to the field test results and theoretical behavior to assess whether the analytical response

predicted from these models was of acceptable accuracy. The greater resolution of FEA relative to the relatively limited number of discrete points and data types that can be recorded with field instrumentation also allows the behavior suggested by field results to be further explained.

The final primary component of the research was to perform an FEA parametric study, evaluating the influences of cross-frame configuration (K-frames versus X-frames) and cross-frame layout (staggered versus inline). These models were evaluated under both moving service-level loads where a linear elastic analysis was performed and under ultimate loads where the live load in a fixed position was proportionately increased until a converged solution could no longer be obtained. In both analyses, the effects of the differing cross-frame configurations and layouts on output such as the maximum compressive and tensile stresses occurring in the bottom flange of the girders and cross-frames along with the locations of these peak stresses were evaluated. In the ultimate loading scenarios, the extent of yielding in the bottom flange, load distribution among the five girders in the cross-section and the comparison of these values to AASHTO live load distribution factors, as well as peak strains in the cross-frames were also assessed.

7.2 **Results**

7.2.1 **Field Test Data**

Cross-frames and girder locations were instrumented on two bridges of varying skews, (x and y degree skews) and the bridges were load tested with a weighed truck. The most significant differences between the responses of these two

bridges were that in the bridge with staggered K-frames and less skew (SR-299) the cross-frame forces were significantly reduced and the magnitude of lateral bending was significantly higher. The data generated in the field testing also indicates a significant amount of bending in some cross-frames. These issues are further discussed in the following paragraphs.

As a frame of reference for considering the reported cross-frame stresses, in SR-299 the maximum bottom flange stress was 1.7 ksi while the maximum cross-frame stress is of similar magnitude, 1.5 ksi. For the more-heavily skewed bridge, US-13, the maximum bottom flange stress was also of similar magnitude (1.5 ksi) while the maximum cross-frame stress is nearly three times this value, 4.2 ksi. This was recorded in a cross-frame adjacent to the obtuse corner of the bridge (Cross-frame 4-4 in Figure 4.3). This result is due to the obtuse corner being a critical location in this highly skewed bridge and the significant amount of bending experienced by this member, which is evidenced by the 4.5 ksi difference between the two readings on opposing legs of this same angle section. When the average stress indicated by the pairs of gauges at a common cross-frame member cross-section is considered, the maximum value in US-13 is again significantly higher than any stress recorded in SR-299. Specifically, the peak average stress through the cross-section of an angle member is 3.6 ksi, which occurs in a diagonal member of a cross-frame near the maximum positive moment location. As an additional measure of the difference in cross-frame magnitudes throughout the two structures, the peak cross-frame stress recorded in the SR-299 field test was exceeded in 36 instances of cross-frame stress during the US-13 field test. Based on the known relationship between skew and

torsional force, the higher skew of US-13 is a likely reason for the increased cross-frame stresses (due to equal loading and similar girder stress) in this bridge.

The peak lateral bending stress in SR-299 is 3.7 times larger than the peak lateral bending stress observed in US-13 (550 psi vs. 149 psi). The lateral bending stress in SR-299 also contributes more significantly to the total stress relative to the results for US-13, with SR-299 having a lateral to vertical bending stress ratio of 69% compared to the maximum value for this quantity in the US-13 results being 38%. The peak lateral bending stress of 550 psi appears to be related to the fact that the location where this occurs is equidistant between two staggered cross-frames. Furthermore, in general, under the more critical positive vertical bending moments, the average lateral bending stresses at all cross-sections and passes is higher in SR-299 (27% versus 7%). The FEA results suggest that this is due to the staggered cross-frame layout and this is a suggested topic for further evaluation in future studies.

The cross-frame data from the field testing also indicates many cross-frame members experience a significant amount of bending, which is indicated by both variation in stress along the length of the member as well as variation in stress through the member cross-sections. This issue was investigated in the US-13 results, where the variation in peak stress along the length of the member was observed as being most prominent in diagonal members experiencing tension. These members also experience a significant stress gradient through the cross-section, with the highest difference between the two gauges on a given cross-section being 4.5 ksi. This effect is also observed in the FEA results, which also shows that the presence of bi-axial bending moments of 3,000 in-lbs in each direction in some elements.

7.2.2 **FEA Validation**

FEM of both bridges were created and analyzed, the results of which were then compared to the field test to assess modeling techniques for use in future use in parametric studies and reveal a more thorough understanding of the structural responses indicated by the field results. These results show that the FEA is of acceptable accuracy in some cases but that the FEA accuracy is very sensitive to the manner in which cross-frames are modeled. The comparison of field, FEA, and theoretical expectations also revealed that the behavior of at least one of the structures may be deviating from theoretical expectations to unintended fixity of the bearings. Additional details on the correlation between the field, FEA, and theoretical (where warranted) results is discussed in the following paragraphs.

For US-13, this analysis showed that the tensile bottom flange stresses were well predicted by the model in all cases with a maximum percent difference of 13% and the two passes closest to the instrumented locations producing a maximum of 5% difference. The FEA stresses at the cross-section experiencing the highest compressive stresses in the field testing are within 20% of the field results.

Weaker correlations were achieved in the web and cross-frame data for US-13; however, it was found that refined modeling of the cross-frames and cross-frame to girder connections dramatically improved this correlation. Regarding the web field results of US-13, it was often observed that the peak stresses differed significantly from both the FEA stresses and those expected based on the theoretical location of the neutral axis (Table 5.5). This field result was revealed to be due to that when the peak stress occurred in one gauge of a pair of gauges on opposite sides of the same web cross-section, the other gauge of the pair would be experiencing an opposite force

effect (i.e., tension on one side of the web and compression on the other, Figure 5.11). It is hypothesized that this is due to a combination of lateral bending and warping torsion of these non-compact webs. This effect is not reproduced when the cross-frames are modeled using the commonly-accepted beam elements. However, this effect is reproduced when the cross-frames were modeled with shell elements. In fact, the percent difference between the field and FEA web stress results decreased by as much as 100% (Figure 5.14).

Regarding the correlation between the cross-frame field and FEA data, the general trend of the variation in stress from gauge to gauge that was observed in the field results was reproduced with reasonable accuracy, but the percent differences in magnitude varied between 1 and 300%. However, it is encouraging that the 1% error arises from two of the locations where high compression stresses exist and that the 300% error represents only a difference in magnitude of 100 psi. The percent difference between the maximum field cross-frame stress and maximum FEA cross-frame stress is 25%, with the field test generating the higher stress value, which is typical of the field test cross-frame results relative to the corresponding FEA results. When refined modeling of one of the instrumented cross-frames was explored, the improvement in cross-frame stress correlation was less significant compared to the improvement in web stress correlation, with the percent difference ranging between 25 and 58% for the instrumented locations in the refined cross-frame compared to an original percent differences within this cross-frame ranging between 25 and 68%. As a result of these efforts it was concluded that the global response of US-13 was accurately simulated, but accurately simulating localized effects requires a FEM even more refined that the detailed FEM used in this work.

FEA bottom flange stress results for SR-299 agree closely with the maximum expected based on hand calculations using conventional bridge design assumptions. Specifically, Ambrose (2011) demonstrated that the maximum theoretical stress in the bottom flange due to the test vehicle is 2.1 ksi. In comparison, the maximum FEA stress based on averaging the two stresses corresponding to bottom flange gauges at a common cross-section (i.e., the maximum vertical bending stresses) is 2.0 ksi, differing from the theoretical result by an acceptable margin of 5%. However, the corresponding maximum from the field test is 1.2 ksi. Additional data analysis based on assessment of the neutral axis locations predicted by the field data, suggests this difference may be due to unintended fixity of the expansion joints of the bridge. While field and FEA bottom flange data differed by as little as 4%, when viewing concurrent readings from pairs of gauges on the same bottom flange cross-section, there were also several situations where greater than 100% error was observed.

The worst case situations were found to be due to situations where the FEA data predicted significant amounts of lateral bending causing stresses of opposite sign (compression on one side of the cross-section and tension on the other) which did not occur in the field data. The bottom flange results were again found to be significantly improved when refined cross-frame modeling was adopted, for example, lowering a 154% error to a 7% error in one situation. In contrast to the flange results, a larger amount of lateral stress gradient was indicated by the field web results than the FEA web results. Furthermore, while the peak web stresses were reproduced within an acceptable margin (3% difference for peak tensile stress, which occurs at the same location and under the same loading scenario, and less than 100 psi difference in peak compressive stress, which also occurs at the same location and under the same loading

scenario as in the field results), there are also instances where greater than 100% error was observed.

The correlation of the field and FEA cross-frame stresses in SR-299 do not differ significantly from the trends previously discussed pertaining to US-13. Higher maximum cross-frame stress is reported in the field results, where this value is 35% higher than the FEA result. The variation in the correlation of the field and FEA cross-frame data for SR-299 is also similar to the US-13 results in the sense that there is a significant difference in the correlation from gauge to gauge, with these values ranging from 0 to 900%. From these collective comparisons of the SR-299 field and FEA data, it was concluded that the FEA was suitable for describing a general theoretical response of this structure (which will be discussed in the following section), but conclusions on exact magnitudes or localized effects would require a FEM even more refined that the detailed FEM used in this work.

Given the improved correlation between the field and FEA responses of US-13, this model was selected as the basis for a parametric study discussed in the following section. The fact that the comparison between the FEA and field peak bottom flange stresses was within 5% gives confidence that girder results generated in these parametric models will be of reasonable accuracy. The greater variation in cross-frame stresses suggests that relative differences in cross-frame stress throughout these models will provide a reasonable estimate of cross-frame behavior, but that the FEA results will likely under-estimate the magnitudes of stress that would be likely to occur in a physical representation of the structures being modeled and these facts should be kept in mind when assessing cross-frame output from these models.

7.2.3 **Parametric Study Results**

The parametric study evaluated the influences of cross-frame layout (inline versus staggered) and cross-frame configuration (X-frame versus K-frame) at both elastic and inelastic load levels. At elastic load levels, the tensile results show a clear trend that the greater transverse stiffness of the inline cross-frames contributes to greater stresses in the cross-frame members; however, all cross-frame tensile stresses due to service loads were well below the corresponding tensile capacities. The opposite trend is true when service loads cause compression, where the staggered layout, and K-frame configuration, are both observed to cause consistently higher compressive cross-frame stresses. Furthermore, these compressive stresses exceed the member capacities in three of the four models. Yet, a significant variation in the compression results was observed with the peak compressive stresses varying by 50% in the different models, with K-frames in a staggered configuration producing the greatest stress and inline X-frames producing the lowest stress. However, in assessing the governing compressive stress results relative to the buckling capacities of the cross-frame members, it was seen that the design stresses are exceed by as much as 29% under the service level loading and that this occurs in the bottom chord of the X-frame, which has a significantly reduced capacity compared to the other members, in the staggered model. The locations of maximum cross-frame stresses in all models are in cross-frames adjacent to supports.

To further investigate the effects of cross-frame configuration and layout on bridge behavior under service loads, bottom flange stresses were also analyzed. This revealed that the locations of the maximum longitudinal stresses in the bottom flange elements are typically near the supports, either the abutments or the pier, due to

significant lateral bending at these locations. In comparing the bottom flange stress results from the four parametric models, it is seen that the greatest similitude and differences relate to whether inline or staggered cross-frames are used, where the inline cross-frames lead to bottom flange tensile stresses that are 26 to 44% greater than the corresponding model with staggered cross-frames. However, the opposite trend is observed in the compression results, where the staggered cross-frames produce compressive stresses up to 10% higher than the maximum compressive stresses in the inline models.

In the nonlinear analyses, all models resisted a live load of at least 57 times the loading used in the field test, which is the load magnitude equivalent of 44 HS-20 vehicles, in addition to self-weight. At this level of loading and for the modeling assumptions used in this work (which most notably consisted of linear elastic transverse load distribution mechanisms due to the assumed concrete and cross-frame properties), a significant level of load redistribution was observed, with four of the five girders having a fully yielded bottom flange at mid-span of the loaded span. The inline cross-frame configurations also display yielding in at least one side of the bottom flanges of all five girders at the abutment of the loaded span due to a significant level of lateral bending. This phenomenon also occurs but affects a fewer number of girders in the staggered configurations. The inline configurations also produce more yielding in the bottom flange over the pier support, with two of the five bottom flange cross-sections fully yielded at this location compared to only one of the bottom flanges being fully yielded in the staggered configurations.

These observations along with the quantification of the spread of plasticity in each model led to the conclusion that cross-frame layout was more influential to

inelastic girder response than cross-frame configuration. Viewing the inelastic regions in all models it was shown that in the staggered models, the yielded area is larger as the load has more points along the girder length where load can be transferred transversely due to the discontinuities in cross-frame placement. However, there are more locations where the bottom flange cross-section has yielded on only one side of the girder cross-section, indicating greater lateral bending stresses in these models. In terms of magnitudes of bottom flange stresses, it was found that stagger increases the compressive stress by as much as 12%. However, these effects do not indicate any significant consequence on the structural performance of the girders in terms of peak magnitude of stress under service level loads or a significant difference in the load distribution characteristics of the girders due to differences in either cross-frame configuration or layout.

With regards to the cross-frame results from the inelastic analyses, it was again concluded that the results were more sensitive to cross-frame layout than configuration, with more yielding observed in the inline cross-frames. These stress results were then considered relative to the governing compression capacities of the cross-frame members. When viewed from this perspective, the compressive demand to capacity ratios of the cross-frame members are more sensitive to cross-frame configuration than layout. Furthermore, this showed that the compressive capacities of the cross-frame members was exceeded in all four models. The largest difference was detected in the diagonal member of the K-frame Inline model where the capacity is only 7% of the demand. The X-frame Staggered model was observed as experiencing both the lowest magnitude of peak compressive strain and the lowest demand to capacity ratios.

Considering that the final girder stress state of all models was relatively similar in demonstrating favorable load redistribution, this load redistribution will be most likely to be achieved in situations where the cross-frame stress is minimized. Thus, it is concluded that the X-frame staggered configuration is the one most likely to lead to the greatest reserve capacity in the system. Modifications to the member sizes used in these cross-frames likely provide the best opportunity for further increasing this reserve capacity.

7.3 **Future Work**

While this work has provided new insights into the forces experienced by cross-frames in skewed bridges and the role of cross-frames in affecting girder stresses in these bridges, future research will undoubtedly continue to contribute to the body of knowledge on these complicated effects. This section provides a discussion of lessons learned in this research that may be worthwhile considerations to include in future related work.

The field work completed in this research included sixty strain gauges on each of two bridges. The majority of the instrumentation was devoted to the cross-frames and the balance between cross-frame instrumentation and girder instrumentation was found to be well-suited to the research objectives. While this amount of instrumentation yields a great deal of valuable data, more instrumentation would have enabled a greater understanding of structural performance. In particular, there are two aspects on which more information would have been beneficial. One of these is a means to assess the level of potential bearing fixity, which could be achieved by instrumenting girder cross-sections near the abutment. This issue has been cited in

multiple works as a plausible explanation for analytical models deviating from field results, thus it is recommended that this aspect of performance attempt to be captured in any future field work where calibration to FEA results is a component of the research objectives.

The second aspect of behavior that is recommended to consider in future instrumentation plans devoted to cross-frame stresses is a greater amount instrumentation on selected cross-sections of cross-frame members. The majority of the cross-frame cross-sections that were instrumented in this work contained one gauge on each leg of the angle members to achieve two gauges per cross-section. While this allowed for relative contributions between axial and bending effects to be generally assessed, this is not sufficient for fully resolving the stress components into the vertical and lateral bending force components producing biaxial bending in the member or assess the potential contribution of torsion in the members. To fully understand these force effects, it would be ideal to place two gauges oriented longitudinally on each leg of angle members as well as additional gauges oriented along the coordinate axes of the cross-section. While the instrumentation plan employed in the current work required significant investments in monitoring hardware to accomplish, it would be feasible (although more time consuming) to increase the number of locations at which data is gathered by repeating the same loading scenario(s) with different instrumentation groupings, in the same manner as was employed in the two days of testing used in each of the field tests conducted in this work.

Possible refinements to the FEA methodologies should also be considered in future work, but issues of computational power for both data processing and output

manipulation are imperative considerations complementary to such decisions. Chapter 3 has provided a discussion of the computing resources utilized in the present work. These capabilities are fully adequate for the US-13 model, but result in less than optimum functionality for the larger SR-299 model. Thus, it is recommended that the physical size of the bridge be considered in future field work applications that will also involve complementary FEA. The primary modeling refinement is then using shell elements to represent cross-frame members as this was found to have a significant influences for the models created in the present research. These models also included greater refinement in the cross-frame to girder connection. Refined concrete properties capable of modeling the difference in behavior under compression and tension are also recommended as a potential influence to consider in future work, particularly work involving continuous span bridges where a significant portion of the concrete experiences tensile stresses.

References

Ambrose, K. (2011). "Field Measurements and Corresponding FEA of Cross-Frame Forces in Skewed Steel I-Girder Bridges", Master's Thesis, University of Delaware, Newark, DE.

American Association of State Highway and Transportation Officials. (2010). *AASHTO LRFD Bridge Design Specifications, 5th Edition.* American Association of State Highway and Transportation Officials, Washington, D.C.

American Institute of Steel Construction (2010). *Steel Construction Manual 14th Edition.* American Institute of Steel Construction Officials.

Azizinamini, A., Kathol, S., and Beacham, M. (1995). "Influence of Cross Frames on Load Resisting Capacity of Steel Girder Bridges." Eng.J.-Amer.Inst.Steel Constr., 32(3), 107-116.

Bechtel, Andrew J. (2008). "Destructive Testing and Ultimate Capacity of Skewed Simple Span Bridges." Thesis. University of Delaware.

Bishara, A. G., and Elmir, W. E. (1990). "Interaction between Cross Frames and Girders." J.Struct.Engrg.Journal of Structural Engineering, 116(5).

Bridge Diagnostics. (2006). "BDI Strain Transducer ST-350 specifications sheet." Bridge Diagnostics, Inc.

Fasl, Jeremiah, Romage, Michelle, Helwig, Todd, Herman, Reagan, and Frank, Karl. (2009). "Field Measurements on Steel Girder Bridge with Skewed Supports Utilizing Lean-On Bracing." ASCE Proceedings of 2009 Structural Congress. Vol. 341, 1-10.

Federal Highway Administration (2012). Bracing System Design. *Steel Bridge Design Handbook*. Washington D.C

Fell, B. V., and Kanvinde, A. M. (2010). "Tensile forces for seismic design of braced frame connections - Experimental results." *Journal of Constructional Steel Research,* 66(4), 496-503.

Google Maps. (2012). <www.googlemaps.com>. (April 13, 2012).

Hartman, A. S., Hassel, H. L., Adams, C. A., Bennett, C. R., Matamoros, A. B., and Rolfe, S. T. (2010). "Effects of Cross-Frame Placement and Skew on Distortion-Induced Fatigue in Steel Bridges." *Transportation Research Record: Journal of the Transportation Research Board,* 2200(-1), 62-68.

Liu, J., and Chajes, M. J. (2008). "Lateral-torsional buckling study of a continuous, skewed, steel bridge during deck placement." *Bridge Structures,* 4(1), 15-22.

Michaud, K. (2011). "Evaluating Reserve Capacity Through Destructive Testing of a Decommissioned Bridge." Thesis. University of Delaware.

Quadrato C., Battistini A., Frank K., Helwig T., and Engelhardt M. (2010). "Improved cross-frame connection details for steel bridges with skewed supports." (2200).

Ross, J. H. (2007). "Evaluating Ultimate Bridge Capacity Through Destructive Testing of Decommissioned Bridges." Thesis. University of Delaware.

Schluter IV, E. (2001). "Influence and Design of Intermediate Cross Frames in Composite Steel Bridges." Thesis. University of Delaware.

Tedesco, J. W., Stallings, J. M., and Tow, D. R. (1995). "Finite element method analysis of bridge girder-diaphragm interaction." Computers & Structures., 56(2-3), 461.

Wang, W., Battistini, A., Helwig, T., Engelhardt, M., and Frank, K. (2011). "Staggered bracing in skewed steel bridge." Structural Stability Research Council, Conference Proceedings, 70-81.

Wang L., and Helwig T.A. (2008). "Stability bracing requirements for steel bridge girders with skewed supports." *J Bridge Eng Journal of Bridge Engineering,* 13(2), 149-157.

White D., Sanchez, A., Ozgur, C., and Chong, J. (2012)."Evaluation Of Analytical Methods For Construction Engineering Of Curved And Skewed Steel Girder Bridges", *NCHRP Report 12-79*.

Delaware Center for Transportation University of Delaware Newark, Delaware 19716

AN EQUAL OPPORTUNITY/AFFIRMATIVE ACTION EMPLOYER

To the extent permitted by applicable State and Federal laws, the University of Delaware is committed to assuring equal opportunity to all persons and does not discriminate on the basis of race, creed, color, sex, age, religion, national origin, veteran or handicapped status, or gender identity and expression, or sexual orientation in its educational programs, activities, admissions, or employment practices as required by Title IX of the Educational Amendments of 1972, Section 504 of the Rehabilitation Act of 1973, Title VII of the Civil Rights Act of 1964, and other applicable statutes. The University of Delaware has designated Karen Mancini, Director of the Office of Disabilities Support Services, as its ADA/Section 504 Coordinator under Federal law. Inquiries concerning Americans with Disabilities Act compliance, Section 504 compliance, campus accessibility, and related issues should be referred to Karen Mancini (302-831-4643) in the Office of Disabilities Support Services. Inquiries concerning Title VII and Title IX compliance and related issues should be referred to the Director of the Office of Equity and Inclusion, Becki Fogerty (302-831-8063).